Alma Mater Studiorum · Università di Bologna

Dipartimento di Fisica e Astronomia
Dottorato di ricerca in Fisica
Ciclo XXVIII

Measurement of the $t\bar{t}$ Differential Cross Section at Large Top Quark Transverse Momentum in $\sqrt{s} = 8$ TeV pp Collisions using the ATLAS Detector at the LHC

Tesi Presentata da: **Lorenzo Massa**

Coordinatore Dottorato:
Prof. Gastone Castellani

Relatore:
Chiar.mo Prof. Mauro Villa

Correlatore:
Dott. Matteo Negrini

Settore Concorsuale di Afferenza: 02/A1

Settore Scientifico Disciplinare: FIS/01

Esame Finale - Anno 2016

Contents

Introduction

The top quark, discovered in 1995 by both the CDF and D0 [1] collaborations at the Tevatron collider, is the heaviest known fundamental particle. Several interesting properties are due to its large mass $m_t = 173.34 \pm 0.27 \pm 0.71$ GeV[2] and make it a privileged window for searches for new physics.

First of all, top is the only quark decaying before the hadronization process, and its study gives important information about the "bare" quarks, like its mass and spin.

Besides, the radiative corrections to the Higgs boson mass bind together the masses of top quark, W boson and Higgs boson, making possible a series of important consistency tests on the Standard Model.

Furthermore, the study of the production of $t\bar{t}$ pairs allows to make stringent tests on the perturbative QCD predictions.

Finally, the large Yukawa coupling of the top quark with the Higgs boson makes it play a special role in the electroweak symmetry breaking and in Beyond the Standard Model physics scenarios. In particular, many BSM theories involve large couplings to top quarks and $t\bar{t}$ resonances with the invariant mass in the TeV region. In this case, the produced top quarks could have a high Lorentz boost, making their decay products overlap. Hence, it is necessary to use different strategies with respect to the standard ones, which exploit the reconstruction of well separated objects from the top decay.

The subject of this thesis is the measurement of the differential production cross section of $t\bar{t}$ pairs with high transverse momentum from pp interactions

at $\sqrt{s} = 8$ TeV at Large Hadron Collider (LHC), calculated with respect to the mass, to the transverse momentum and to the pseudorapidity of the $t\bar{t}$ system.

This analysis has been tuned on a Monte Carlo simulated sample and has been applied on a real data sample, corresponding to an integrated luminosity of $\mathcal{L} \sim 20$ fb^{-1}, recorded during the 2012 with the ATLAS detector, one of the four LHC experiments.

At LHC, $t\bar{t}$ pairs are produced mainly by gluon fusion and by quark-antiquark annihilation and almost every top quark decays into a W boson and a b quark pair. Hence depending on the decay of the Ws in a lepton-neutrino or a quark-antiquark pair it is possible to identify three different final states. The decay channel which has been studied in the analysis is the lepton+jets one, where one W boson decays hadronically while the other one decays into a lepton and a neutrino

$$t\bar{t} \to W^+b + W^-\bar{b} \to (\ell^+\nu)b + (jj)\bar{b} \qquad t\bar{t} \to W^+b + W^-\bar{b} \to (jj)b + (\ell^-\nu)\bar{b}$$

since it represents the best compromise in terms of *branching ratio* and signal-to-background ratio.

The event selection has been made through a series of cuts which are designed to enhance the $t\bar{t}$ signal component selecting events with a single isolated lepton with high transverse momentum, a sizable missing transverse energy due to the presence of a neutrino and at least one jet close to the lepton. The reconstruction of the hadronically decaying top quark, in order to deal with the overlapped decay products, exploits a jet with large radius ($\Delta R = \sqrt{\Delta\eta^2 + \Delta\phi^2} \leq 1$). The internal structure of the large jet is then analysed in order to discriminate the signal from the QCD background, applying several selection criteria on mass and energy and an algorithm to reduce the pile-up contamination. On the contrary, the leptonically decaying top is reconstructed combining the selected lepton, the jet with the highest p_T and the neutrino, whose longitudinal momentum is estimated from the missing transverse energy and the lepton, using the W boson pole mass,

$M_W = 80.4$ GeV, as a constraint. The $t\bar{t}$ system is then reconstructed making the vectorial sum of the two top quarks' four-momenta.

The most relevant backgrounds which contaminate the selection are the ones related to the QCD multijet production and the W+jets processes and they are estimated with data-driven methods. The other significant background processes, like diboson, Z+jets, $t\bar{t}$ dilepton and single top processes are simulated using Monte Carlo techniques.

The results are corrected through an unfolding procedure both at at *particle level* in the fiducial region defined by the selection cuts and at *parton level* in the full phase space, and then compared with the theoretical predictions obtained with different Monte Carlo generators.

The first chapter of this thesis will show briefly the physics of the top quark, with more emphasis on the the single lepton decay channel of the $t\bar{t}$ processes and on the boosted top.

The second chapter presents a description of the general characteristics of the LHC accelerator and the ATLAS detector, through which the data taking has been performed.

The last three chapters are dedicated to the data analysis: the third chapter describes the techniques and the Monte Carlo generators used to simulate the signal and the backgrounds, the fourth chapter describes the criteria which have been used to reconstruct the objects employed in the analysis and to select the events, finally the unfolding procedures and the $t\bar{t}$ differential cross section measurements are presented in the last chapter.

The thesis ends with two appendices describing two studies I performed in parallel to the main analysis on partially related subjects. The first appendix is about the development of a RIVET routine to calculate the boosted $t\bar{t}$ differential cross section with respect to the hadronically decaying top p_T at *particle level*. The second appendix is about the performance studies which I made for an upgrade project of the ATLAS muon trigger in the Barrel-End Cap transition region using RPCs. These studies were used in the review that led to the approval of the project by the ATLAS Collaboration in 2015.

Chapter 1

The Top Quark

1.1 The Standard Model

Nowadays, the Standard Model is the most complete theory to represent the elementary particles and their fundamental interactions. It is a model which was developed in the 1960's and 70's, and which considers matter as formed by fermions (particles with spin $\frac{1}{2}$) and their antiparticles, with the same mass and spin but opposite charges. Fermions are divided into leptons and quarks, which are both organized in three families, as can be seen in Figure 1.1 As a particular quantum field theory, the Standard Model describes the forces between the fermions through the exchange of gauge particles with integer spin, called bosons, corresponding to quantised gauge fields. The basis of the model is a set of fields corresponding to the known fermions and the gauge symmetries $SU(3)_C \times SU(2)_L \times U(1)_Y$.

Quantum Chromodynamics

The strong interaction, responsible of the forces that bind quarks, is described by the gauge theory of Quantum Chromodinamics (QCD) [3]. This theory, based on the gauge group $SU(3)_C$, couples three different colour charges (red, green, blue), carried by quarks and eight massless gauge bosons called gluons (which carry both a colour and an anticolour charge). Accord-

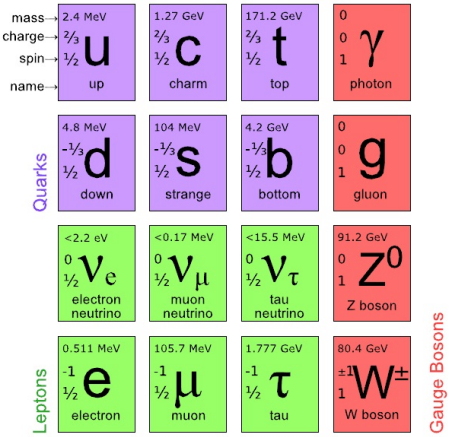

Figure 1.1: The fundamental fermions and gauge bosons of the Standard Model and their properties.

ing to the theory, quarks can form colourless bound states called hadrons, divided in mesons (a quark and an antiquark) and baryons (three quarks).

The QCD theory gives an explaination to the fact that free quarks have not been observed in nature through the effect of "confinement" of quarks in hadrons: because of the gluons' self-interaction, a coloured state like a free quark increases quickly in energy and after a short time evolves into a collimated stream of hadrons, called "jet", with a process known as "hadronization".

The strength of strong interactions is described by the coupling constant α_S, which depends on the interaction momentum transfer Q^2 and (to a first approximation in $\frac{Q^2}{\lambda^2}$) can be written as:

$$\alpha_S\left(Q^2\right) = \frac{12\pi}{(33-2f)\ln\frac{Q^2}{\lambda^2}}$$

where f is the number of different flavoured quarks with lower mass than Q^2, and λ is a phenomenological scale constant which is set around 200 MeV. From this formula, the propriety of "asymptotic freedom" is visible: for large transferred momenta compared to λ or increasingly short distances compared to $\frac{hc}{\lambda}$, the strong interaction becomes arbitrary weak, making possible perturbative calculations.

Electro-weak interactions

The electromagnetic interaction, responsible of attraction and repulsion of all electrical charged particles, is mediated by photons, while the weak interaction, responsible of the β decays and nuclear fissions, is mediated by three massive bosons W^+, W^- and Z, with mass $m_W = (80.390 \pm 0.023)$ GeV and $m_Z = (91.1876 \pm 0.0021)$ GeV [4]. The Glashow-Salam-Weinberg (GSW) gauge theory of electroweak interactions [5] provides an explanation which unifies weak and electromagnetic forces. This theory is based on the $SU(2)_L \times U(1)_Y$ gauge group of the weak left handed isospin T and hypercharge Y. The weak interaction takes the $(V - A)$ form, coupling only to left-handed particles (the direction of particle's spin is opposite to the direction of its motion) and right-handed antiparticles (particle's spin and motion have the same direction), explaining in this way its parity violation. So, the fermion fields ψ of the theory are split up into left-handed and right-handed fields $\psi_{L,R} = \frac{1}{2}(1 \mp \gamma_5)\psi$ (where γ_5 is the Dirac matrix $\begin{pmatrix} 0 & I \\ I & 0 \end{pmatrix}$), arranged in weak isospin $T = \frac{1}{2}$ doublets and $T = 0$ singlets

$$\begin{pmatrix} u \\ d \end{pmatrix}_L \begin{pmatrix} c \\ s \end{pmatrix}_L \begin{pmatrix} t \\ b \end{pmatrix}_L \quad \begin{matrix} u_R & c_R & t_R \\ d_R & s_R & b_R \end{matrix}$$

$$\begin{pmatrix} \nu_e \\ e \end{pmatrix}_L \begin{pmatrix} \nu_\mu \\ \mu \end{pmatrix}_L \begin{pmatrix} \nu_\tau \\ \tau \end{pmatrix}_L \quad \begin{matrix} e_R & \mu_R & \tau_R \end{matrix}$$

In the doublets, the weak isospin T_3 has the value $+\frac{1}{2}$ for neutrinos and up-type quarks (u, c, t) and $-\frac{1}{2}$ for the charged leptons and the down-type quarks (d, s, b). Using the electric charge and the weak isospin it is possible to define the weak hypercharge as $Y = 2Q - 2T_3$, where Q is the electrical charge in units of the fundamental electron charge $|q_e|$. So, within the doublets every lepton carries the same hypercharge $Y = 1$ and every quark has $Y = \frac{1}{3}$.

Mass terms for the gauge bosons or fermions are not permitted in a gauge group like $SU(2)_L \times U(1)_Y$ without violating the gauge invariance. The most

convincing origin of the mass of particles seems to be the introduction of a mechanism for the spontaneous symmetry breaking, known as "Higgs mechanism" [6]. According to this theory, particles' mass would be the result of the interaction with an $SU(2)$ doublet of complex scalar fields $\phi = (\phi^+, \phi^0)^T$, mediated by a spin 0 particle known as Higgs boson.

When the neutral component of the doublet obtain a non-zero vacuum expectation value, the $SU(2)_L \times U(1)_Y$ symmetry is broken to $U(1)_{QED}$, giving mass to the W and Z bosons, while the electromagnetic symmetry $U(1)_{QED}$ remains unbroken and the photons massless.

In 2012, at the LHC the production of a new neutral boson was observed, with a mass measured as $m_H = (126.0 \pm 0.4(stat.) \pm 0.4(sys.))$ GeV by ATLAS [7] and $m_H = (125.3 \pm 0.4(stat.) \pm 0.5(sys.))$ GeV by CMS [8]. This observation, with a significance of more than 5 standard deviations, is compatible with the production and decay of the Higgs boson and could be the experimental proof of its existence.

CKM Matrix and Mixing

In order to explain the suppression of the strangeness-changing decays, in 1963 Nicola Cabibbo supposed that, for the d- and s-quarks, the pure flavours eigenstates were obtained by a mixing of the two mass eigenstates. The experimental evidence is that a certain mixing angle of $\theta_C \sim 13.1°$ [9] is present in the down-type quarks and that the weak interaction is sensitive to a $(u, d\cos\theta_C + s\sin\theta_C)$ quark doublet. In 1970 Cabibbo's model was extended by Glashow, Iliopoulos and Maiani by supposing the existence of a fourth quark, the charm quark, to explain the suppression of the flavour changing neutral current processes [10].

To explain the small CP violation observed by Cronin and Fitch in some kaon decays [11] and to include it in the electroweak theory, in 1973 Kobayashi and Maskawa supposed the existence of a third generation of quark (the top and the bottom quark), at a time when the charm quark was yet to be discovered [12].

In this model, the weak eigenstates of the down type quarks d', s' and b' have to be considered as a combination of the corresponding mass eigenstates d, s and b. This mixing of eigenstates is described by the Cabibbo-Kobayashi-Maskawa (CKM) matrix:

$$\begin{pmatrix} d' \\ s' \\ b' \end{pmatrix} = \begin{pmatrix} V_{ud} & V_{us} & V_{ub} \\ V_{cd} & V_{cs} & V_{cb} \\ V_{td} & V_{ts} & V_{tb} \end{pmatrix} \begin{pmatrix} d \\ s \\ b \end{pmatrix}$$

Since the matrix is not diagonal, it is evident that there could be transitions between quark generations. By convention, only a mixing between down-type quarks is considered. The W boson couples with up type and the mixed down-type quarks of every doublet.

The CKM matrix is unitary, and its diagonal entries are very close to unity, while the others are very small. Indeed, the other terms are of the order of ~ 0.2 between the first and the second generation and ~ 0.04 between the second and the third generation and even smaller between the first and the third generation [4]. All these terms are measured experimentally, except the V_{tb} matrix element, whose direct measurements (made using the single top production cross section) aren't as precise as the indirect ones which suppose the unitarity of the CKM matrix and only three quark generations, resulting $|V_{tb}| > 0.999$ at 90% of confidence level. However, the experimental measurements are in good agreement with the theoretical constraints, although they are affected by large uncertainties.

The evidence of neutrino oscillations [13] has led to the hypothesis that there is also a lepton mixing, described by the Pontecorvo-Maki-Nakagawa-Sakuta matrix [14].

The Lagrangian of the Standard Model

The Standard Model Lagrangian, which must be gauge invariant, local and normalisable, can be divided into four terms:

$$\mathcal{L}_{SM} = \mathcal{L}_{Gauge} + \mathcal{L}_{Matter} + \mathcal{L}_{Higgs} + \mathcal{L}_{Yukawa}$$

The first term is the pure gauge Lagrangian:

$$\mathcal{L}_{Gauge} = -\frac{1}{2}\ \mathbf{Tr}\ G^{\mu\nu}G_{\mu\nu} - \frac{1}{8}\ \mathbf{Tr}\ W^{\mu\nu}W_{\mu\nu} - \frac{1}{4}B^{\mu\nu}B_{\mu\nu}$$

where $G^{\mu\nu}$, $W^{\mu\nu}$ and $B^{\mu\nu}$ are the gluon, the weak and the hypercharge field-strength tensors, respectively. These terms express the kinetic energy of the gauge fields and their self interactions.

The second term is the so called "matter" Lagrangian:

$$\mathcal{L}_{Matter} = \bar{Q}^i_L i\gamma^\mu D_\mu Q^i_L + \bar{u}^i_R i\gamma^\mu D_\mu u^i_R + \bar{d}^i_R i\gamma^\mu D_\mu d^i_R + \bar{L}^i_L i\gamma^\mu D_\mu L^i_L + \bar{e}^i_R i\gamma^\mu D_\mu e^i_R$$

where Q^i_L and L^i_L are the quark and lepton doublets, and there is an implicit sum on the index i of the generations. This term expresses the kinetic energy of the fermions and their interactions with the gauge fields, which are contained in the covariant derivatives D_μ.

The third term is the Higgs Lagrangian:

$$\mathcal{L}_{Higgs} = (D^\mu\phi)^\dagger\, D_\mu\phi + \mu^2\phi^\dagger\phi - \lambda\left(\phi^\dagger\phi\right)^2$$

This term expresses the kinetic energy of the Higgs field, its gauge interaction and the Higgs potential. Choosing the signs of μ^2 and λ it is possible to vary the shape of the potential $V(\phi) = \mu^2\phi^\dagger\phi - \lambda\left(\phi^\dagger\phi\right)^2$. With $\mu^2 < 0$ and $\lambda > 0$ the potential energy $V(\phi)$ has a shape which looks like a Mexican hat, as can be seen in Figure 1.2: in this way there will be a non-trivial vacuum expectation value of the Higgs field on the circle of minima in the field space given by $\langle\phi^0\rangle = \frac{\mu}{\sqrt{2\lambda}} = \frac{v}{\sqrt{2}}$. The value of v can be extrapolated through the indirect constraints posed by the formula of radiative corrections to the mass of the W boson, which depends on the masses of the top quark and the Higgs boson (further details are shown in Section 1.2.2), obtaining $v \approx 246$ GeV.

It is always possible to obtain with a rotation an Higgs doublet in the form $\phi = \begin{pmatrix} 0 \\ \frac{v+H}{\sqrt{2}} \end{pmatrix}$, where all the components are real and H is a scalar field with zero vacuum expectation value, corresponding to the physical Higgs boson. Using this form of ϕ, the $(D^\mu\phi)^\dagger\, D_\mu\phi$ term produces mass terms for the gauge

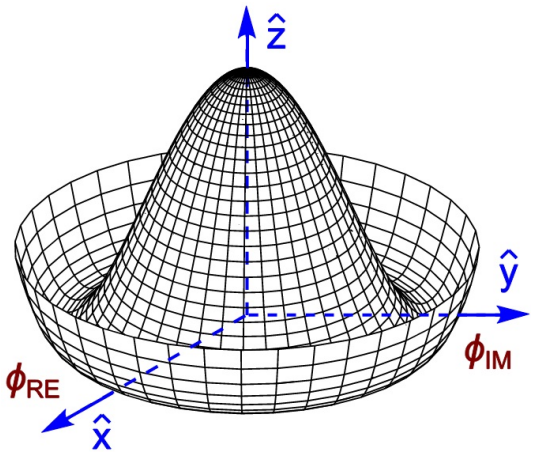

Figure 1.2: The so called "Mexican hat" shape of the Higgs field.

bosons, and for example the masses of W and Z bosons are $M_W = g\frac{v}{2}$ and $M_Z = \sqrt{g^2 + g'^2}\frac{v}{2}$.

Finally, the last term of the lagrangian describes the Yukawa interaction of the Higgs field with fermions:

$$\mathcal{L}_{Yukawa} = -\Gamma_u^{ij}\bar{Q}_L^i \epsilon \phi^* u_R^J - \Gamma_d^{ij}\bar{Q}_L^i \epsilon \phi d_R^J - \Gamma_e^{ij}\bar{L}_L^i \epsilon \phi e_R^J + h.c.$$

where Γ_u, Γ_d and Γ_e are 3×3 complex matrices.

As a result of the interaction with the Higgs field, the fermions' mass terms can be introduced as $m_f = \lambda_F \frac{v}{\sqrt{2}}$, where λ_f is the Yukawa coupling term for the fermion mass eigenstate f, which sets both the mass and the coupling of a fermion with the Higgs boson.

1.2 The Top Quark

The top quark is the last quark which has been discovered. Its first observation was made in 1995 by the CDF and D0 experiments using the Tevatron collider, at Fermilab [1], which was the only accelerator of its time which could reach the necessary energy. The most precise measurements performed by Tevatron's experiments yield a mass of $m_t = 173.34 \pm 0.27 \pm 0.71$ GeV[2].

Top mass, cross section and other proprieties, are still studied at LHC, which had already collected a much larger statistics with respect to the Tevatron collider and can be considered as a top-factory: at a luminosity of 10^{33} $\mathrm{cm}^{-2}\mathrm{s}^{-1}$ and center-of-mass energy of 7 TeV, the $t\bar{t}$ pairs produced were approximately one per second.

1.2.1 Top quark characteristics

Top quark is the most massive particle ever discovered.
Because of this property, the study of this quark is really important to make stringent tests of Standard Model and search for New Physics, for many reasons:

- The mass of the top quark is near the Electroweak Symmetry Breaking scale η, with the largest Yukawa coupling with the Higgs boson ($\lambda_T = \frac{\sqrt{2}m_T}{\eta} \approx 1$).
- The mass of the top quark, of the W boson and of the Higgs boson are strictly bounded by the formula of radiative corrections to the W mass. A better knowledge of the mass of top quark and W boson imposes indirect constraints on the Higgs boson mass.
- $t\bar{t}$ production cross section can be used to test QCD: top quark is produced at very small distances ($\frac{1}{m_T}$), so $\alpha_S(m_T) \approx 0.1$ and the perturbative expansion converges rapidly.
- The top quark decays before hadronization ($\frac{1}{m_T} < \frac{1}{\Gamma_T} < \frac{1}{\Lambda} < \frac{m_T}{\Lambda^2}$), so it can be used to study spin characteristics and make tests of the V-A interaction theory.

1.2.2 The Top Quark in the Searches for the Higgs Boson

In the electroweak theory, every quantity depends at tree level on three parameters: the two coupling constants g and g' and the vacuum expectation

value of the Higgs field v. To determine these parameters, three precision quantities can be used:

$$\alpha = \frac{1}{4\pi}\frac{g^2 g'^2}{g^2 + g'^2}, \qquad G_F = \frac{1}{\sqrt{2}v^2}, \qquad M_Z = \frac{1}{2}\frac{v}{\sqrt{g^2 + g'^2}}.$$

For example, it is possible to express the mass of the W boson at tree level as

$$M_W^2 = \frac{1}{4}g^2 v^2 = \frac{1}{2}M_Z^2\left(1 + \sqrt{1 - \frac{4\pi\alpha}{\sqrt{2}G_F M_Z^2}}\right).$$

Defining the Weinberg angle as $\sin^2\theta_W = 1 - \frac{M_W^2}{M_Z^2}$, the mass of the W boson can be expressed as [15]

$$M_W^2 = \frac{\frac{\pi\alpha}{\sqrt{2}G_F}}{\sin^2\theta_W\,(1 - \Delta r)}$$

where Δr represents the loop corrections.

The production of a virtual top contributes to the mass of the W and the Z with the first loop diagrams shown in Figure 1.3.

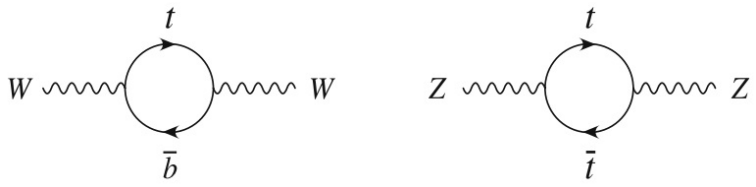

Figure 1.3: First loop contribution of virtual top quarks to the mass of W and Z bosons.

The first loop correction due to the virtual top production can be parametrised in this way:

$$(\Delta r)_{top} \simeq -\frac{3G_F}{8\sqrt{2}\pi^2\tan^2\theta_W}m_t^2.$$

Also the Higgs boson contributes to the Δr correction by the first loop diagrams shown in Figure 1.4.

Figure 1.4: First loop contribution of virtual Higgs bosons to the mass of W and Z bosons.

The term Δr due to the Higgs boson can be parametrised as

$$(\Delta r)_{Higgs} \simeq -\frac{3G_F m_W^2}{8\sqrt{2}\pi^2}\left(\ln\frac{m_H^2}{m_Z^2} - \frac{5}{6}\right).$$

The corrections to the mass of the W boson due to the top quark are larger, mainly because Δr depends quadratically on the top quark mass, while there is only a logarithmic dependence on the Higgs boson mass. Through these calculations it has been possible to constrain theoretically the value of the top quark mass, before its observation and direct measurement made at Tevatron in 1995. Once the top quark has been observed and the measurement of its mass found to be in good agreement with the bounds from the W mass radiative correction formula, it has been possible to use the same formula combined with the precision measurements of the top quark and the W mass to indirectly constraint the Higgs boson mass.

Before July 2012 the direct searches for the Higgs boson made at the LHC lead to constraints excluding at 95% of C.L. a wide area of possible values of its mass, leaving possible only the values between 115,7 and 127 GeV and between 600 and 1000 GeV. The latter interval was largely disfavoured by the constraints due to the precise electroweak measurements. Such indirect constraints obtained with the global electroweak fit using precise measurements of the W and the top quark mass give an important information on the possible values of the Higgs boson mass within the Standard Model framework. Figure 1.5 shows the $\Delta\chi^2$ of the last best fit as a function of Higgs boson's mass, showing that low mass values are largely preferred by the Standard Model. Figure 1.6 shows the 68% C.L. contour in the (m_{top}, M_W) plane, obtained from the global electroweak fit, from both direct and indirect mea-

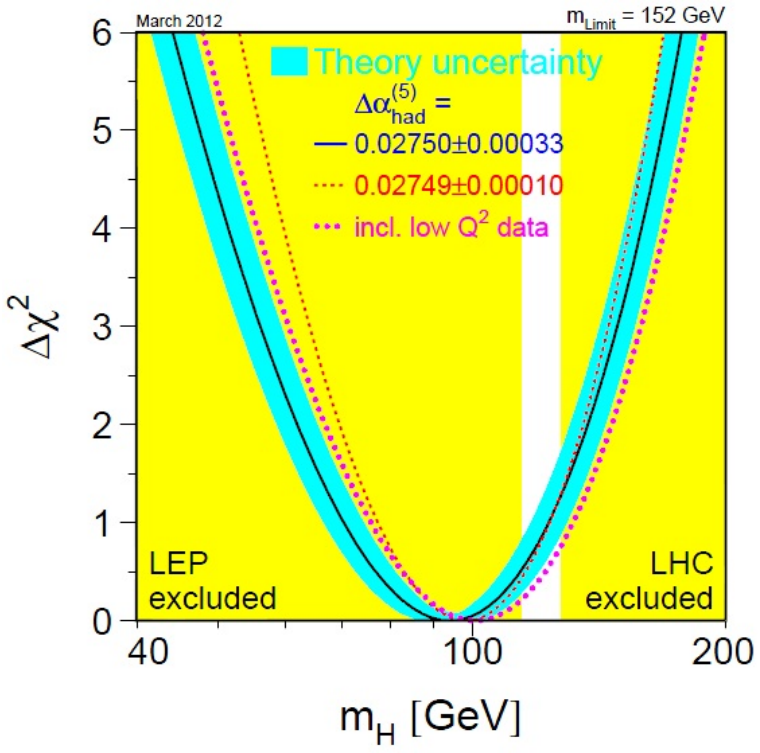

Figure 1.5: Results of the fit on precision electroweak measurements. The blue band plot shows the goodness of the fit as a function of the Higgs mass. The direct limits on the mass at 95% of C.L. are also shown in yellow. The plot is from [16]

surements. The two contours are in good agreement and give another proof of the goodness of Standard Model. In the plot there are shown also the isolines of the possible Higgs boson's mass in the Standard Model, and it could be seen that only a few values of m_{top} and M_W are still compatible with the possible range.

Together with the refinement of the indirect constraints, with the high energy and statistics available at the LHC it has been possible to perform direct searches on the Higgs boson and measurements of its mass: on July 4, 2012 both ATLAS[7] and CMS[8] confirmed the observation of a new neutral boson of mass $m_H \sim 125 - 126$ GeV, compatible with production and decay mechanisms of the Standard Model Higgs boson. This evidence has been obtained combining the results in the channels of $H \to ZZ^* \to 4\ell$,

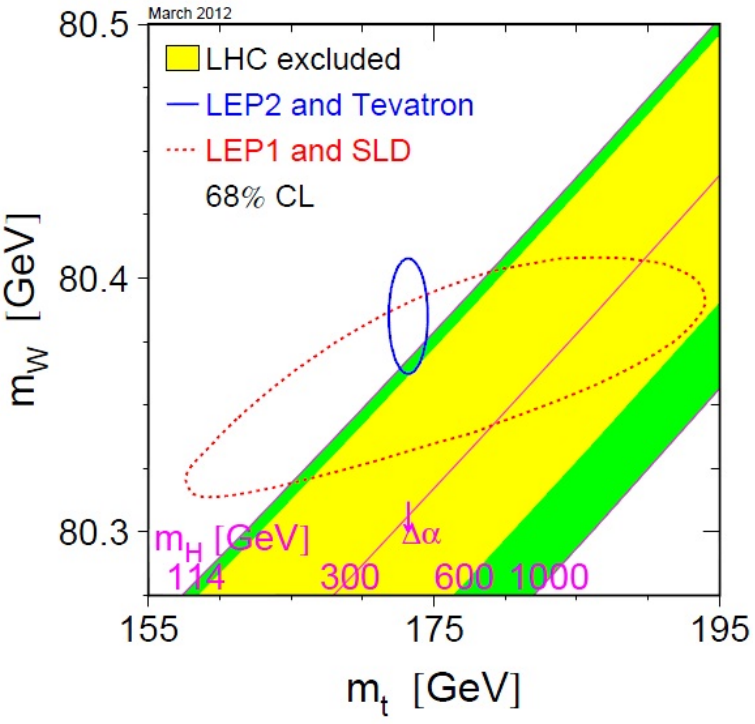

Figure 1.6: Isolines of the possible values of the Higgs boson's mass, in a M_W vs m_{top} plot. The two ellipses show the 68% C.L. constraints due to the measurements of the W and the top mass. The plot is from [16]

$H \to \gamma\gamma$, $H \to WW^* \to e\nu\mu\nu$, $H \to b\bar{b}$ and $H \to \tau^+\tau^-$, using a dataset corresponding to integrated luminosities of 4.8fb^{-1} at $\sqrt{s} = 7$ TeV in 2011 and 5.8 fb^{-1} at $\sqrt{s} = 8$ TeV in 2012. After this observation, the formula of radiative corrections to the mass of the W and its indirect constraints to the Higgs boson mass have become a new stringent test on the Standard Model, in order to verify its self-consistency: the mass of the particle observed by ATLAS and CMS is fully compatible with the limits set by the top quark and W boson masses.

1.2.3 Top quark production cross section

Differential and Total Cross Section

Given the high energy which is necessary, the most effective way to produce top quark is using hadron colliders, like the Tevatron at Fermilab (where it was seen for the first time) or the LHC at CERN.

In a scattering experiment it is useful to consider the flux of incident particles Φ as the number of particles per unit time which traverse a unit surface perpendicular to the beam direction. Far from the interaction point, in a position described by the polar angles θ and φ, a detector is placed, subtending the solid angle $d\Omega$. Hence, with this detector is possible to count the number dn of particles which are scattered per unit time into the solid angle $d\Omega$ about the direction (θ, φ).

There is a proportionality between dn, $d\Omega$ and Φ, and a coefficient of proportionality $\sigma(\theta, \varphi)$ between these quantities can be defined

$$dn = \Phi\sigma(\theta, \varphi)d\Omega$$

which have the dimensions of a surface. This coefficient is called *differential scattering cross section* in the direction (θ, φ), and is usually measured in barns and submultiples of barns, where

$$1 \text{ barn} = 10^{-24} \text{ cm}^2.$$

Hence, the number of particles per unit time which are observed by the detector is equal to the number of particles which would cross a surface $\sigma(\theta, \varphi)d\Omega$ perpendicular to the incident beam. Similarly, it is possible to define a *total scattering cross section* σ as

$$\sigma = \int \sigma(\theta, \varphi)d\Omega.$$

Production in hadron colliders

When two hadrons collide, the hard interaction can be represented by a model involving their partons, which are three valence quarks (uud in the case

of protons) and many other "sea" quarks and gluons, that carry a fraction of the momenta of the hadrons. A hadronic collision can be factorized [17] into a parton collision weighted by the Parton Distribution Function $F_i(x_i, \mu_F)$ which express the probability of the parton i to carry the fraction x_i of its parent hadron's momentum.

Hence, the cross section which is measured in an hard scattering experiment can be expressed as

$$\sigma = \sum_{i,j} \int dx_1 dx_2 F_i^{(1)}(x_1, \mu_F) F_j^{(2)}(x_2, \mu_F) \hat{\sigma}_{ij}(s; \mu_F, \mu_R)$$

where the sum runs over gluons and quarks (both the valence and the sea ones) of the colliding hadrons. In this formula, $\hat{\sigma}_{ij}$ is the perturbative cross section for collisions of partons i and j, $F_i^{(\lambda)}(x_\lambda, \mu_F)$ is the probability density to observe a parton i with longitudinal momentum fraction x_λ in incoming hadron λ, when probed at a scale μ_F, μ_R is the renormalization scale which defines the size of strong coupling constant, and μ_F is the factorization scale which is a free parameter that determines the proton structure if probed by a virtual photon or gluon with $q^2 = -\mu_F^2$. It is one of the principal sources of uncertainty on the theoretical cross section, and for top quark production is usually chosen $\mu_F = \mu_R = \mu \in \left[\frac{m_{top}}{2}, 2m_{top}\right]$.

In a high energy pp collider, $t\bar{t}$ pairs can be produced copiously via strong interactions, but it is sizeable also the production of single top quark, mainly in association with a b quark, via electroweak interactions.

Single Top production

The single top production is due to weak interaction, involving the Wtb vertex, with a rate which is dependent on the mass of the top quark itself. There are three processes contributing to the single top production, distinguished by the virtuality Q^2 of the W boson ($Q^2 = -q^2$, where q is the four-momentum of the W), which can be seen in Figure 1.7.

In W-gluon fusion, also known as t-channel, a virtual space-like W interacts with b quark of the sea of the proton. This process is the dominant

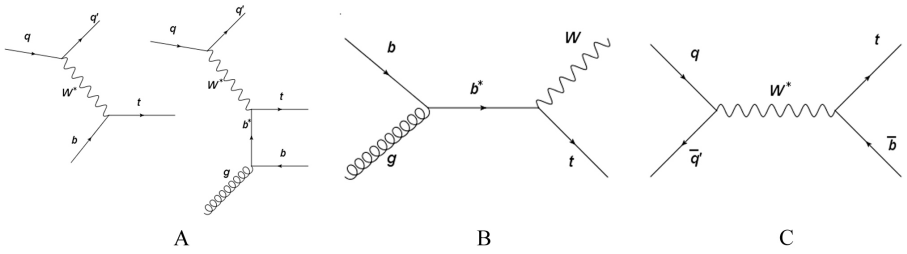

Figure 1.7: Feynman diagrams describing the production processes of single top which are possible at LHC: A: W-gluon fusion (t-channel); B: Wt production; C: $t\bar{b}$ with exchange of W^* (s-channel).

source of single top quark in colliders.

In the Wt production, the single top quark is produced in association with a real W boson after the scattering of an energetic gluon on a b quark of the sea inside the proton.

The $t\bar{b}$ production with exchange of W^*, also known as s-channel, is a Drell Yan process, where the fusion of two quarks belonging to a $SU(2)$ isospin doublet makes a time-like W boson which decay into a top quark and a b quark.

Since they are proportional at Leading Order to the square of the CKM matrix element V_{tb}, the measurement of the cross sections of these processes are the only way to measure V_{tb} without assuming the unitarity of CKM matrix and the existence of only three quark families. Despite the single top production at Tevatron has a really low cross section and high background, this process was observed for the first time in march 2009 in the CDF and D0 experiments [18], and the direct measurement of V_{tb} was found to be in good agreement with the theoretical predictions.

The single top production is now studied in different channels by ATLAS[19] and CMS[20] experiments with larger statistics, yielding more precise results. A summary of LHC measurements of the single top production cross-sections in various channels as a function of the center of mass energy compared to a theoretical calculation based on NLO QCD complemented with NNLL re-

summation [21] is shown in Figure 1.8

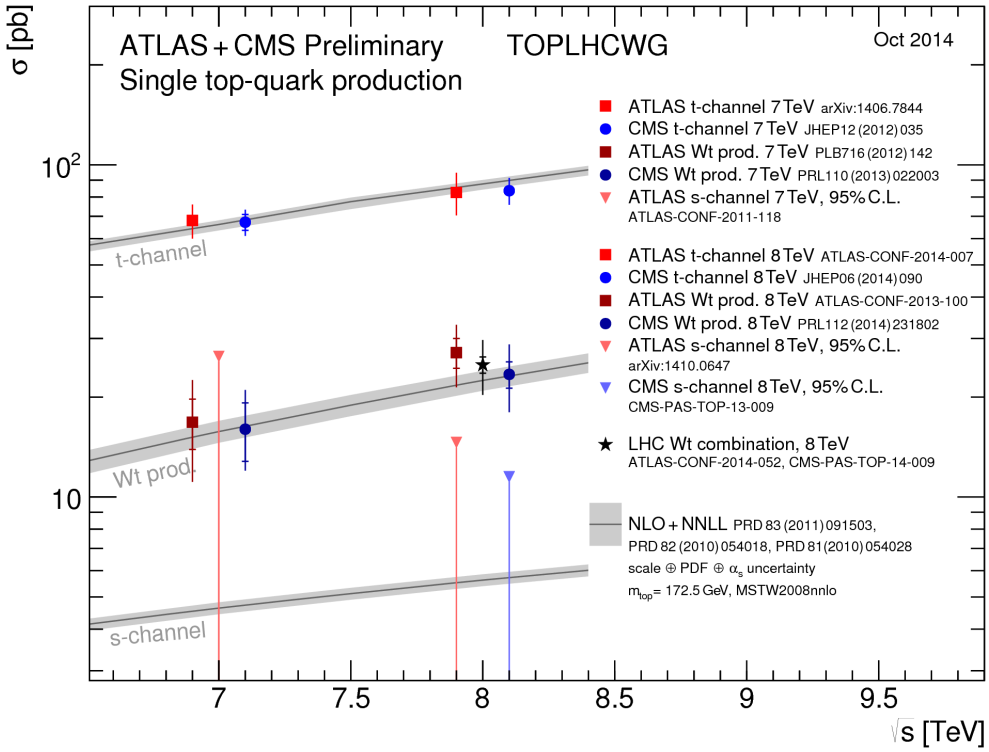

Figure 1.8: Summary of LHC measurements of the single top production cross-sections in various channels as a function of the center of mass energy compared to a theoretical calculation based on NLO QCD complemented with NNLL resummation. For the s-channel only an upper limit is shown.

Top pair production

The production of $t\bar{t}$ pairs is due to the strong interactions. At Tevatron, where protons and anti-protons collided at a center of mass energy of ~ 2 TeV, the production was dominated by $q\bar{q}$ annihilation ($q\bar{q} \to t\bar{t}$). On the contrary at LHC, in pp collisions at 8 TeV, the $t\bar{t}$ production is dominated by the gluon fusion ($gg \to t\bar{t}$), and the $q\bar{q}$ annihilation becomes relatively important only at high energies. It is estimated that in LHC the 87% of the $t\bar{t}$ pairs comes from gluon fusion, while the other 13% comes from $q\bar{q}$ annihilation [22].

At the high energies of LHC the single top production is not negligible with respect to the $t\bar{t}$ production, even if it is a weak interaction. However, $t\bar{t}$ production is two times higher than single top production.

The theoretical calculations of the $t\bar{t}$ production cross section at the Leading Order can be expressed by the term [23]

$$d\hat{\sigma} = \frac{1}{2\left(p_1 + p_2\right)} \frac{d^3p_3}{\left(2\pi\right)^3 2E_3} \frac{d^3p_4}{\left(2\pi\right)^3 2E_4} \delta\left(p_1 + p_2 - p_3 - p_4\right) \overline{\left|M\right|^2}$$

where $\overline{\left|M\right|^2}$ is the matrix element which express the transition from the initial state and the final state and p_n is the momentum of the n particle which is implied in the process.

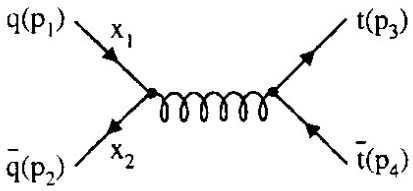

Figure 1.9: Feynman diagram of quark-antiquark annihilation with production of $t\bar{t}$.

For quark-antiquark annihilation the $\overline{\left|M\right|^2}$ term, averaged over initial and summed over final color and spin state, is:

$$\overline{\left|M\right|^2}\left(q\bar{q} \to t\bar{t}\right) = \left(4\pi\alpha_S\right)^2 \frac{8}{9} \left(2\frac{\left(p_1 \cdot p_3\right)^2 + \left(p_2 \cdot p_3\right)^2}{\left(p_1 \cdot p_3\right)^2} + \frac{m_t^2}{\left(p_1 + p_2\right)^2} \right)$$

While for gluon fusion the $\overline{\left|M\right|^2}$ term is:

$$\begin{aligned} \overline{\left|M\right|^2}\left(gg \to t\bar{t}\right) = & \left(4\pi\alpha_S\right)^2 \left(\frac{\left(p_1 + p_2\right)^4}{24\left(p_1 \cdot p_3\right)\left(p_2 \cdot p_3\right)} - \frac{8}{9} \right) \\ & \times \left(4\frac{\left(p_1 \cdot p_3\right)^2 + \left(p_2 \cdot p_3\right)^2}{\left(p_1 \cdot p_3\right)^2} + \frac{m_t^2}{\left(p_1 + p_2\right)^2} - \frac{m_t^4\left(p_1 + p_2\right)^4}{\left(p_1 \cdot p_3\right)^2\left(p_2 \cdot p_3\right)^2} \right) \end{aligned}$$

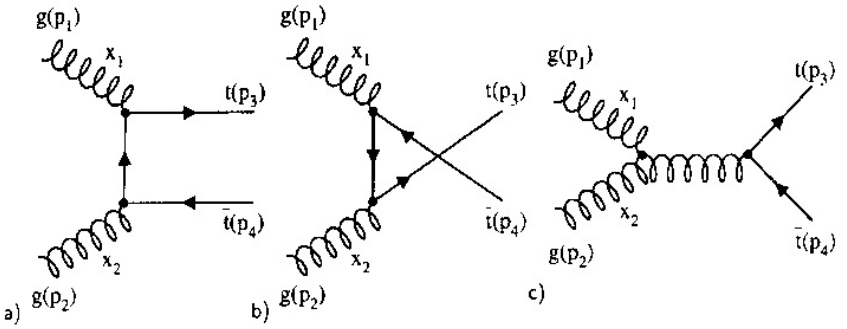

Figure 1.10: Feynman diagram of gluon fusion with production of $t\bar{t}$.

Next-to-leading order calculations [24] refine Leading Order estimations, by adding associated quark production, gluon bremsstrahlung, virtual contributions, full spin information [25], and QCD corrections [26]. The most accurate theory for $t\bar{t}$ production cross section is nowadays at approximated Next to Next to Leading Order, taking into account full resumation of soft gluon radiation [27]:

$$\sigma_{ij}\left(\beta, \frac{\mu^2}{m^2}\right) = \frac{\alpha_S^2}{m^2}\Big\{\sigma_{ij}^{(0)} + \alpha_S\left[\sigma_{ij}^{(1)} + L\sigma_{ij}^{(1,1)}\right] + \alpha_S^2\left[\sigma_{ij}^{(2)} + L\sigma_{ij}^{(2,1)} + L^2\sigma_{ij}^{(2,2)}\right] + O\left(\alpha_S^3\right)\Big\}$$

where $L = \ln\frac{\mu^2}{m^2}$ and $\beta = \sqrt{1 - 4\frac{m^2}{s}}$.

The summary of measurements made by ATLAS and CMS of the top-pair production cross-section at 8 TeV compared to the exact NNLO QCD calculation complemented with NNLL resummation [28] are shown in Figure 1.11

In Figure 1.12 it is possible to see the significative dependence of the total cross section of top quark pair production on the top quark mass and on the energy in the center of mass of the colliding hadrons. The increase in rate visible in Figure 1.12b is linked to the momentum fraction which are needed by the interacting partons to form a $t\bar{t}$ pair. At threshold energy for the $t\bar{t}$ production as at Tevatron ($\sqrt{s} \sim 2$ TeV), each of the two interacting partons must carry a large fraction of the proton momentum ($x \sim 0.2$),

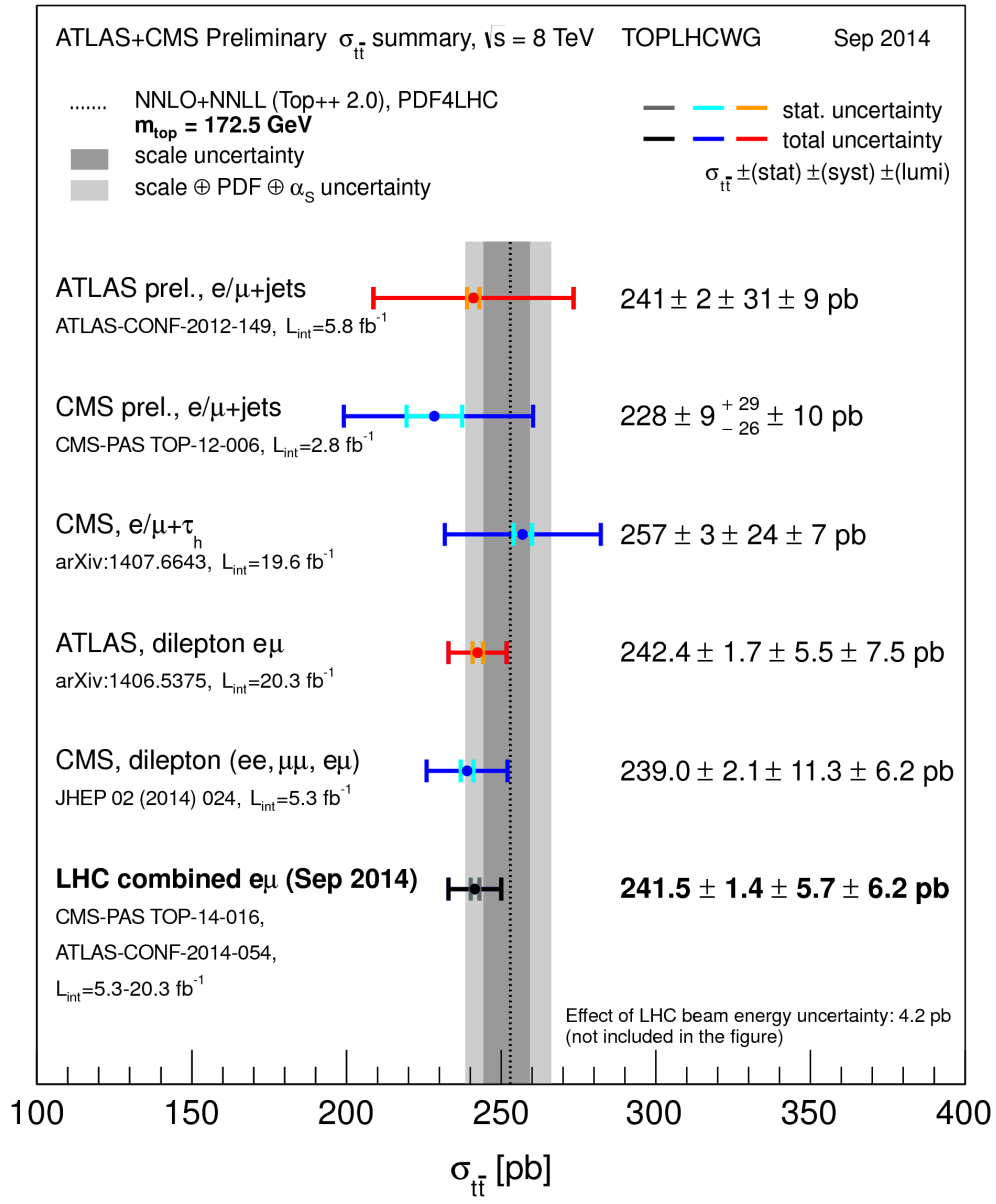

Figure 1.11: Summary of measurements of the top-pair production cross-section at 8 TeV compared to the exact NNLO QCD calculation complemented with NNLL resummation [28]. The theory band represents uncertainties due to renormalisation and factorisation scale, parton density functions and the strong coupling. The measurements and the theory calculation is quoted at m_{top}=172.5 GeV.

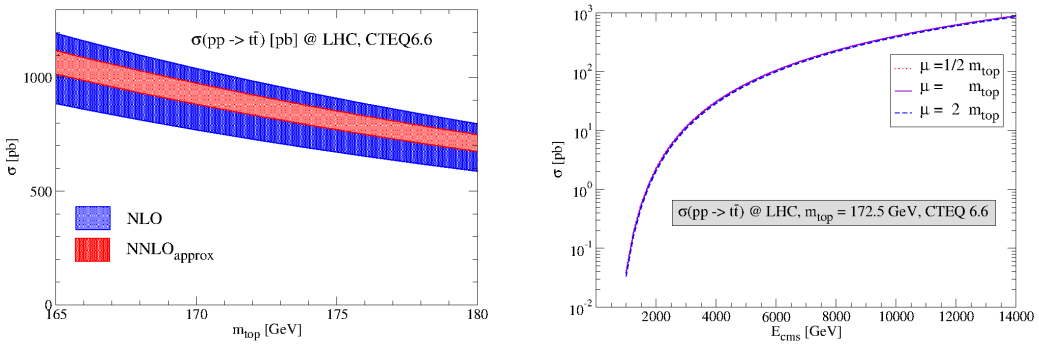

(a) Dependance on m_{top}

(b) Dependance on $\sqrt{s}$

Figure 1.12: (a) $t\bar{t}$ production cross section a a function of top mass at NLO (blue band) and NNLO (red band) at the LHC and (b) $t\bar{t}$ production at the LHC as a function of the centre of mass energy E_{cms} for $m_{top} = 172.5$ GeV and for three different scales $\mu = \frac{m_{top}}{2}, m_{top}, 2m_{top}$[29]

while at higher energies like the ones of LHC they need only a small fraction ($x \sim 0.02$) of the proton momentum.

The probability of finding a gluon with fraction x of the proton momentum grows rapidly with decreasing x, bringing to a $t\bar{t}$ production dominated by gluon fusion at LHC.

1.2.4 Top quark decay

According to the CKM matrix, the top quark decays almost esclusively producing a bottom quark and a W boson [30], with a branching ratio in the Standard Model of 99.8%.

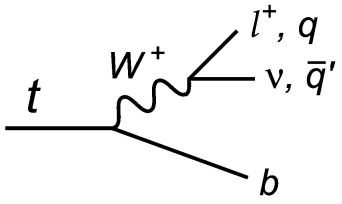

Figure 1.13: Feynman diagram of the decay of a top quark.

In one third of cases the W boson decays into a $l\nu$ pair, while in the other cases it decays into a couple of quarks. The abundance of quark pairs in which the W can decay is proportional to the correspondent CKM matrix element; in particular, the production of b quarks is suppressed, as $|V_{cb}|^2 \approx 1.7 \cdot 10^{-3}$. So, considering that the mass of the top quark is larger than the one of the W boson, the pairs produced by this decay are made only of light quarks: (u, d, c, s). Regardless the top quark which decays before the hadronization, every quark hadronize in short times, of the order of 10^{-23} seconds, generating jets.

In the case of single top events, in the final state there will be only one top quark, or a top quark and a b *jet*; after the decay of the top quark there will be from one to four jets.

In the case of $t\bar{t}$ events, there will be three different channels, depending on the number of jets and leptons in the final state:

Hadronic Channel: $t\bar{t} \rightarrow Wb + Wb \rightarrow (jj)b + (jj)b$

Both the W bosons decay into $q\bar{q}$ pairs. The characteristic signature of this channel consists in six jets, four of them are light and the other two come from the b quark hadronisation. This is the decay channel with the highest branching ratio of 46,2% [31]; however, it is very difficult to study, because of the large contamination of multiple jets due to strong interactions which do not involve top quark production, called multijet QCD.

Lepton+jets Channel: $t\bar{t} \rightarrow Wb + Wb \rightarrow (l\nu)b + (jj)b$

One of the W bosons decays into two light jets, while the other decay into $\ell\nu$. The typical signature of this channel can be divided into a leptonic and an hadronic branch. The presence of one isolated lepton in the decay products allows to reduce the background and to trigger the events easily. The branching ratio of this channel is 43,5% [31].

Di-Leptonic Channel: $t\bar{t} \rightarrow Wb + Wb \rightarrow (l\nu)b + (l\nu)b$

Both the W bosons decay leptonically. The presence of two neutrinos makes the kinematic reconstruction very difficult, while on the other hand the two high transverse energy leptons allow an efficient discrimination of the signal events with small background contamination, especially in the case of leptons of different flavours. However, the branching ratio of this channel is only 10,3% [31].

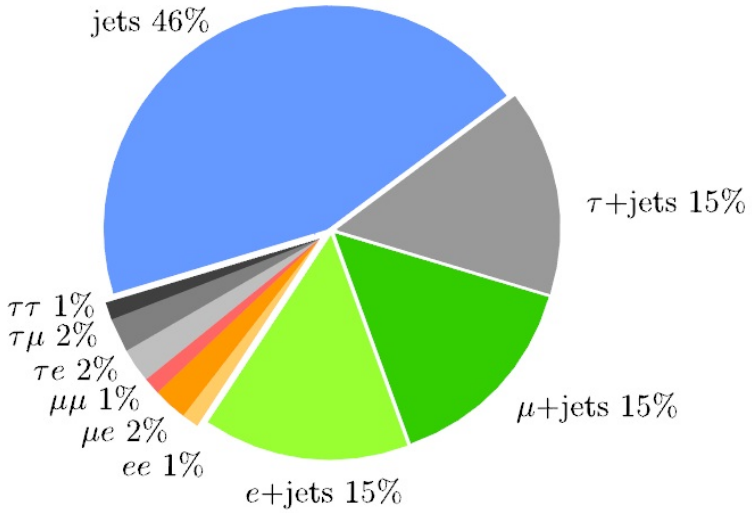

Figure 1.14: $t\bar{t}$ channels' final state fractions.

The *lepton+jets* channel (also called *golden* channel) is the preferred one in the analysis of the top quark proprieties, because it can be considered the best compromise, thanks to a sizeable branching ratio guaranteed by the presence of an hadronically decaying top, which gives also the possibility to a full kinematic reconstruction. Moreover, such events can be easily triggered due to the presence of an isolated charged lepton (electron or muon) coming from the leptonically decaying top. This is the decaying channel which has been used for the analysis described in this thesis, and it will be the only one considered in the following sections.

1.2.5 Main background sources

The sources of background always depend on the cuts which are used in the analysis to select the signal and on the physical distributions of the processes. Here the most important sources of background regarding the $t\bar{t}$ production in the semileptonic channel are listed. Their description will be detailed in Section 4.4.

$W + \ \boldsymbol{jets} \rightarrow (l\nu) + \ \boldsymbol{jets}$

This background is very important in the semi-leptonic channel and has the same features of the signal. This type of background can be reduced by the request of the presence of at least one b-tagged jet in the final state.

QCD Multijet

This type of background is present in all $t\bar{t}$ channels, and is fundamental to be well understood in order to discriminate the events of the signal in the hadronic channel. In the semileptonic channel the contamination is considerably reduced by the presence of a high energy isolated charged lepton and the missing transverse energy due to the neutrino, but the electromagnetic signal made by several processes can yield to the reconstruction of fake leptons.

The main processes which can lead to these errors are the semileptonic decay of charm quarks (where a real lepton is present, although is not isolated as in top events), the punch through of K mesons which reach the Muon Spectrometer, $\pi^0 \rightarrow \gamma\gamma$ processes and various objects which are reconstructed as isolates electrons (for example the conversion electrons). Although the probability of making reconstruction errors because of these processes is very low ($\sim 10^{-4}$), the cross section of the QCD multijet processes is so high (of the order of mb with respect to the pb of $t\bar{t}$ production) that they are an important background in the analysis. So, in order to avoid the contamination from this kind of background the lepton triggering techniques have to be very precise.

1.2.6 Boosted $t\bar{t}$ differential cross section

Top quarks in boosted regime

The centre-of-mass energies which are reached by the modern hadron colliders like LHC are far larger then the masses of known standard model particles. As an effect of these high energies, heavy particles such as W and Z bosons and top quarks can be produced with a large momentum. Top quarks which are produced with significant momentum ($p \gg m_t$) are said to be *boosted*, implying a large Lorentz boost for their decay products which will be localized in a small angular region of the detector. As the boost increases, the top's decay products start overlapping, leading to difficulties in the jets reconstruction when using standard jet and lepton reconstruction algorithms. These decay products can be efficiently reconstructed by means of jets with larger radius parameter (large-R jets).

This special kind of top quarks, even if it leads to difficulties in the reconstruction processes, is very intersting for two primary reasons. First of all, boosted tops can be a signal for Beyond Standard Model theories. Indeed, many theories that address the hierarchy problem, like Supersimmetry (SUSY) or Reciprocal System (RS), contain either top-partners, resonances with enhanced couplings to tops (like the Kaluza-Klein partners of the gluon, W,Z or graviton), or other particles which can have large branching fractions into op-rich decay modes (like the gluino). All these are probably heavier than the top quark itself, with the consequence that their signatures will include highly energetic boosted top quarks. Finally, also the properties that top quarks can be cleanly identified and that their decay products carry important polarization/spin-correlation information make the boosted tops a golden channel for new physics. Taking models with a heavy Z' [32] as example, a search for a resonance peak in $t\bar{t}$ is characterised by lower backgrounds than a generic double jet search, and can be used to study the chirality of the Z' couplings to quarks.

Boosted tops can also be used to test and validate new techniques in jet

reconstruction which have been developed in the last years making use of detailed hadronic event information in order to extend the available energy region. Top quark reconstruction using these techniques is still sensitive to pileup effects, that is effects of the underlying events, and sensitive to detector measurements effects which should be carefully tested. The Standard Model $t\bar{t}$ production is a relatively clean and well-understood phenomenon which can be used to validate these techniques.

Differential cross section

The relevance of the boosted tops in new physics theories makes the studies on differential $t\bar{t}$ production cross section extremely important. Especially the $t\bar{t}$ invariant mass distribution has a great role in these tests, because the presence of resonances decaying in top pairs can modify significantly its shape. Both fixed order QCD and SCET models [33] have theoretical predictions of how this distribution could be modified, showing theoretical errors between 10% and 15% depending on the $m_{t\bar{t}}$ value assumed.

The dependance of the $t\bar{t}$ production cross section from the p_T is important as well in the search of BSM effects. In addition to that, the momentum of the top quark is changed by its extra radiations, which are determinant in the calculation of the value of the α_s constant. So, a study on the dependence on the p_T differential $t\bar{t}$ cross section allows to test deeply the Standard Model. The theoretical prediction of the differential $t\bar{t}$ production cross section with respect to the p_T for the LHC data taking at $\sqrt{s} = 14$TeV is shown in Figure 1.15 [34].

There are many ways to determine the differential cross section: it could be extrapolated to the full phase space at the so called *parton level* (before the hadronization process), or at the *particle level*, using only the object which are visible by the detector in a fiducial phase space. If the differential cross section is calculated at *parton level*, it could be compared with the results of the theoretical calculations, while the *particle level* cross section is more similar to the experimental measurements and can be compared with

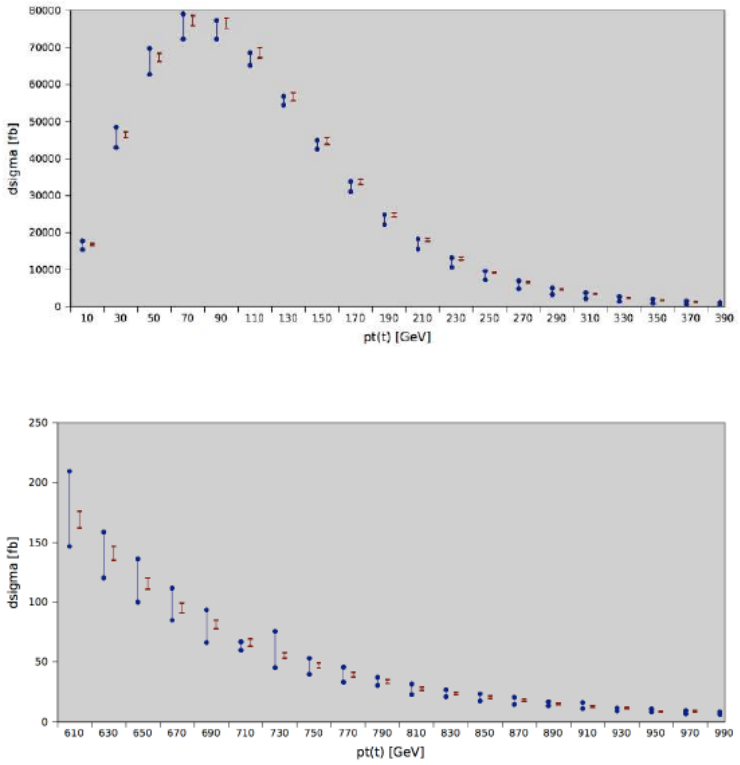

Figure 1.15: NLO QCD predictions [34] for the transverse momentum of the top quark at the 14 TeV LHC. The central MSTW pdf set and the scale variation by a factor of two around $\mu = m_T$ are represented by the blue error bars, while the dark red error bands represent one standard deviation of MSTW pdf error sets for fixed renormalization and factorization scale at $\mu = m_T$.

MC simulations.

Previous measurements

The first measurements of the $t\bar{t}$ production differential cross section have been done by Tevatron. CDF measured the differential cross section with respect to the $t\bar{t}$ invariant mass in the lepton+jets channel with 2.7 fb^{-1}, improving the sensitivity to exotic particles decaying into $t\bar{t}$ pairs [35]. On the other hand, D0 measured the differential $t\bar{t}$ production cross section with respect to the transverse momentum and absolute rapidity of the top quarks,

and with respect to he invariant mass of the $t\bar{t}$ system in 9.7 fb^{-1} of lepton+jets data [36]. All these measurements are consistent with the standard model predictions, as it is shown in Figure 1.16.

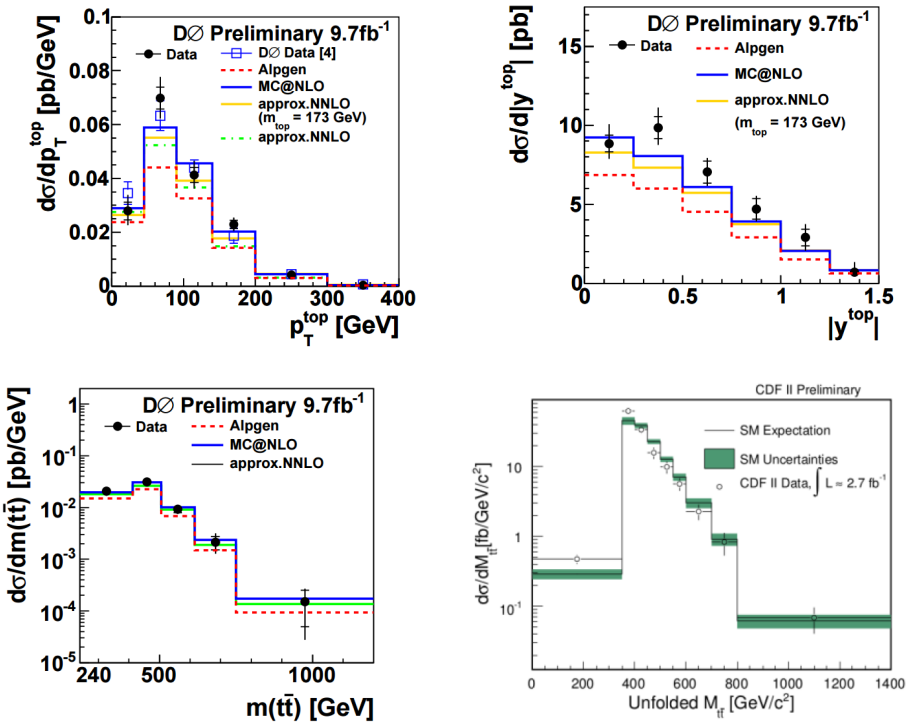

Figure 1.16: Differential cross section measured by the D0 experiment[36] as a function of top-quark p_T (top left) and $|y|$ (top right) compared with expectations from NLO, from an approximate NNLO calculation, and for several event generators. The bottom plots show the differential cross section as a function of $m_{t\bar{t}}$ obtained by the D0 collaboration[36] (bottom left) and by the CDF collaboration[35] (bottom right) compared to the standard model expectation. In all the plots the measurements are identified by points, while for the theoretical predictions a line is used.

With the large abundance of top quarks produced at the LHC it is now possible to perform new differential cross section measurements with increasing precision and several kinematic variables. ATLAS performed the measurement of the differential $t\bar{t}$ differential cross section with respect to the

top quark p_T, and of the mass, transverse momentum and rapidity of the $t\bar{t}$ system in 4.6 fb^{-1} at $\sqrt{s} = 7$ TeV in the lepton+jets channel [37]. These measurements, corrected for detector efficiency and resolution effects, are compared to several Monte Carlo simulation and theoretical calculations. From these comparisons, data seem to be softer than all predictions for higher p_T, starting from 200 GeV, especially in the case of $Alpgen + Herwig$ generator. There are also disagreements between the $m_{t\bar{t}}$ spectrum and NLO+NNLL calculations, and the same problem happens between the measured $y_{t\bar{t}}$ spectrum and the $MC@NLO + Herwig$ and $Powheg + Herwig$ generator, both evaluated with the CT10 PDF set. HERAPDF1.5 seems to be the preferred PDF set for the NLO QCD predictions.

CMS performed the measurement of the normalised differential $t\bar{t}$ cross section with respect to the usual kinematic properties of the top quarks and the $t\bar{t}$ system, as well as those of the final-state charged leptons and jets associated to b quarks, using 5.0 fb^{-1} of $\sqrt{s} = 7$ TeV data in the lepton+jets and dilepton channels. The measurements are consistent with many predictions from perturbative QCD calculations [38]. These measurements have been recently repeated using 12 fb^{-1} of data at $\sqrt{s} = 8$ TeV, improving the overall precision without particular deviation from the Standard Model [39]. In recent times, CMS also measured the normalized differential cross section in 20 fb^{-1} of lepton+jets data with respect to many event-level observables, like the jet p_T scalar sum, the missing transverse energy or the leptonic W p_T and m_T, with results which are consistent with the Standard Model [40].

The latest ATLAS and CMS measurements on normalized cross section as a function of the top quark p_T, the invariant mass $m_{t\bar{t}}$ and the p_T of the $t\bar{t}$ system are presented in Fig. 1.17.

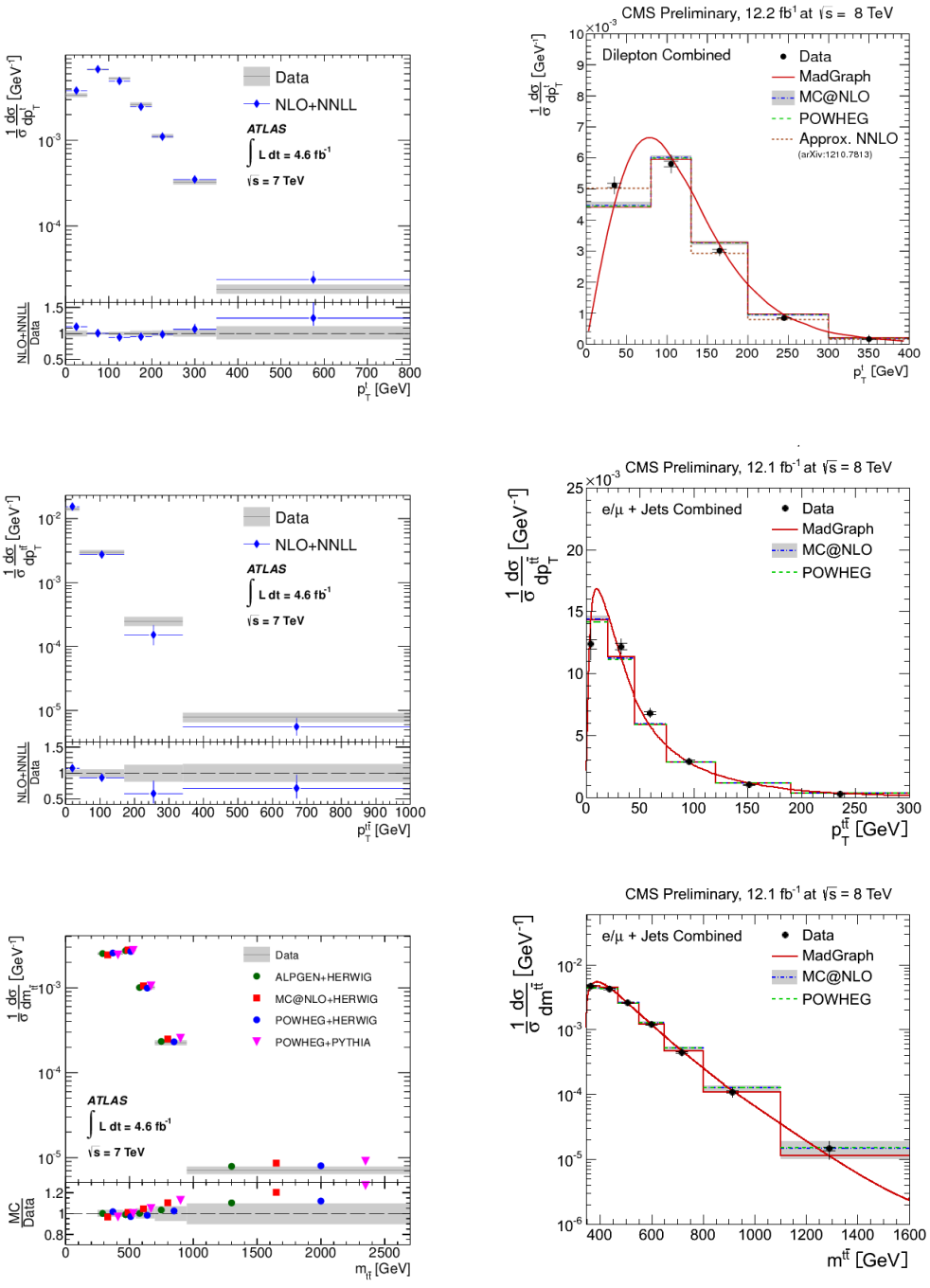

Figure 1.17: Normalised differential $t\bar{t}$ production cross section as a function of p_T^t (top), $p_{t\bar{t}}$ (middle) and $p_T^{t\bar{t}}$ (bottom), measured by ATLAS (left) [37] and CMS (right)[38]. The band (left) and outer bars (right) represent the total uncertainty.

Concerning the boosted $t\bar{t}$ production, a dedicated analysis on the absolute differential cross section in the lepton+jets channel has been recently performed by ATLAS. The results are obtained with respect to the p_T of the top quark that decays hadronically [41] (with $p_T > 300$ GeV). The results are shown in Figure 1.18 at *particle level* in the visible phase space, close to the event selection, and extrapolated at parton level to the full phase space, up to the TeV scale for top quarks with $p_T > 300$ GeV. The total uncertainties range between 15% and 20% at *particle level*, and between 20% and 40% at parton level. Incresasing the p_T, it has been found that the predictions generally overestimate the measured cross section.

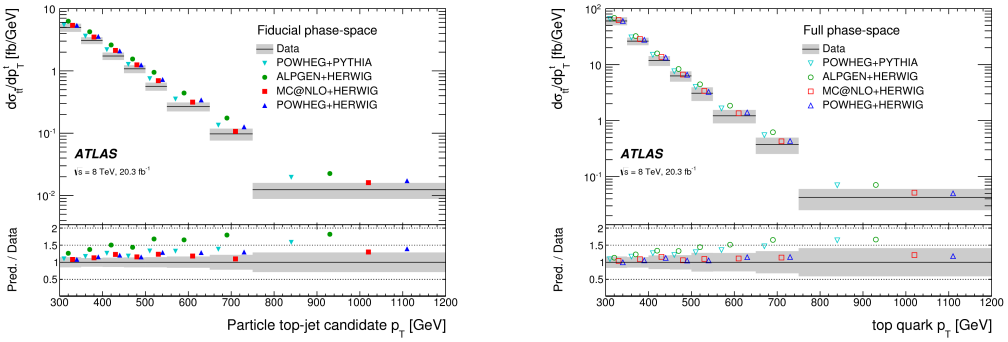

Figure 1.18: Fiducial *particle level* differential cross section as a function of the hadronic top-jet candidate p_T (left) and *parton level* result (right) as a function of the top quark p_T decaying hadronically[41]. The shaded area corresponds to the total uncertainty.

Chapter 2

The LHC collider and the ATLAS experiment

2.1 General aspects of LHC

As explained in the previous chapter, despite the Standard Model is in excellent agreement with the experimental results of many phenomena, there are still some questions to be addressed. The Higgs's Mechanism has to be studied and confirmed with higher precision. In addition, there are extensions beyond the Standard Model which have been theorized but not experimentally verified, like the Supersymmetric Extension (SUSY), where every particle has a supersymmetric partner. Finally, it is not yet understood why the universe is made of matter, even if it is supposed that in the beginning there was the same quantity of matter and antimatter,

To find an answer to these questions and many others, the LHC (Large Hadron Collider) has been built at CERN of Geneva: it is the biggest and most powerful particle accelerator in the world. It is placed inside the tunnel which originally contained the LEP (Large Electron Positron Collider), with a circumference of 27 km and an average depth of 100 m.

The efficiency of a collider can be described using its luminosity, which represents the number of interaction in a collision per unit of time and cross

section.

$$L = \frac{1}{\sigma}\frac{dN}{dt}.$$

This quantity can be interpreted in term of machine parameters only:

$$L = \frac{N_1 N_2 f n}{2\pi\sigma_x\sigma_y}$$

where

- N_1,$N_2$are the number of proton per beam
- f is the revolution frequency
- n is the number of bunches per beam
- σ_x, σ_y are the trasversal dimensions of the beam.

In 2012 LHC achieved a peak luminosity of $2.4 \cdot 10^{33} cm^{-2} s^{-1}$, becoming the world's highest-luminosity hadron accelerator, and it is designed to reach the value of $10^{34} cm^{-2} s^{-1}$ in the next years. Because of many factors, like the collisions between protons and the interaction between them and the residual gas inside the vacuum tubes, the luminosity of the experiments decreases during every run following an exponential $L = L_0 e^{-\frac{t}{\tau}}$, where τ is about 14 hours.

The LHC will be able to collide beams of protons with a center of mass energy of 14 TeV, and atoms of lead with an energy per nucleon of 2.76 TeV and a center of mass energy of 1148 TeV. Every beam is made of 3564 bunches (most of which are empty) orbiting with a revolution frequency of $f = 11.2$ kHz, corresponding to a collision every 25 ns, while now there is an interaction every 50 ns. Once the LHC will be fully operational, 2808 bunches will be filled, each bunch containing an average of $1.15 \cdot 10^{11}$ protons.

It has been decided to accelerate protons instead of electrons and positrons in order to reduce the effect of synchrotron radiation and reach higher energies. Indeed, a charged particle which makes a circular trajectory has a loss of energy equal to

$$\Delta E = \frac{4}{3}\frac{\pi q^2}{R}\left(\frac{E}{mc^2}\right)^4$$

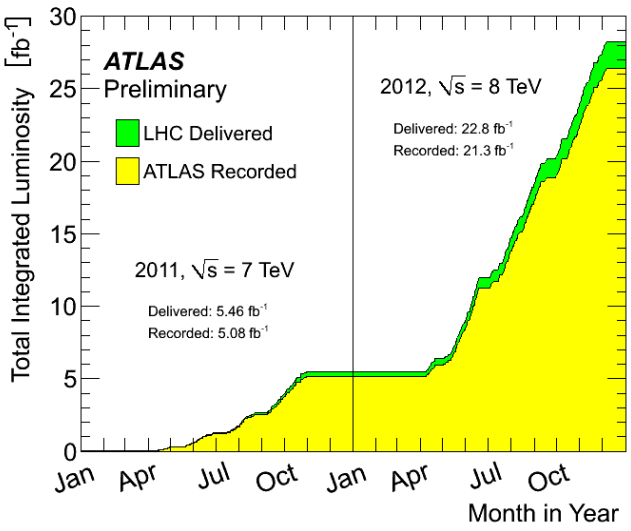

Figure 2.1: Cumulative luminosity versus time delivered to (green), and recorded by ATLAS (yellow) during stable beams and for pp collisions at 7 and 8 TeV centre-of-mass energy in 2011 and 2012.

where R is the curvature radius, q the charge of the particle, E is its energy and m is its mass at rest. It's clear that for a given energy, curvature radius and modulus of the electric charge a greater mass leads to a lower energy loss. Protons are 2000 times more massive than electrons, so they have been chosen for the experiments at LHC: in this way, the energy loss results to be lowered by a factor 10^{13} with respect to e^+e^- colliders.

However, the choice to operate with non-elementary particles leads to some problems in the interpretation of events. In fact, at sufficiently high energies, interactions occur directly between the partons, the constituents of protons, namely quarks and gluons. Collisions between protons will therefore bring processes of hard scattering between quark-quark, gluon-gluon and quark-gluon, together with low energy transfer interactions like elastic scattering, which make the interpretation of the events more complicated. In addition, every parton which is involved in the collision will have only an unknown fraction of the total energy of the protons inside the beam. With beam energy of about 7 TeV, it is estimated that the maximum value of

energy which can be investigated would be 3 TeV.

Before being injected inside the LHC and used for the planned experiments, every proton is subjected to some initial pre-accelerations. Every proton is accelerated passing through the Linac2, from where it exits with an energy of 50 MeV. Then it passes through the PSB (Proton Synchrotron Booster) and the PS (Proton Synchtotron), reaching and energy of 14 and then 26 GeV. Finally, the SPS (Super Proton Synchrotron) brings the energy of the protons to 450 GeV and inject them inside the LHC.

On the contrary, lead ions are first accelerated by the Linac3, by the LEIR (Low Energy Ion Ring), by the PS and the SPS, and then they are injected inside the LHC with different energies with respect to the protons.

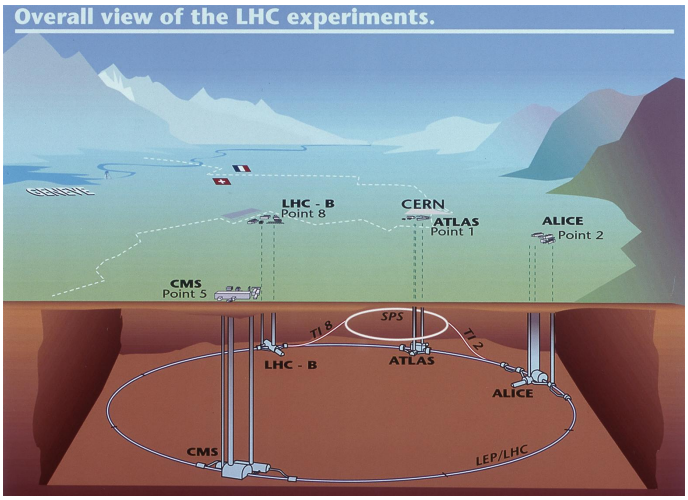

Figure 2.2: An LHC tunnel overview (not in scale)

In four points of the ring where the beams cross, detectors has been placed:

- ATLAS (A Toroidal LHC ApparatuS), which is a multi-purpose experiment, with the aim of discovering the Higgs's Boson, improve the measurements linked with the Standard Model and study physics beyond this model.

- CMS(Compact Muon Solenoid) which is an experimental similar to

ATLAS, but realized with different techniques.

- LHCb (LHC Beauty experiment) which is an experiment originally dedicated to the measurement of the CP violation in the Standard Model, paying attention in particular to the b mesons; now it is spreading also to other searches.

- ALICE (A Large Ion Collider Experiment) which is an experiment dedicated to the study of heavy ions and quark-gluon plasma.

2.2 ATLAS

ATLAS [42] is the biggest detector in LHC, with the shape of a 44 meters long cylinder with a diameter of 22 meters and a weight of 7000 tons. Because of the multipurpose nature of the experiment, it is designed to cover as much as possible the solid angle, using a large number of sub-detectors.

From the interaction point moving outwards, the particles pass through an inner tracker, an electromagnetic calorimeter, an hadronic calorimeter and then a muon spectrometer. Through the particles' interaction in these sub-detectors it is possible to have a quite detailed description about their nature, energy and direction.

The inner tracker, immersed in a solenoidal magnetic field (see Section 2.2.1) that deviates the trajectory of electrically charged particles, mesures the momentum and the charge of these particles through the radius of curvature of their trajectory.

On the contrary, calorimeters are needed to measure the energy of most of the particles. Interacting with the matter of these sub-detectors, particles lose their energy until they are completely absorbed, creating electromagnetic and hadronic showers. In this way the energy of the incident particle is converted in ionization and excitation in the detector's material.

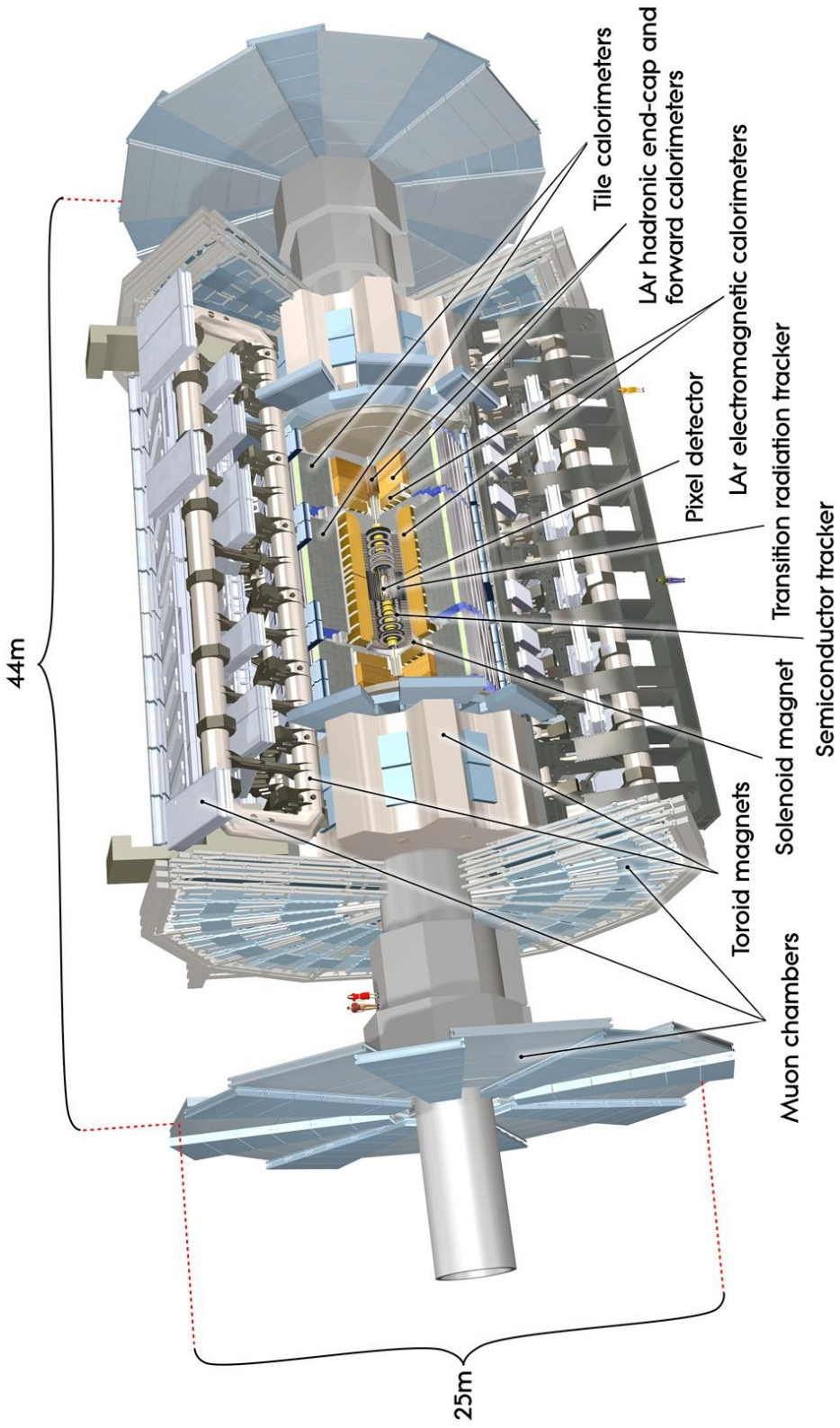

Figure 2.3: The ATLAS detector

The only particles that can traverse the calorimeters are neutrinos and muons, because of their low interaction cross section with matter. Neutrinos are neutral particles and can interact only weakly, so they escape ATLAS without being detected.

Muons are particles with similar characteristics to those of the electrons. They produce a certain ionization in the calorimeters and are able to advance beyond the calorimeter without being braked completely because their loss of energy in the process is minimal. To detect them there is the muon spectrometer, which measure the trajectory and the energy of these particles using a magnetic field, provided by a toroidal magnetic system (see Section 2.2.1).

The ATLAS coordinate system is oriented using the z axis to define the beam direction. So the xy plane is orthogonal to the beam direction, with the x axis pointing to the center of the ring, and the y axis pointing upwards. In many situation it could be useful to use a polar coordinate system: the azimuthal angle φ is the one which is measured around the beam axis, while the polar angle θ is the one measured with respect to the beam axis.

The interaction between quarks and gluons after the collision doesn't take place at rest with respect to the laboratory coordinate system. Considering the high energies and speeds involved, it is very useful to identify a variable which is invariant under Lorentz transformations, like the rapidity y:

$$y = \frac{1}{2} \ln \left(\frac{E + p_z}{E - p_z} \right)$$

Where E and p_z are the energy and the component along z of the momentum of the particle. As it is defined, rapidity y is invariant under Lorentz transformation along the z-axis. In particular, for particles with speed close to the speed of light, another variable can also be used, the pseudorapidity η:

$$\eta = -\ln \left(\tan \frac{\theta}{2} \right).$$

To express this quantity is not necessary to know energy and mass of the particle. Being invariant under Lorentz transformations along the z-axis, it

is very useful to describe events with high momenta at LHC, where energy and mass of particles aren't known and the distribution in eta of charged particles is almost constant. In the ATLAS experiment, all trajectories are usually described in terms of η, φ and z.

2.2.1 Magnetic System

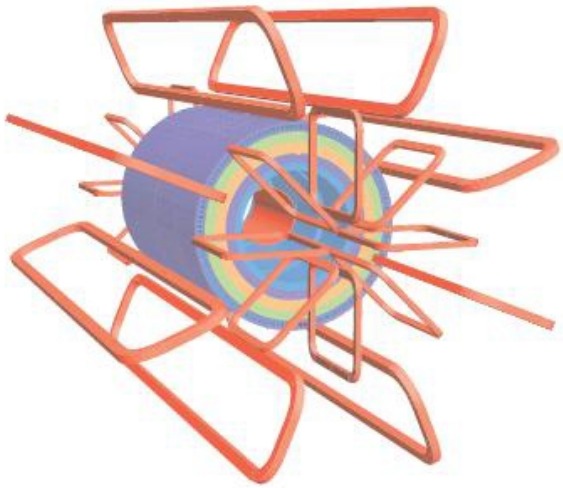

Figure 2.4: The scheme of the Barrel and the End-Cap Toroids of the magnetic system, drawn in red.

In order to deviate the path of the particles to measure their momentum, in ATLAS there are two different magnetic field systems.

The first one is the Central Solenoid (CS) [43], a superconducting solenoid with a radius of 1.2 m and a lenght of 5.3 m, which makes a magnetic field of almost 2 T. It is built around the Inner Tracker, and it is optimized to minimize the amount of material in front of the electromagnetic calorimeter.

The other magnetic system is the large superconducting air-core toroid which gives the name to the whole detector. It is made by eight Barrel Toroids (BT) [44] and two End Cap Toroids (ECT)[45], with an open structure to minimize the contribution of multiple scattering to the momentum resolution. Over the range $|\eta| \leq 1$, the charged particles are deviated by a large barrel

toroid that is 25 meters long, with an inner core of 9.4 m and an outer diameter of 20.1 m. On the contrary, in the $1.4 < |\eta| < 2.7$ region the bending is made by the end-cap magnets, placed at the ends of the barrel, which are 5 meters long, with an inner core of 1.64 m and an outer diameter of 10.7 m. In the so called transition region ($1 < |\eta| < 1.4$), there is a combination of barrel and end-cap magnetic fields. All this toroid system makes a magnetic field of almost 4 T, that is mostly orthogonal to the muon paths.

2.2.2 Inner Tracker

The first sub-detector crossed by the particles produced in the collision is the Inner Tracker [46], contained inside the Central Solenoid. It has a cylindrical symmetry, with an outer radius of 105 cm, and covers the full $|\eta| < 2.5$ region. Its principal aim is to reconstruct the trajectory of charged particles, measure their electric charge and the transverse component of their momentum, find the primary vertex of interaction and reconstruct any secondary vertexes, and distinguish electrons from other particles like photons and hadrons. Given the very large track density at the LHC, the granularity of the detector must be very fine in order to make high precision measurements. The Inner Detector is composed by in three parts: a barrel section which covers ± 80 cm with respect to the interaction point, and two identical end-caps. The arrangement of the detector layers in the barrel region is concentric with respect to the beam direction, while in the end-caps is perpendicular to the same axis.

From the technical point of view, the inner and the external part of the detector are realized with different criteria. The inner part, which is closer to the point of interaction, is realized with layers of silicon pixels, followed by microstrip detectors. The difference between pixels and microstrips consists mainly in their geometry: pixels are closely spaced pads, capable of good 2-dimensional reconstruction, while microstrips give a better resolution along one privileged coordinate. The path covered by the particle is reconstructed

through seven samples, and so it is possible to find the location of the primary vertex and any secondary vertexes. The external part of the detector is made of Transition Radiation Tracker (TRT), which samples on 36 points the path of the particle, resulting in a nearly continuous reconstruction. The precision of these points is lower than the one of the inner part of the detector, but it is possible to measure the momentum of the charged particle and there is a first discrimination between electrons and other particles, using the phenomenon which is known as transition radiation. All the main characteristics, including the resolution, of the three ATLAS Inner tracker subdetectors are summarized in Table 2.1.

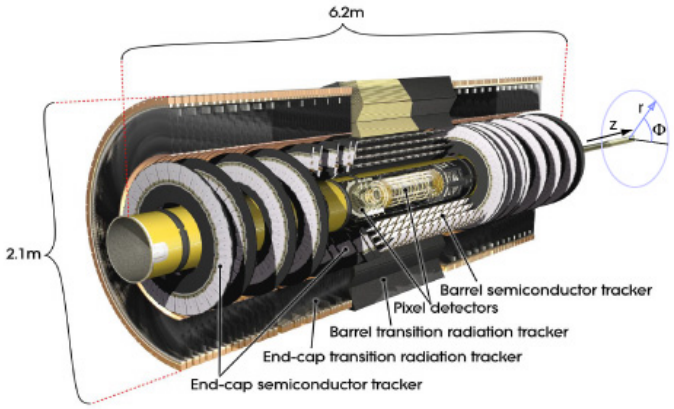

Figure 2.5: Inner Tracker scheme

Pixel Detectors

The nearest detector to the collision interaction point is the Pixel Detector [47], which allows to measure the particle impact parameters and reconstruct any secondary vertices, due to the decay of short living particles like B hadrons, with a resolution of 15 μm. Every pixel module is a 16.4×60.8 mm^2 wafer of silicon with 46080 pixels, 50×400 μm^2 each. The Inner Tracker has three layers of silicon pixels, placed at 5, 9 and 12 cm from the center of the detector, and five rings on each side with an inner radius of 11 cm and an outer radius of 30 cm, to complete the angular coverage. The pixel

modules in the layer of the barrel region are tilted 20° with respect to the cylinder's tangent, in order to counterbalance the Lorentz angle effect. The readout of this part of detector is made of almost 80.4 million channels. The ionizing radiation of more than 300 Gy and the $5 \cdot 10^{34}$ neutrons per cm^2 which are expected in 10 years of operation of ATLAS require that all chips of this detector are made using radiation-hard technologies.

Semi Conductor Tracker and Microstrip Detectors

The Semi Conductor Tracker (SCT) system [48] is designed to provide precision measurements of momentum, impact parameter and vertex position in the intermediate radial range. The SCT barrel is made of four layers of microstrip modules placed at 30, 37.3, 44.7 and 52 cm from the center of the detector. In addition, on both sides of the barrel there are 9 SCT disks that cover up to $|\eta| < 2.5$. Each module in the barrel is made of two strip layers, each of which consists of two 6.4 cm long sensors with a strip pitch of 80 μm. In the back side of the module, strips are placed rotated of 40 mrad with respect to the front side. The end-cap detector modules have the same structure except a radial disposition of the strips. The spatial resolution of the Semi Conductor Tracker is 17 μm along $R-\varphi$ direction and 580 μm in z direction, so it is possible to distinguish tracks which are separated at least by ~ 200 μm.

Transition Radiation Tracker

The Transition Radiation Tracker is the combination of drift tube chamber tracking capabilities with transition radiation detector for electron/pion discrimination. A TRT is made of a carbon fiber drift tube that cover a 4 mm diameter Kapton straw; this straw contains a 30 μm diameter gold-plated anode wire. The gap between the straw and the wire is filled with a gas mixture. Each TRT's straw has a spatial resolution of 130 μm. The passage of ionizing particle induce a low energy signal on the anodes as in drift tube chambers. At the same time, the cross of polypropylene fibers

Subdetector	Element size	Resolution [μm]	Hits/track in the barrel	Radius of the barrel layers [mm]
Pixel	50 μm × 400 μm	10 ×115	3	50.5, 88.5, 112.5
SCT	80μm	17	8	299, 371, 443, 514
TRT	4 mm	130	$\sim$ 30	from 554 to 1082

Table 2.1: Summary of the main characteristics of the three ATLAS Inner Tracker subdetectors.

made by some particles causes the emission of X-rays as transition radiation, which is absorbed by the xenon present in the gas mixture. This process is linked with an high energy signal in the readout that can be distinguished from ionization signal by the electric pulse intensity. In the barrel region, there are about 50000 144 cm long straws, displaced parallel to to the beam axis. Every wire inside the straws is divided into two halves (approximately at $\eta = 0$) and covers an $|\eta| < 0.7$ range. In the end-cap region, about 320000 37 cm long straws are arranged radially, covering $0.7 < |\eta| < 2.5$ region. The total number of TRT readout channels is approximately 351000.

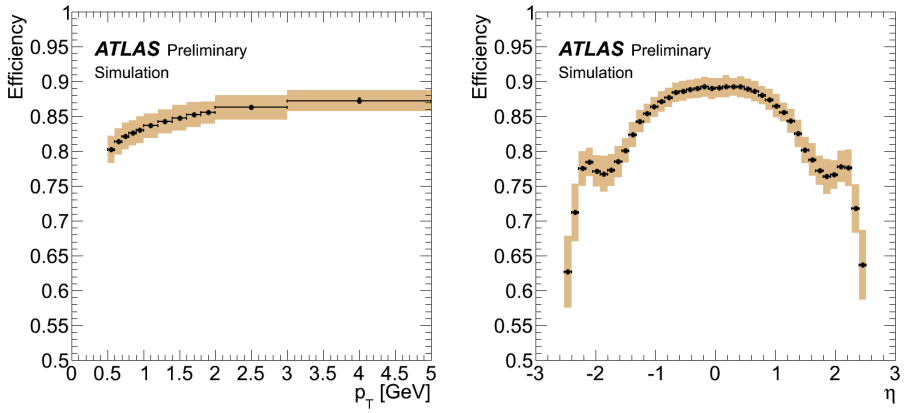

Figure 2.6: Tracking reconstruction efficiency vs transverse momentum (left) and η (right) . Special no-pileup 8 TeV Minimum Bias simulation was used. Tracking reconstruction efficiency is defined as a ratio between "number of matched tracks" and "number of generated charged particles" [49].

2.2.3 Electromagnetic Calorimeter

The aim of this detector is to measure energy and position of electrons, photons and jet. For this reason it is composed of a series of plates of lead, immersed in liquid argon, and arranged "in accordion", to reduce dead space and have a complete symmetry in φ [50]. The lead has an high cross section both for electromagnetic and strong processes, so the incident particles interact with it, making bremsstrahlung and pair creation. These processes lead to an electromagnetic shower, which ionizes the argon layer, making a signal which is detected by an electrode. From the measurement of the ionization in the argon it is possible to reconstruct the energy which was released from the incident particle.

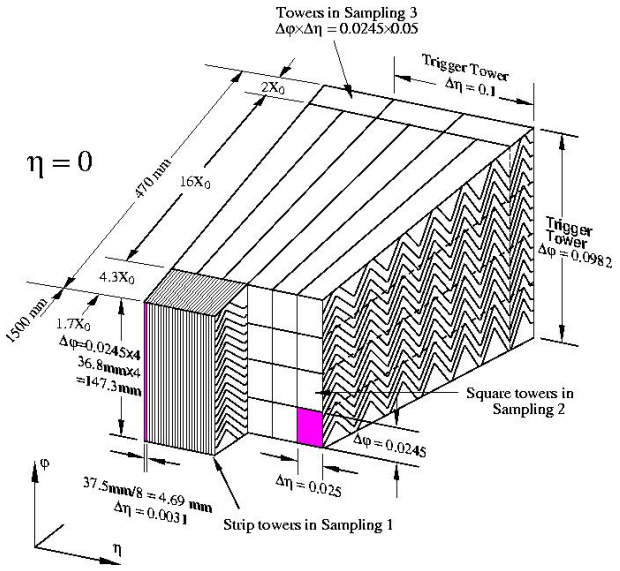

Figure 2.7: The scheme of the "accordion" structure of the electromagnetic calorimeter

The calorimeter can be divided into a central barrel, contained in a cylindrical cryostat which extends up to $|\eta| = 1.475$, and two end caps, perpendicular to the beam direction, which extend from $|\eta| = 1.375$ to $|\eta| = 3.2$. The central barrel is divided into three compartments with different characteristics. The first compartment is used to identify with extreme precision the

angle and position of the cluster of particles. To do this, it has an extremely fine granularity and is formed by very narrow cells (4 mm wide in φ). The second compartment, made by cells of dimensions $(\Delta\eta = 0.025) \cdot (\Delta\varphi = 0.025)$, must contain the central part of the cluster and measure the released energy. The last compartment, with cells of dimensions $(\Delta\eta = 0.025) \cdot (\Delta\varphi = 0.05)$, is used to measure those clusters which are not all contained in the central compartment, because of their high energy. Through this last compartment it is possible to discriminate the electromagnetic clusters from the hadronic ones, because photons and electron are often not so energetic to reach the last cells. Concerning the end caps, the lead plates are disposed radially, and the undulations of the "accordion" arrangement are perpendicular to the beam axis. A pre-sampler is used to estimate how much energy has been lost within the magnet and in the walls of the detector. A summary of these parameter can be seen in Table 2.2.

The design goal for the energy resolution of this calorimeter is

$$\frac{\Delta E}{E} = \frac{a}{\sqrt{E}} + \frac{b}{E} + c$$

where a, b and c are η-dependent parameters. The first term a is related to the sampling, and should be $\sim 10\%$ by design at low $|\eta|$. The second term b is related to the noise, and correspond to $(350 \times \cosh\eta)$ MeV for a 3×7 cluster in $\eta \times \varphi$ space in the barrel and for a mean number of interaction per bunch crossing of $\mu = 20$. At higher energies the energy resolution tends asymptotically to the third term c, which has the constant value of 0.7% by design.

During the Run 1 the relative uncertainty on the energy resolution has been measured to be better than 10% for $E_T < 50$ GeV, rising asymptotically to ∼40% at high energy[51], as can be seen in Figure 2.8.

2.2.4 Hadronic Calorimeter

In order to discriminate the hadronic jet from other particles, in ATLAS there is also an hadronic calorimeter. Its main purpose is to reconstruct

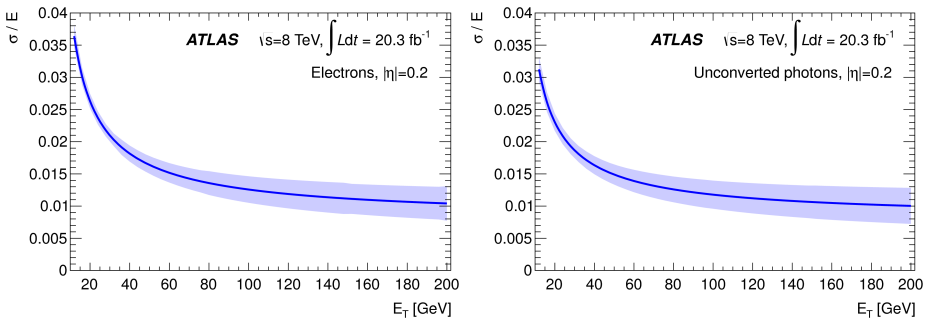

Figure 2.8: Resolution curve and its uncertainty as a function of E_T for electrons (left) and unconverted photons (right) with $|\eta| = 0.2$.[51].

the hadronic jets and measure their energy, so to contribute together with information from other sub-detectors to the calculation of the energy balance and determine the missing transverse energy. This sub-detector covers the region $|\eta| < 4.9$, and like the electromagnetic calorimeter it is divided in many parts, each one with different experimental methods to detect jets. The central part of the calorimeter (called Tile Calorimeter [52]), which extends up to $|\eta| = 1.6$, is divided into three sections, with different width and granularity. It has been designed to have a resolution

$$\frac{\Delta E}{E} = \frac{50\%}{\sqrt{E}} + 3\%$$

After the test beam, the energy resolution has been measured [53] to be

$$\left(\frac{\sigma_E}{E}\right)_{pions} = \frac{(52.9 \pm 0.9)\%\sqrt{GeV}}{\sqrt{E}} + (5.7 \pm 0.2)\%$$

in the case of pions, while there is a ratio between the electromagnetic and the hadronic signal of

$$\frac{e}{h} = 1.33 \pm 0.7.$$

The calorimeter consists of an active medium made of plates of scintillator material, placed in an absorbent body of iron. The hadrons which pass through the detector interact with iron, making an hadronic shower. The scintillator generates a light signal that is proportional to the number of

secondary particles produced, and hence to the deposited energy. This signal is taken by some photomultipliers which convert it into an electric signal. As in the electromagnetic calorimeter, also in this sub-detector there are two end caps which cover the region from $|\eta| = 1.5$ to $|\eta| = 3.2$. In this part of the detector, due to the high rate of irradiation, the active medium consists of liquid argon. The two end caps are contained in the same cryostat of the electromagnetic calorimeter, even if they are independent. After the calibration, the resolution of the end caps has found to be[54]

$$\left(\frac{\sigma_E}{E}\right)_{electrons} = \frac{(21.4 \pm 0.1)\%\sqrt{GeV}}{\sqrt{E}}$$

in the case of electrons and

$$\left(\frac{\sigma_E}{E}\right)_{pions} = \frac{(70.6 \pm 1.5)\%\sqrt{GeV}}{\sqrt{E}} + (5.8 \pm 0.2)\%$$

in the case of pions.

To increase the converge of the detector, there is an additional compartment: the Forward Calorimeter, which allows the detection of hadronic jets at angles of less than 1 degree, covering the region between $|\eta| = 3.1$ and $|\eta| = 4.9$. As for the end caps, also in this case the active medium consists of liquid argon, because of the high irradiation. According to the project, the energy resolution of the Forward Calorimeter should be

$$\frac{\Delta E}{E} = \frac{100\%}{\sqrt{E}} + 10\%$$

Nowadays, after several calibrations which have been made during the test beams, the energy resolution has been measured[55]

$$\left(\frac{\sigma_E}{E}\right)_{electrons} = \frac{(27.0 \pm 0.9)\%\sqrt{GeV}}{\sqrt{E}} + (3.6 \pm 0.1)\%$$

in the case of electrons and

$$\left(\frac{\sigma_E}{E}\right)_{pions} = \frac{(88.0 \pm 2.0)\%\sqrt{GeV}}{\sqrt{E}} + (6.8 \pm 0.4)\%$$

in the case of hadrons.

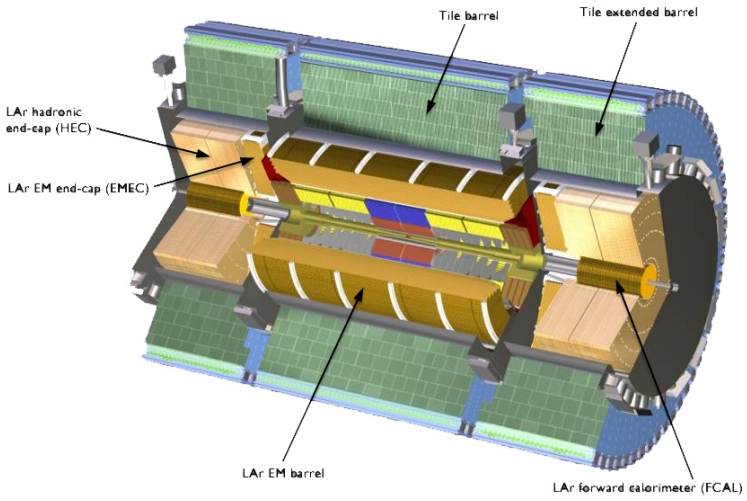

Figure 2.9: Section of ATLAS showing the electromagnetic and hadronic calorimeters

A summary of the parameters of the hadronic calorimeters can be seen in Table 2.2.

There are many ways to reconstruct the jets. The simplest one is the "cone" algorithm: the energy of the hadronic jet is calculated by adding the energy that is released and measured from all the cells contained in the cone of radius $\Delta R = \sqrt{\Delta\eta^2 + \Delta\varphi^2}$. The geometry of the calorimeter is then optimized in order to obtain the best performance: the energy resolution is the better the higher is R; a too wide cone, however, would lead to a signal degraded by electronic noise and to a greater difficulty in discriminating events. In addition to the "cone" algorithm there are other methods to reconstruct jets with more precision which will be discussed in Section 4.1.1.

Parameter	Barrel	End Cap
Electromagnetic Calorimeter		
$\|\eta\|$ coverage	1.4	1.4-3.2
Depth samples		
presampler	1	-
calorimeter	3	3
Granularity $\Delta\eta \times \Delta\varphi$		
presampler	0.025×0.1 $(\|\eta\| < 0.8)$	-
	0.003×0.1 $(\|\eta\| > 0.8)$	-
calorimeter	0.003×0.100	0.003×0.100 $(\|\eta\| < 2.4)$
	0.025×0.025	0.025×0.025 $(\|\eta\| < 2.4)$
	0.025×0.050	0.025×0.050 $(\|\eta\| < 2.4)$
		0.050×0.050 $(\|\eta\| > 2.4)$
Readout channels		
presampler	32000	-
calorimeter	10000	82000 (both sides)
Tile Calorimeter		
$\|\eta\|$ coverage	1.0	1.0-1.6
Depth samples	3	3
Granularity $\Delta\eta \times \Delta\varphi$	0.1×0.1	0.1×0.1
	0.2×0.1 (last sample)	0.2×0.1 (last sample)
Readout channels	6000	4000 (both sides)
Hadronic End Cap Calorimeter		
$\|\eta\|$ coverage	-	1.5-3.2
Depth samples	-	4
Granularity $\Delta\eta \times \Delta\varphi$	-	0.1×0.1 $(\|\eta\| < 2.4)$
	-	0.2×0.2 $(\|\eta\| > 2.4)$
Readout channels	-	8600 (both sides)
Forward Calorimeter		
$\|\eta\|$ coverage	-	3.1-4.9
Depth samples	-	3
Granularity $\Delta\eta \times \Delta\varphi$	-	$\sim 0.15 \times 0.15$
Readout channels	-	1500 (both sides)

Table 2.2: Summary of the main characteristics of the ATLAS calorimeters

2.2.5 Muon Spectrometer

Muons and neutrinos can traverse the hadronic calorimeters, reaching the external layers of ATLAS. Even if muons are charged particles which ionize the materials crossed, the energy that they lose electromagnetically interacting with other nuclei is not such as high to restrain them until the absorption. To identify them and measure their momentum there is a particular detector called Muon Spectrometer. A series of magnets arranged outside the calorimeter originates a toroidal field with lines of force that are concentric and perpendicular to the beam, deviating the charged particles and allowing the measurement of their momentum. In particular, the toroidal magnetic field is divided in three regions: into the barrel region ($|\eta| \leq 1.0$) there is a field peak of 3,9 T, in the end-cap region ($1.4 \leq |\eta| \leq 2.7$) there is a field peak of 4.1T, and in the transition region there is a magnetic field which is equivalent to the sum of the other two.

For muons with $p_T > 30$ GeV the measurement of the momentum is more precise than the one obtained with the inner tracker. On the contrary, for lower impulses the measurement is less accurate, because of the fluctuations due to the energy loss in the previous layers of the detector, of the order of a few MeV/mm [56].

To reconstruct the path of the muons, the ATLAS Muon Spectrometer uses a combination of trigger chambers, the Resistive Plate Chambers (RPC) and the Thin Gap Chambers (TGC) and high precision tracking chambers, the Monitor Drift Tubes (MDT) and the Cathode Strip Chambers (CSC). The trigger chambers are faster detectors and make rough measurements of muon momentum, while precision chambers have a better resolution but with a longer signal build-up. For muon with $|\eta| < 2$ it is used the central body of the detector, where there are MDT and RPC chambers arranged in three concentric layers with a radius of 5, 7.5 and 10 m from the beam axis. In the end-caps and transition region, the Muon Spectrometer is equipped with three wheels of MDT and TGC. For high values of η, where high counting rates are expected, CSC are mounted between the calorimeter and the mag-

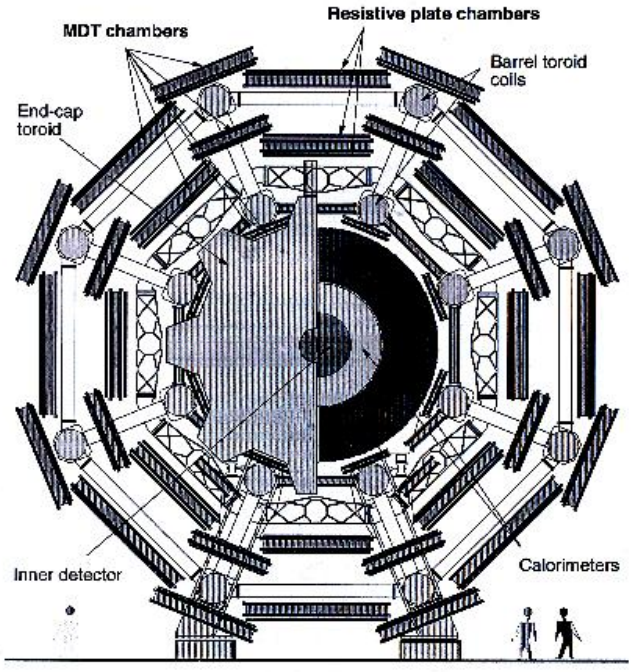

Figure 2.10: Section of the Muon Spectrometer

net. In this way, particles cross three stations of chambers starting from the interaction point.

In 2018, when LHC is scheduled to have a center-of-mass energy of $\sqrt{s} = 13 \sim 14$ TeV, an instantaneous luminosity up to $L = 3 \cdot 10^{34}$ cm^{-2} s^{-1} and 25 ns of bunch crossing interval, an extremely high rate in end-caps and transition region is expected. The upgrade which is foreseen for the transition region of the Muon Spectrometer in order to face the high rate is shown in detail in Appendix 2.

It is worth remembering that this sub-detector measure momentum and path of all charged particle which passes through it, and not only muons. For this reason, it is possible that other different particles such as pions that are able to overcome the calorimeter are recorded as muons.

Trigger chambers

In order to make fast and coarse measurements on muon p_T for the ATLAS trigger system, which has to work at 40 MHz, the Atlas Muon Spectrometer is equipped with a series of trigger chambers, in particular Resistive Plate Chambers (RPC) and Thin Gap Chambers (TGC).

RPC are gaseous parallel electrode-plate detectors, with a spatial resolution of 1 cm and an excellent time resolution of 1 ns. Each of the two rectangular layers which form the RPC are read by two orthogonal series of pick-up strips: the particle deviation in the η coordinate is measured by strips which are parallel to the MDT wires, while orthogonal strips measure the φ coordinate, needed for the offline pattern recognition.

The average strip pitch is 3 cm and inside a chamber there could be a variable number of strips: 32, 24 or 16 in η and from 64 to 160 in φ. RPC work in avalanche regime: after the passage of a particle inside the chamber, the primary ionization electrons are multiplied into avalanches by an high electric field of typically 4.9 kV/mm. The signal is read out on both sides of the chamber through a capacitive coupling of strips .

The end-cap region of the Muon spectrometer is equipped with very thin multi-wire chambers, the TGC: the name "Thin Gap" comes from the cathode-anode spacing, which is smaller than the anode-anode spacing and leads to a very short drift time, less then 20 ns. In order to have a time resolution of 4 ns and a good performance in an high particle flux, the TGC work in a saturation operation mode, being filled with a highly quenching gas mixture of 55% of CO_2 and 45% of n-pentane (C_5H_{12}). The spatial resolution of these detectors is $\sim$ 4 mm in radial direction and $\sim$ 5 mm in φ one. In addition to the trigger system, the TGC are also used to improve measurements of MDT along the φ coordinate.

Precision chambers

Some precision chambers are used to reconstruct the path of the muon.The most used precision chambers are the MDT (Monitored Drift Tubes): drift

chambers composed by two multi-layer drift tubes with aluminum walls filled with a gaseous mixture of argon and carbon dioxide, on the axis of which there is a cable with a high potential difference with respect to the walls. Each multi-layer is made of three or four layers of tubes. The electrical field created permits to collect the ions which are formed after the passage of a muon through the gas.

The end caps, which cover the area where $2.0 < |\eta| < 2.7$, are equipped with CSC (Cathode Strip Chamber). The principle used to determine the path of muons with CSC is the same of the MDT, but the background events at small angles are different, so another technical implementation is needed. The CSC are metallic chambers containing a system of parallel anode wires, which are perpendicular to 1 mm strips of opposite polarity. The crossing point of incoming muons can be measured with a resolution of 40 μm in the φ direction, while in the η direction there is a coarser resolution of 5 mm.

2.2.6 LUCID

ATLAS has several ways to measure indirectly the luminosity, but there is also one detector which is specifically designed to measure it: the LUCID (Luminosity Cherenkov Integrating Detector). It is a Cherenkov detector composed by two identical parts placed near the beam pipe at 17 m from the interaction point covering a pseudo-rapidity range $5.6 < |\eta| < 6.0$. Each part is composed by 16 aluminium pipes which were originally filled with the C4F10 gas, used to originate Cherenkov photons afer the passage of a charged particle. Since it has been found that the gas doesn't give a linear response, it has been removed from the pipes, and the Cherenkov photons are now emitted only by the quartz windows of the photomultipliers (PMT) which are located at the end the detector, resulting a total of about 40 photoelectrons per incident charged particle[57]. If a tube receives a charge over a preset threshold equivalent on average to 15 photoelectrons, it is considered hit. From the number of hits it is then possible to evaluate the average number of interactions per bunch crossing and then a relative luminosity measurement

for each bunch crossing. The whole detector has been redesigned for Run II, in order to give better performances without the gas.

2.2.7 Trigger

Once fully operational, with a luminosity of 10^{34} cm^{-2}s^{-1} and the high frequency of collisions, the LHC will have an output of about one billion events per second, an impressive number of data, impossible to manage without applying some filters. So there is a trigger system able to recognize events of interest for the study of the physics of ATLAS, minimizing dead times [58]. The selection of the events is made using three levels of trigger, called Level1 (L1), Level2 (L2) and Event Filter (EF). In all three levels selection algorithms are used, with the greatest simplicity as the main feature. In particular, L1 algorithms must work with a frequency of 40 MHz. The presence of the three levels ensures that the frequency of events to be recorded is reduced to 200 Hz, a quantity that the system of data acquisition can manage.

The first level L1 uses the information from calorimeter and muon spectrometer to select the events which are considered interesting, for example the events in which it was recorded the presence of muons, electromagnetic showers, jets, missing transverse energy or high total energy values . In particular, events with low values of total energy are not taken into account. After the L1 trigger, the data acquisition rate is decreased to ~ 75 kHz.

All the events which pass the L1 selection are examined by the Level2, which is a software-based trigger, realized with a series of selection algorithms running on farm of PCs. Like the L1, it is an online trigger, so the selection must be fast, but the slower event rate allows a CPU process time of almost 10 ms. During this time, L2 algorithms are able to make a finer selection, using other ATLAS sub-detector information collected into the Regions-of-Interest (RoI) identified at L1. Each event which is accepted by L1 make a seed that consists of a p_T threshold and an $\eta - \varphi$ position. The L2 algorithms construct a RoI around this seed position. After the L2 triggers the event

rate is reduced to ~ 2 kHz.

The last step in the trigger system, which makes the data acquisition rate decrease to 200 Hz, is the Event Filter. It is a full software-based trigger, with an elaboration time of ~ 1 s. It refines the selection using offline algorithms for more precise measurements and fake rejections. The data that have passed all this complex selection are eventually recorded.

Chapter 3

Data and Monte Carlo Simulation

For a measurement of the boosted $t\bar{t}$ differential cross section, it is important to define some criteria to select the chosen signal maximizing the background rejection. Moreover, it is important to determine the efficiencies of the selection cuts on the signal and the background processes, so a detailed simulation of the physical process and the detector simulation is needed. This chapter contains a description of all the simulated physical processes used in the analysis.

3.1 Collider Real Data Samples

In order to evaluate the signal efficiency and perform the background subtraction, the boosted $t\bar{t}$ differential cross section has been measured using samples of real data with the support of a Monte Carlo simulation.

The real data used in the analysis were collected by the ATLAS detector during the 2012 LHC pp run at $\sqrt{s} = 8$ TeV, corresponding to an integrated luminosity of $\mathcal{L} = (20.3 \pm 0.6)$ fb^{-1}, as can be seen in Figure 3.1 (left). The luminosity scale has been calibrated through the beam-overlap scans performed in November 2012, with similar techniques to those used for the $\sqrt{s} = 7$ TeV calibration [59]. In 2012, the average number of interactions per bunch crossing (μ) was around 21, as can be seen in Figure 3.1 (right). The

sample is collected considering only data which are acquired under stable conditions and fully operational sub-detectors, and applying a logical OR of a single electron trigger and a single muon trigger. The single electron trigger has a threshold of $p_T \geq 24$ GeV for isolated electrons and $p_T \geq 60$ GeV for the not isolated ones, while the single muon trigger has a threshold of $p_T \geq 24$ GeV for isolated muons and $p_T \geq 36$ GeV for not isolated ones.

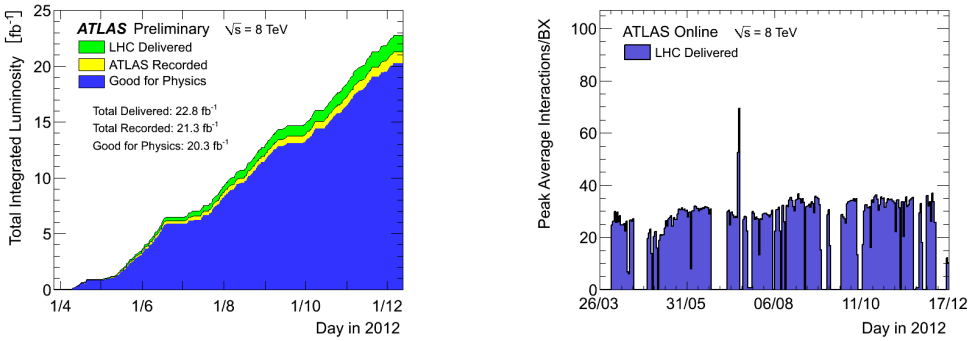

Figure 3.1: Left: Cumulative luminosity versus time delivered to (green), recorded by ATLAS (yellow), and certified to be good quality data (blue) during stable beams and for pp collisions at $\sqrt{s} = 8$ TeV in 2012. Right: The maximum number of events per beam crossing versus day.

3.2 Monte Carlo Simulation

3.2.1 Generation of Simulated Events

Monte Carlo generators[60] can be used to perform simulations to study the response of the detector for a large number of physical processes. Each simulation is usually composed of three steps: the first step is the generation of the full events from the hard parton interaction to the stable final particles which go through the detector; follows the simulation of the response of the detector, including the physical processes due to the interactions between the particles and the detector materials; finally the electronic signals analogue

to the ones obtained with the real detector are simulated through a digitalization process. In this way the output of the generator can be of the same format as real measurements, allowing the usage of the same trigger selection and reconstruction algorithms for real and simulated data. Each simulation carries the information of the "truth", corresponding to the complete description of the generated event, and of the "hits", corresponding to the deposited energies, the positions and the times measured by the detector.

The generation of the events consists in the production of a series of particles through a simulation process. The first step of the simulation produces a list of stable particles (like electrons, muons, pions and photons) and many unstable colored particles (like quarks and gluons). Usually, the output of the programs which are designed for this purpose is in the HepMC format [61], which contain all the information of the generated events. In the HepMC format the information are saved in a tree system, which allows reconstructing the entire chronology of the events, going back to the whole chain of unstable particles.

The usual steps in which the generation of simulated physical events can be divided are the following[62]:

- Hard Process;
- Parton Shower;
- Hadronization;
- Decay;
- Multiple Interaction and Beam Remnants.

Hard Process

The *Hard Process* is the most theoretically understood part of the interaction. Usually, the simulation of this part is done using fixed-order perturbative *matrix elements*, which describe the transitions between the initial and final state in Feynman diagrams. The squared matrix elements

are positive definite, so the Leading-Order calculations can be automated. On the contrary, the automatization is more difficult to be performed with Next-to-Leading-Order calculations, because the considered real and virtual contributions have equal and opposite divergences, and generators need to know ahead the way to move to the hadronization level.

Parton Shower

The *Parton Showers* step produces the full cascade of QCD partonic emissions from the primary partons (Figure 3.2).

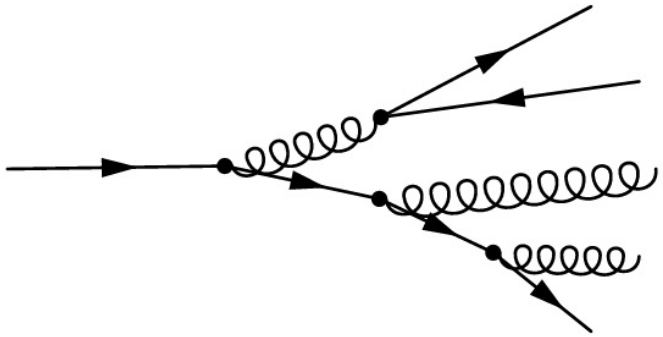

Figure 3.2: Example of Parton Shower

For example, it is possible to write a 3-jets cross section in terms of quark-gluon opening angle θ and the *light cone momentum fraction* z in this way [62]

$$d\sigma = \sigma_0 \sum_{jets} C_F \frac{\alpha_S}{2\pi} \frac{d\theta}{\theta} dz \frac{1+(1-z)^2}{z}$$

which has a singularity for $z \to 0$ and $\theta \to 0$ and holds for every quantity that behaves like θ^2, as the transverse momentum ($p_T^2 = z^2(1-z)^2\theta^2E^2$) and the invariant mass ($m^2 = z(1-z)\theta^2E^2$). The cross section can be generalized with the *Universal Collinear Limit* [62]:

$$d\sigma = \sigma_0 C_F \frac{\alpha_S}{2\pi} \frac{d\theta^2}{\theta^2} P_i(z,s) ds$$

where $P_i(z,s)$ is the *Altarelli-Parisi splitting kernel*, a function depending on the kind of branching i and spin s.

Two partons can be resolved only after the introduction of a separation criteria, like $p_T^2 > Q_0^2$. The probability that there is an emission at an energy scale between q^2 and q^2+dq^2 is calculated through the splitting kernel function [62]

$$d\mathcal{P} = \frac{\alpha_S}{2\pi}\frac{dq^2}{q^2}\int_{Q_0^2/q^2}^{1-Q_0^2/q^2} dz P(z) \equiv \frac{dq^2}{q^2}\bar{P}(z)$$

Like in radioactive decays, the non-emission probability can be calculated between a higher and a lower energy scales Q^2 and q^2.

$$\frac{\Delta(Q^2,q^2)}{dq^2} = \Delta(Q^2,q^2)\frac{d\mathcal{P}}{dq^2}$$

$$\Delta(Q^2,q^2) = exp\left(-\int_{q^2}^{Q^2}\frac{dk^2}{k^2}\bar{P}(k^2)\right)$$

$$\Delta(Q^2,Q_0^2) \equiv \Delta(Q^2) \sim exp\left(-C_F\frac{\alpha_S}{2\pi}\log^2\frac{Q^2}{Q_0^2}\right)$$

The last equation defines the *Sudakov form factor* and represents the probability that the emitted radiation is non-resolvable (Figure 3.3).

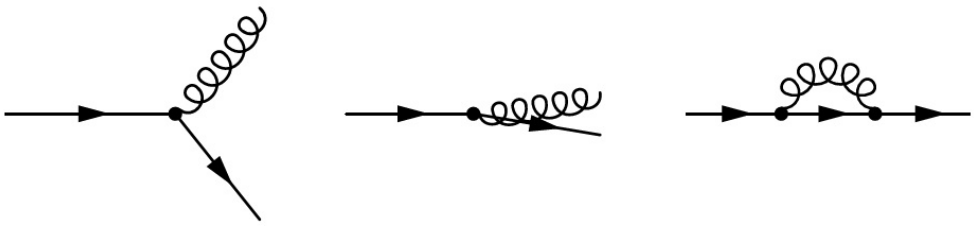

Figure 3.3: Resolvable (left), unresolvable (centre) and virtual (right) emissions

In order to preserve the unitarity,

$$P(resolved) + P(unresolved) + P(virtual) = 1$$

Choosing a starting scale Q^2, it is possible to generate branchings following

$$dP = \frac{dq^2}{q^2}\bar{P}(q^2)\Delta(Q^2,q^2)$$

Choosing random number uniformly distributed $0 < \rho < 1$, if $\rho < \Delta(Q^2, q^2)$ the evolution stops, otherwise one solves the equation $\rho = \Delta(Q^2, q^2)$ for q^2 as the emission scale of the next branching.

The evolution parameter can be θ^2 or p_T^2, which are formally on equal footing, but can lead to different calculations: in the case of *soft gluons* which are emitted at large angles this choice usually falls on the angular separation θ^2. Theoretically, soft gluons can interact with particles in the shower; however the radiation intensity is proportional to the coherent sum of emissions from the emitting parton. While angular ordering produces wide angle soft emission first, this is not obvious with other evolution-driving variables.

Hadronization

The absence of a well-known theory about a correct treatment of non-perturbative QCD makes the *Hadronization* one of the most complex steps of the Monte Carlo simulation: for this reason only phenomenological models are used. The first model which has been proposed was the *Independent Fragmentation Model* [63], based on the experimental observation that in $e^+e^- \to q\bar{q}$ events the number of produced hadrons is flat in rapidity while the p_T distribution is limited by an exponential $\rho(p_T^2) \sim exp(-p_T^2/2p_0^2)$. Using this approximation jet energy and momentum estimations become possible, but unfortunately the results are not satisfactory, since there is no obvious relation to perturbative emission, the model is not infrared safe (see section 4.1.1) and does not include confinement.

A more advanced model is the *Lund string model* [64], which is implemented in some Monte Carlo generators (like *Pythia*[65]). This model is based on the experimental observation that, at long distances, gluon self-interaction makes inter-quark field lines attract each other and the resulting potential could be approximated as

$$V(R) = V_0 + kR - e/R + f/R^2$$

with $k \sim 1$ GeV/fm. In this model the mass of a meson is $m^2 = 2k^2$ and $q\bar{q}$ pairs are created by tunneling with a probability $\sim e^{-b(m_q^2+p_T^2)}$. The parameters can be adjusted for each quark flavor and meson, starting from experimental measurements. As for the baryons, two quarks are considered tightly bounded, so that a "diquark" state is treated like an antiquark.

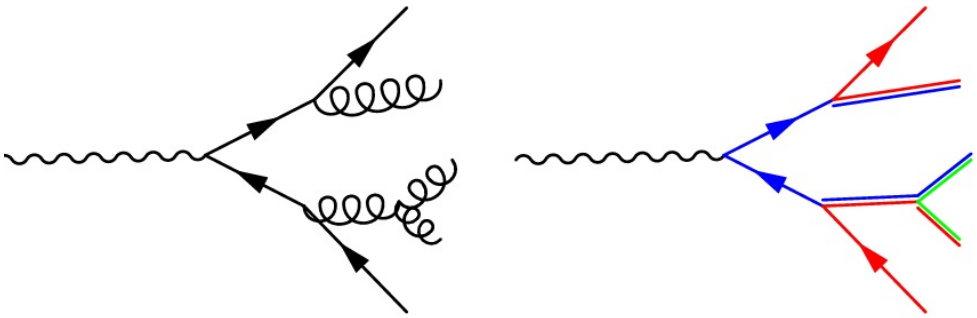

Figure 3.4: Cluster model: gluons are represented by colour-anticolour lines.

Another advanced hadronization model is the *Cluster Model* [66], based on the usage of colour charge flow (Figure 3.4). The colour-singlet pairs mass spectrum is asymptotically independent on energy and production mechanism and is peaked at a low mass Q_0. In this model the clusters represent mesonic resonances that decay to lighter resonances and stable hadrons, while the heavy hadron production is suppressed.

After the perturbative parton showering, all outgoing gluons are split non-perturbatively into quark-antiquark pairs so that only quarks can effectively give rise to particle jets, and each final state color line links a quark to an antiquark, like colour singlet clusters. Lighter hadrons are defined as fragments of the cluster, and if a cluster is too light to decay into two hadrons, is considered itself a hadron. This mechanism is not directly applicable to a fraction of clusters, which have too high masses: in this case, an iterative fission model is used until the mass of the daughter cluster is low enough.

In the *Herwig* MC generator [67], where the *Cluster Model* is implemented, the threshold over which a cluster is split is defined by the following

relation:

$$M_f^{CLPOW} = CLMAX^{CLPOW} + (m_{q1} + m_{q2})^{CLPOW}$$

where m_{q1} and m_{q2} are the quark nominal masses, $CLPOW$ and $CLMAX$ are free parameters. Usually, only few clusters need the fission model, so only the tail of the cluster mass spectrum is affected from changing these parameters. Unfortunately the tail of the spectrum is fundamental because the production rater of high p_T heavy particles strongly depend on it.

In this model the b-quark hadronization is still not satisfactory and needs another parameter ($B1LIM > 0$) to allow clusters with mass above $M_{B\pi}$ form a single B-meson if $M_f < (1 + B1LIM)M_{B\pi}$. With this parametrization, the probability of single meson decreases linearly for $M_{B\pi} < M_f < (1 + B1LIM)M_{B\pi}$ and the B-spectrum is hardened. Another way to describe better the bottom hadronisation is to use two different sets of $(CLPOW, CLMAX)$, one for b-quarks and one for the lighter quarks.

Decay

The decay products of strings and clusters are mainly unstable resonances, which decay themselves, following the PDG data tables [4].

Multiple Interaction and Beam Remnants

The hard scattering leaves two colour-charged object (the *remnants*) which in turn interact between each others. The approach to describe this interaction can be perturbative or non-perturbative. It has been studied [68] that for small minimum p_T and high $\sqrt{s}$ the inclusive parton-parton cross section is larger than the total proton-proton cross section, so every proton-proton event is characterized by many parton-parton interactions.

3.2.2 Monte Carlo Generators

Monte Carlo event generators are used to produce sets of simulated events, needed to characterize the detector response, estimate the detector efficency

and predict the background contributions from various physics processes. Every generator has different features, summarized in the following:

- *Pythia*[65] is a general purpose generator, which simulate scattering processes at leading order of QCD. Afterwards, QCD and QED radiations are added as approximations of parton showers. At the end of the showers, the hadronization of quark and gluons is described through the Lund String Model.

- *Herwig*[67] is another general purpose generator used with the same aims of *Pythia*, but with a different approach, describing the hadronization process with the Cluster Model. Through the *Jimmy* [69] library of routines it is possible to generate the so-called underlying events, like multiple parton scattering events in hadron-hadron, photon-photon or photon-hadron events

- *MC@NLO*[70] is a generator which simulates hard scattering events at Next-to-Leading Order of the QCD perturbative theory, giving a better description of the transverse momentum distribution than *Herwig*. Using the perturbative theory, several corrections are generated, along with their weights that must be taken into account. The overcounting of the events is avoided by subtracting from the exact NLO cross section its approximation which is implemented in the MC generator to which *MC@NLO* is matched in order to make the parton showering (like *Herwig*). In general, the result obtained with this subtraction is not positive defined: therefore *MC@NLO* can generate events with positive and negative weights. A distribution of a physical variable, containing events with both types of weights, with sufficiently high statistics should always provide positive (i.e. physically acceptable) results.

- *Powheg*[71] is another hard scattering generator at Next-to-Leading Order of the QCD perturbative theory, which was designed to overcome

the limits of *MC@NLO*: the dependence on the Monte Carlo generator used for the parton showering and the negative weights. *Powheg* generates the hardest radiation first, using the exact NLO matrix elements in order to obtain only positive-weighted events and the output can be matched for the parton showering to every generator which is p_T-ordered or allows the implementation of a p_T veto.

- *Alpgen*[72] is a generator which is designed to provide a better description of final states containing a large number of partons originated from the hard scattering, for which the fixed order QCD matrix element can give a better approximation than the one obtained through *Herwig* or*Pythia*.

- *AcerMC*[73] is a hard process generator which is dedicated to the generation of Standard Model background processes at pp LHC collisions, providing a library of massive matrix elements and phase space modules for generation of a set of selected processes, like $gg, q\bar{q} \to t\bar{t}b\bar{b}$, $q\bar{q}W(\to \ell\nu)b\bar{b}$, $q\bar{q}W(\to \ell\nu)t\bar{t}$, $gg, q\bar{q} \to Z/\gamma^*(\to \ell\ell)b\bar{b}$, $gg, q\bar{q} \to Z/\gamma^*(\to \ell\ell, \nu\nu, b\bar{b})t\bar{t}$ and $gg \to (Z/W/\gamma^* \to)b\bar{b}t\bar{t}$. The hard process generated with these modules, with a phase-space generation based on a multichannel self-optimizing approach, can be completed using the initial/final state radiation, hadronization and decays provided by *Herwig* or *Pythia* generator.

- *Sherpa* [74] is a generator which matches fixed-order QCD matrix elements to QCD showers using the Catani-Krauss-Kuhn-Webber duplicate removal prescription [75]. It is interfaced to *Pythia*'s hadronization model and produces complete events which give better approximations for final states with large number of isolated jets than other generators based on pure QCD showering, such like *Pythia* and *Herwig*.

3.2.3 Simulated samples

The simulated Monte Carlo samples used in this analysis are from the ATLAS MC12 production campaign. In order to be coherent with the real data sample, the generated events have been processed through a detailed model of the ATLAS detector implemented in the program GEANT4[76].

The $t\bar{t}$ signal has been generated with *Powheg* using the CT10 parton distribution function set[77] for the hard scattering, while the parton shower and the hadronization have been performed with *Pythia*. In order to estimate the generator systematic uncertainty, these simulations have been compared with the ones obtained with *Powheg+Herwig* and *MC@NLO+Herwig*. The simulation of vector boson production has been made at Leading Order with *Alpgen* using the CTEQ6L1 parton distribution function set [78] and making the parton showering with *Pythia*, producing samples with several final state jet multiplicities and enriched with jets from heavy flavors. The production of the single top quark is simulated using *AcerMC* for the t-channel and *Powheg* for the s-channel and the Wt production. In both cases the CTEQ6L1 parton distribution functions set and the *Pythia* parton showering have been used. Diboson production is modeled using *Sherpa* with the CT10 parton distribution function set.

Details on the MC samples used in the analysis are shown in Tables 3.1-3.7. In the analysis, every sample is rescaled to the luminosity of the data, taking into account the number of generated events and the cross section of the processes. Finally, every weight is rescaled by a k factor, which corrects for the recent Next-to-Next-to-Leading Order calculation from the previous Next-to-Leading Order calculations.

ID	Description	ME+PS	σ [pb]	k-factor
117050	$t\bar{t}$ (no all hadr.)	Powheg+Pythia	114.49	1.1994
117075	$t\bar{t}$ (no all hadr.) with 1.1 TeV $< m_{t\bar{t}} \leq$ 1.3 TeV	Powheg+Pythia	0.61073	1.1994
117076	$t\bar{t}$ (no all hadr.) with 1.3 TeV $< m_{t\bar{t}} \leq$ TeV	Powheg+Pythia	0.21459	1.1994
117077	$t\bar{t}$ (no all hadr.) with 1.5 TeV $< m_{t\bar{t}} \leq$ 1.7 TeV	Powheg+Pythia	0.081171	1.1994
117078	$t\bar{t}$ (no all hadr.) with 1.7 TeV $< m_{t\bar{t}} \leq$ 2.0 TeV	Powheg+Pythia	0.041004	1.1994
117079	$t\bar{t}$ (no all hadr.) with $m_{t\bar{t}} >$ 2.0 TeV	Powheg+Pythia	0.016542	1.1994

Table 3.1: $t\bar{t}$ samples which do not include all hadronic decays (No full-had).

ID	Description	ME+PS	σ [pb]	k-factor
110101	t-channel (lept.)	AcerMC+Pythia	25.750	1.1042
110119	s-channel (lept.)	Powheg+Pythia	1.6424	1.1067
110140	Wt-channel (incl.)	Powheg+Pythia	20.461	1.0933

Table 3.2: Single top samples.

ID	Description	ME+PS	σ [pb]	k-factor
183585	$ZW \to eeqq$ with up to 3p and massive c,b quarks	Sherpa	1.4622	1.0500
183586	$ZZ \to eeqq$ with up to 3p and massive c,b quarks	Sherpa	0.24854	1.0000
183587	$ZW \to \mu\mu qq$ with up to 3p and massive c,b quarks	Sherpa	1.4624	1.0500
183588	$ZZ \to \mu\mu qq$ with up to 3p and massive c,b quarks	Sherpa	0.24747	1.0000
183589	$ZW \to \tau\tau qq$ with up to 3p and massive c,b quarks	Sherpa	1.4523	1.0500
183590	$ZZ \to \tau\tau qq$ with up to 3p and massive c,b quarks	Sherpa	0.24167	1.0000
183734	$WW \to e\nu qq$ with up to 3p and massive c,b quarks	Sherpa	7.2790	1.0600
183735	$WZ \to e\nu qq$ with up to 3p and massive c,b quarks	Sherpa	1.9022	1.0500
183736	$WW \to \mu\nu qq$ with up to 3p and massive c,b quarks	Sherpa	7.2776	1.0600
183737	$WZ \to \mu\nu qq$ with up to 3p and massive c,b quarks	Sherpa	1.9076	1.0500
183738	$WW \to \tau\nu qq$ with up to 3p and massive c,b quarks	Sherpa	7.2756	1.0600
183739	$WZ \to \tau\nu qq$ with up to 3p and massive c,b quarks	Sherpa	1.9086	1.0500

Table 3.3: Background samples containing $WW/WZ/ZZ$.

ID	Description	ME+PS	σ [pb]	k-factor
190001	$W \to e\nu + 1p$	AlpGen+Pythia	0.71565	1.1330
190002	$W \to e\nu + 2p$	AlpGen+Pythia	1.9920	1.1330
190003	$W \to e\nu + 3p$	AlpGen+Pythia	2.2144	1.1330
190004	$W \to e\nu + 4p$	AlpGen+Pythia	1.4867	1.1330
190005	$W \to e\nu + 5p$	AlpGen+Pythia	1.1185	1.1330
190011	$W \to \mu\nu + 1p$	AlpGen+Pythia	0.70640	1.1330
190012	$W \to \mu\nu + 2p$	AlpGen+Pythia	1.9221	1.1330
190013	$W \to \mu\nu + 3p$	AlpGen+Pythia	2.1249	1.1330
190014	$W \to \mu\nu + 4p$	AlpGen+Pythia	1.4169	1.1330
190015	$W \to \mu\nu + 5p$	AlpGen+Pythia	1.0612	1.1330
190021	$W \to \tau\nu + 1p$	AlpGen+Pythia	0.70468	1.1330
190022	$W \to \tau\nu + 2p$	AlpGen+Pythia	1.9309	1.1330
190023	$W \to \tau\nu + 3p$	AlpGen+Pythia	2.1416	1.1330
190024	$W \to \tau\nu + 4p$	AlpGen+Pythia	1.4297	1.1330
190025	$W \to \tau\nu + 5p$	AlpGen+Pythia	1.0705	1.1330

Table 3.4: Background samples containing W + light jets. A filter selecting anti-k_T jets with $R = 1.0$ and $m \geq 250$ GeV is applied.

ID	Description	ME+PS	σ [pb]	k-factor
190050	$W + bb$	AlpGen+Pythia	0.012462	1.1330
190051	$W + bb + 1p$	AlpGen+Pythia	0.11981	1.1330
190052	$W + bb + 2p$	AlpGen+Pythia	0.28254	1.1330
190053	$W + bb + 3p$	AlpGen+Pythia	0.73213	1.1330
190040	$W + cc$	AlpGen+Pythia	0.013282	1.1330
190041	$W + cc + 1p$	AlpGen+Pythia	0.22439	1.1330
190042	$W + cc + 2p$	AlpGen+Pythia	0.69188	1.1330
190043	$W + cc + 3p$	AlpGen+Pythia	1.7859	1.1330
190030	$W + c$	AlpGen+Pythia	0.087468	1.5200
190031	$W + c + 1p$	AlpGen+Pythia	0.47215	1.5200
190032	$W + c + 2p$	AlpGen+Pythia	0.56999	1.5200
190033	$W + c + 3p$	AlpGen+Pythia	0.37909	1.5200
190034	$W + c + 4p$	AlpGen+Pythia	0.29910	1.5200

Table 3.5: Background samples containing W + heavy quarks (c and b). A filter selecting anti-k_T jets with $R = 1.0$ and $m \geq 250$ GeV is applied.

ID	Description	ME+PS	σ [pb]	k-factor
147105	$Z \to ee$	AlpGen+Pythia	718.97	1.1800
147106	$Z \to ee + 1p$	AlpGen+Pythia	175.70	1.1800
147107	$Z \to ee + 2p$	AlpGen+Pythia	58.760	1.1800
147108	$Z \to ee + 3p$	AlpGen+Pythia	15.636	1.1800
147109	$Z \to ee + 4p$	AlpGen+Pythia	4.0116	1.1800
147110	$Z \to ee + \geq 5p$	AlpGen+Pythia	1.2592	1.1800
147113	$Z \to \mu\mu$	AlpGen+Pythia	719.16	1.1800
147114	$Z \to \mu\mu + 1p$	AlpGen+Pythia	175.74	1.1800
147115	$Z \to \mu\mu + 2p$	AlpGen+Pythia	58.795	1.1800
147116	$Z \to \mu\mu + 3p$	AlpGen+Pythia	15.673	1.1800
147117	$Z \to \mu\mu + 4p$	AlpGen+Pythia	4.0057	1.1800
147118	$Z \to \mu\mu + \geq 5p$	AlpGen+Pythia	1.2543	1.1800
147121	$Z \to \tau\tau$	AlpGen+Pythia	718.87	1.1800
147122	$Z \to \tau\tau + 1p$	AlpGen+Pythia	175.76	1.1800
147123	$Z \to \tau\tau + 2p$	AlpGen+Pythia	58.856	1.1800
147124	$Z \to \tau\tau + 3p$	AlpGen+Pythia	15.667	1.1800
147125	$Z \to \tau\tau + 4p$	AlpGen+Pythia	4.0121	1.1800
147126	$Z \to \tau\tau + \geq 5p$	AlpGen+Pythia	1.2561	1.1800

Table 3.6: Background samples of Z/γ^* +jets processes.

ID	Description	ME+PS	σ [pb]	k-factor
200332	$Z \to ee + bb$	AlpGen+Pythia	6.5083	1.1800
200333	$Z \to ee + bb + 1p$	AlpGen+Pythia	3.2948	1.1800
200334	$Z \to ee + bb + 2p$	AlpGen+Pythia	1.2546	1.1800
200335	$Z \to ee + bb+ \geq 3p$	AlpGen+Pythia	0.61800	1.1800
200340	$Z \to \mu\mu + bb$	AlpGen+Pythia	6.5056	1.1800
200341	$Z \to \mu\mu + bb + 1p$	AlpGen+Pythia	3.2909	1.1800
200342	$Z \to \mu\mu + bb + 2p$	AlpGen+Pythia	1.2585	1.1800
200343	$Z \to \mu\mu + bb+ \geq 3p$	AlpGen+Pythia	0.61808	1.1800
200348	$Z \to \tau\tau + bb$	AlpGen+Pythia	6.5062	1.1800
200349	$Z \to \tau\tau + bb + 1p$	AlpGen+Pythia	3.2935	1.1800
200350	$Z \to \tau\tau + bb + 2p$	AlpGen+Pythia	1.2485	1.1800
200351	$Z \to \tau\tau + bb+ \geq 3p$	AlpGen+Pythia	0.61363	1.1800
200432	$Z \to ee + cc$	AlpGen+Pythia	11.763	1.1800
200433	$Z \to ee + cc + 1p$	AlpGen+Pythia	7.1249	1.1800
200434	$Z \to ee + cc + 2p$	AlpGen+Pythia	3.3656	1.1800
200435	$Z \to ee + cc+ \geq 3p$	AlpGen+Pythia	1.7010	1.1800
200440	$Z \to \mu\mu + cc$	AlpGen+Pythia	11.795	1.1800
200441	$Z \to \mu\mu + cc + 1p$	AlpGen+Pythia	7.1254	1.1800
200442	$Z \to \mu\mu + cc + 2p$	AlpGen+Pythia	3.3694	1.1800
200443	$Z \to \mu\mu + cc+ \geq 3p$	AlpGen+Pythia	1.7003	1.1800
200448	$Z \to \tau\tau + cc$	AlpGen+Pythia	11.760	1.1800
200449	$Z \to \tau\tau + cc + 1p$	AlpGen+Pythia	7.1410	1.1800
200450	$Z \to \tau\tau + cc + 2p$	AlpGen+Pythia	3.3582	1.1800
200451	$Z \to \tau\tau + cc+ \geq 3p$	AlpGen+Pythia	1.7046	1.1800

Table 3.7: Background samples containing Z + heavy quarks (c and b).

Chapter 4

Particle identification and event selection

4.1 Particle identification

Depending on the decay products in the final state, the $t\bar{t}$ events could be divided into three channels: full-hadronic, lepton+jets and di-leptonic. The high contamination of the QCD background in the detection of events in the fully-hadronic channel and the low statistics in the di-leptonic channel make the lepton+jets channel the favourite final state for this analysis.

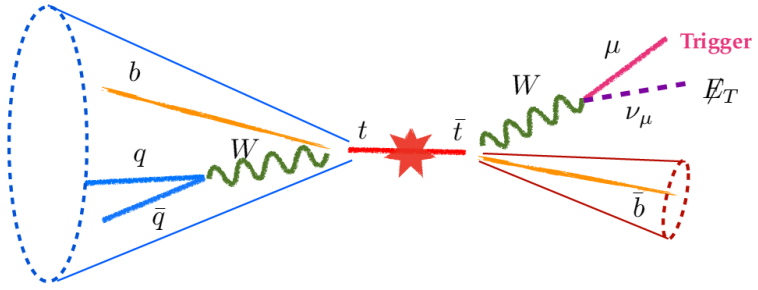

Figure 4.1: A typical boosted $t\bar{t}$ event in the semi-leptonic channel

In the lepton+jets final state one top decays into a b quark and a quark-antiquark pair, while the other top decays into another b quark, a charged lepton and a neutrino. So, the experimental signature of this kind of $t\bar{t}$

events is characterized by a large value of missing transverse energy and by the presence of at least one lepton and 4 jets, two of which originated by b quarks.

While in general the signal is characterized by four isolated jets, when the top quarks are produced in boosted regime ($p_T > m_t$) their decay products can partially overlap and the standard selection methods looses efficiency. In general, the boosted objects are studied searching for bigger jets, which contain all the products of the top quarks that decay hadronically. Many algorithms are studied in order to investigate the substructure of these jets, reconstructing and measuring the proprieties of the decay products.

The ATLAS detector is able to give information about most of the particles which are involved in the decays of $t\bar{t}$ pairs, and to give an estimation of the missing transverse energy, due to neutrinos. The presence of an high energy lepton coming from the decay of the W boson is a key ingredient for the event identification with an efficient single lepton trigger. Electrons are often totally absorbed by the electromagnetic calorimeter, and can be distinguished from the photons because they leave a track in the inner tracker which points to a cluster inside the calorimeter. Muons, being the most penetrating particles, reach the outer layers of the detector, until reaching the muon spectrometer. They can be identified also because of the low ionization that characterizes their path through the internal layers of the detector.

The neutrinos are the only particles involved in this decay that are not detected directly by ATLAS, due to their feeble interactions in matter. It is assumed, therefore, that a possible lack of measured energy in the transverse plane is due to the presence of neutrinos or to instrumental uncertainties and bad reconstruction.

Since the principal background of the lepton+jets channel is made of $W + 4\,jet \rightarrow (l\nu)+4\,jet$ events (which have a signature similar to that of the signal), reconstruction and classification of jets are fundamental: while the four jets of the signal are tagged as two light and two b-flavoured jets, in background events the four jets are mainly light. The b-jets, due to hadronization of the

b quark, can be distinguished from the others. In fact, hadrons containing b quarks are characterized by a mean lifetime which is sufficiently long to make them move by a few millimeters before decaying. So a secondary vertex is present and associated to jets originated by b quarks.

All the criteria for the particle identification, event selection and system reconstruction used in the boosted $t\bar{t}$ analysis will be shown in detail in the following sections.

4.1.1 Jets

The hadronization of the free quarks and gluons present in the event lead to the production of jets, whose characteristics are linked to the one of their parent partons. The jet reconstruction algorithms take as input the four-momentum of the cells of the electromagnetic and hadronic calorimeters, characterized by a different granularity. Because there are more than $2 \cdot 10^6$ cells of different format, it is important to group the information in an effective way in order to give the right input to the reconstruction algorithms. The method used in this analysis uses the *topological cell clusters* method [79].

The *topological cell clusters* method follows the development of the particle shower in a three-dimensional space. If some cells have a signal/background ratio which is larger than 4, they pass a first selection. If the adjacent cells have a ratio larger than 2, they are added to the cluster. Finally, if the adjacent cells have any signal over threshold, they are added to the cluster as well.

Once the inputs are made, they are analyzed by the reconstruction algorithms. In order to reconstruct jets precisely and efficiently, generic guide lines should be followed.

First of all, the jet reconstruction must be *infrared safe*: the presence of additional soft particles between two particles belonging to the same jet should not affect the combination of these two particles into a jet. Generally, any soft particles not coming from the fragmentation of a hard scattered

parton should not affect the number of jets reconstructed.

The jet reconstruction algorithm must be also *collinear safe*: a jet should be independent of the fact that a certain amount of momentum is carried by one particle or if it is split into two collinear particles.

The algorithm must be *order independent*: the same hard scattering should be reconstructed independently at *parton*, *particle* or *detector level*.

In addition, the reconstruction algorithm must give results as much as possible independent on the characteristics of the detector, like its resolution, and external events like multiple interactions or sudden changes in luminosity. It should also be taken into account that any algorithm used in ATLAS has to manage an impressive amount of data: it is therefore necessary to be as fast as possible.

Iterative seeded fixed-cone

The first and simplest algorithm used to recognize jets is the *iterative seeded fixed-cone*. In this algorithm, all objects are sorted by decreasing transverse momentum. If an object exceeds a threshold of 1GeV/c, all objects in the cone in the space (η, ϕ) of radius

$$\Delta R = \sqrt{\Delta\eta^2 + \Delta\phi^2} \leq R$$

are combined to form a single object.

In ATLAS it is usually used $R = 0.4$ for narrow jets. A new direction for the cone axis is then calculated through the sum of the four-momentum of the combined objects. This process is repeated iteratively until the new direction of the cone does not deviate from the direction calculated previously. The stable cone which is determined will correspond to a jet.

Even if this algorithm is fast and simple, it has some defect: the infrared safe condition is not respected. To solve this problem, the constituents of the jets are analyzed: jets which share the constituents with more than 50% of p_T of the less energetic jet are summed .

Sequential recombination

There is another algorithm to reconstruct jets, called *sequential recombination* or *clustering*, which analyzes iteratively all the input pairs (i, j) taking into account their transverse momentum [80].

In this approach it is considered the formula

$$d_{ij} = min\left(p_{T,i}^{2n}, p_{T,j}^{2n}\right) \frac{\Delta R_{ij}^2}{R^2} = min\left(p_{T,i}^{2n}, p_{T,j}^{2n}\right) \frac{\Delta\eta^2 + \Delta\phi^2}{R^2}$$

where n and R are free parameters. Comparing the different pair combinations, the one linked to the lower d_{ij} is replaced with an object k whose four-momentum is the sum of the two input's four-momenta. This procedure is repeated until the available inputs are finished. The size of the jets is controlled by the free parameter R, which usually has a value of 0.4 in ATLAS analysis.

With respect to the *cone* algorithms, the *clustering* approach respect all the guide lines previously listed. Depending on the value of the free parameter n there will be different reconstruction algorithms: for $n = 0$ the p_T is not considered and the algorithm is called *Cambridge*, for $n = 1$ it is called *Kt*, while for $n = -1$ it is called *Anti Kt*. Studies have concluded that the best *clustering* algorithm for the LHC experiments is the *Anti Kt* algorithm, because of its accuracy in the Next-To-Leading Order studies[81].

Jet calibration

The energy scale and resolution of jets (JES and JER) are calibrated through scale factors depending on transverse momentum and pseudorapidity, which make the measured values correspond on average to the ones of the truth-level jets built from the stable particles produced by Monte Carlo simulation.

The calculation of this scale factor has been integrated also with data-driven techniques, using jets reconstructed in the ATLAS calorimeters from well calibrated photon+jets events at $\sqrt{s} = 8$ TeV [82]. The pseudorapidity dependence of the jet response has been studied through the transverse

momentum balance. A residual transverse momentum and pseudorapidity-dependent jet calibration is derived for jets in data, in order to improve the default MC-based calibration, obtaining a variety of scale factors which range from 0.96 to 1.02 depending on the pseudorapidity of the jet. The jet energy scale calibration for high-p_T central jets has been measured looking for isolated high-p_T jets recoiling against a system of low-p_T jets, finding a general agreement between data and simulation for jets with transverse momentum up to 1.7 TeV. Meanwhile, also the jet energy resolution is measured through the transverse momentum balance of jets in the photon+jets events, finding that it is well reproduced in the simulation.

Pile-up rejection

The multiple pp collisions within the same bunch crossing lead to the production of a large amount of particles not belonging to the primary interaction vertex (*pile-up*). Indeed, the *pile-up* products can overlap with the physically interesting objects, modifying the values of their properties, or can be reconstructed as fake jets. So, the jet calibration has to be corrected by removing the average additional energy due to *pile-up* interactions from the energy measured by the calorimeters. The corrections depend on the number of reconstructed primary vertices (NPV), the jet pseudorapidity (η) and the bunch spacing, and are obtained from *in situ* measurements made with minimum bias data.

On the other hand, the rejection of fake jets is done exploiting the Jet Vertex Fraction (JVF)[83], which is the fraction between the number of p_T-matched tracks originating from the primary interaction vertex and all the tracks associated to the jet. The best compromise between a good rejection of *pile-up* events and an efficient selection of hard scatter jets is a cut on $|JVF| < 0.5$ for jets with $p_T < 50$ GeV.

4.1.2 Large-R jets

When a top quark has a large Lorentz boost ($\beta \gtrsim 0.87$), his decay products tend to be collimated, as sketched in Figure 4.2. For this reason, the standard selection of lepton+jets $t\bar{t}$ events, which usually requires the presence of well separated objects, become less efficient.

In particular, the jets coming from the hadronically decaying top quark overlap, and it is more efficient to reconstruct it as a high-p_T large-R jet, containing all the final state particles. In this study the large-R jets are reconstructed using the anti-k_T algorithm with radius parameter $R = 1$ and using as input calibrated topological clusters.

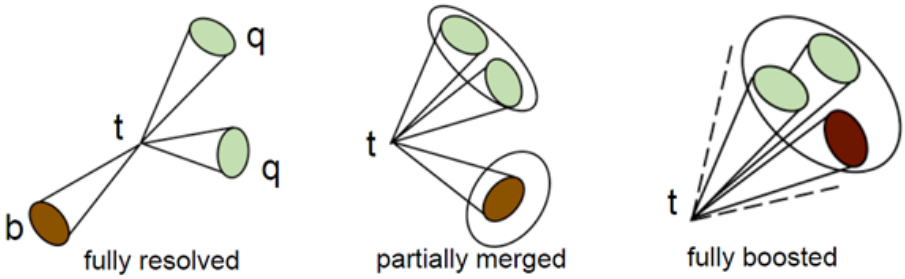

Figure 4.2: Graphical examples of resolved and boosted topologies.

The p_T and the mass of these jets, which are obtained from the four-momentum sum of all their constituents, are calibrated using correction factors depending on energy and η, in order to be on average as close as possible to the truth-level values, which are the ones of the stable particles produced by the MC event generator.

Since the reconstruction of this kind of object can be affected by initial state radiation, multiple parton interactions and pile-up effects, a trimming algorythm [84] is applied.

Trimming the large-R jets

The jet trimming procedure reclusters "seed" jets through a sub-jet finding method. These sub-jets could be clustered with a different algorithm with

respect to the former "seed" jets, and are characterized by a smaller radius R_{sub}. Then, the sub-jets must pass a softness criteria before determining the bigger trimmed jets: the contribution of the sub-jet i is discarded if $p_{T,i}/p_{T,seed} < f_{cut}$, where f_{cut} is a fixed dimensionless parameter. The whole procedure is shown in Figure 4.3

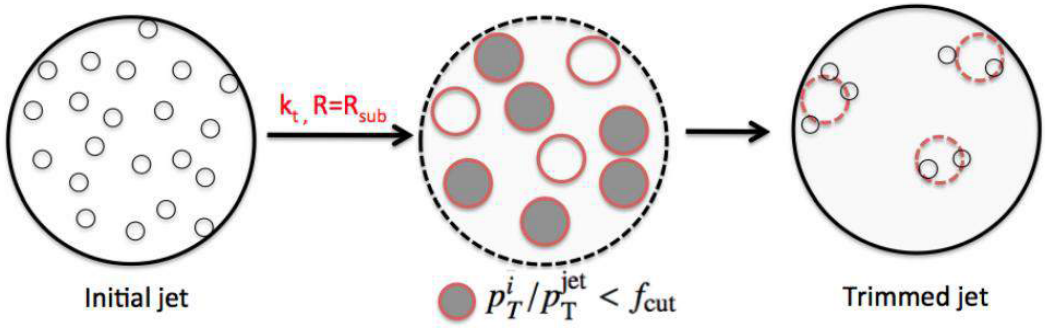

Figure 4.3: Graphical explaination of the jet trimming procedure.

In this analysis, the large-R jets are used as "seed" jets, to be reclustered with sub-jets which are reconstructed with the k_T algorithm and selected applying $R_{sub} = 0.3$ and $f_{cut} = 0.05$ as parameters. The trimmed large-R jets which are considered for the analysis fall in the fiducial region $|\eta| < 2.0$ and $p_T < 300$ GeV.

Typically, a jet from light quarks or gluons lose about 30-50% of its mass, while for jets coming from heavy particles this loss of weight is usually limited to a few percent, corresponding to the *pile-up* background.

Some particular jet variables, called substructed variables, can be used after the trimming to obtain a better signal/background discrimination. This analysis exploits the *jet mass* and the *splitting scale*. The *jet mass*, which is defined as

$$(m^{jet})^2 = (\sum_i E_i)^2 - (\sum_i p_i)^2$$

where E_i and p_i are the energy and the momentum of the i^{th} jet constituent, supposing that each energy deposit is given by massless particles.

Considering that the sub-jets are reconstructed using the k_T algorithm, it is possible to discriminate a hard substructure through the *splitting scale* $\sqrt{d_{12}}$ between the two sub-jets identified in the last step of the reconstruction. The splitting scale is defined as

$$\sqrt{d_{12}} = min(p_{T,1}, p_{T,2}) \cdot \Delta R_{12}$$

where ΔR_{12} is the distance between the last two jet constituents in the iteractions of the sequential recombination.

4.1.3 The *b-tagging*

Since almost every top quark decays into a W boson and bottom quark, one way to reduce the background contamination is to select events with jets containing b-quarks. The *b-tagging* algorithms are generally based on the long lifetime of the particles containing the bottom quark. The *b-tagging* is a combination of three algorithms: *JetFitter*, *IP3D* and *SV1* [85].

JetFitter uses the topology of weak decays of b-hadron and c-hadron in the jet, defining with a Kalman Filter a common line on which the primary vertex and the hadron decay vertices lie, as well as their position on this line, giving an approximated flight path for the b-hadron.

The *IP3D* tagger doesn't reconstruct directly decay vertices or flight paths, but uses the significances of the tracks' impact parameters in the longitudinal and transverse plane, to calculate a likelihood probability for the jet to arise from a *b*-quark.

The *SV1* algorithm looks for secondary vertices due to a *b*-quark decay, making all the possible pairs of tracks. The right vertex is found minimizing a χ^2, based on the 1-dimensional distribution of the number of vertices made by the track pairs, on the 2-dimensional distribution of the invariant masses of the tracks, on the ratio between the sum of the energies of the vertex' tracks and the sum of the energies of the jet.

These three taggers are combined, and the weights of the combination (together with the p_T and η of the jet) are used as input to multi-variate

analysis with a neural network (called *MV1-tagger*)[86] which determines a discriminant variable. The threshold value of the discriminant variable is tuned in order to select b-jets with a 70% efficiency, corresponding to a rejection factor for the light jets of the order of several hundreds.

4.1.4 Electrons

The electron reconstruction is based on a combined analysis of the tracks in the Inner Tracker and the clusters reconstructed in the electromagnetic calorimeter. Two different reconstruction algorithms are used in ATLAS analyses[79].

The standard one starts from a signal in the electromagnetic calorimeter and is designed to find correspondences with the tracks in the Inner Tracker. The second algorithm, on the contrary, is activated by the presence of low momentum tracks (of the order of 1 GeV) in the Inner Tracker and is designed to find correspondences with the signals of the electromagnetic calorimeter.

While the energy of the electron is determined using the calorimeter information, the particle direction at the production vertex comes from the inner tracker. The corrections applied to the measured cluster energy are based on precise Monte Carlo simulations validated by comprehensive measurements with 900 GeV data [87].

To be identified, the electrons must satisfy a series of requirements. There are three selections, which corresponds to three different definitions of electrons: *loose*, *medium* and *tight*.

The *loose* electrons are selected through the partial information obtained by the calorimeters. A set of requirements is made on the the shape of the electromagnetic shower observed in the calorimeter. Such requirements have large efficiency, but a poor discrimination between signal and background.

With respect to the *loose* electrons, the *medium* ones are selected with additional cuts which reduce the background from events like $\pi^0 \rightarrow \gamma\gamma$. The selection is made checking the second maximum energy released in the calorimeter $\Delta E_{max,2}$, the difference between this energy and the minimum one

$\Delta E_s = E_{max,2} - E_{min}$ and the width of the shower detected in the calorimeter. Through several cuts on these observables, there is a jet reduction of a factor 3 with respect to the loose selection with a decrease of efficiency of only 10%.

Finally, the *tight* electrons are selected adding another set of cuts, which further increase the purity respect to the *medium* ones. It is checked if there are no secondary vertices, in order to avoid electrons originated by photon conversions and heavy meson decays. Also a threshold on the momentum of the tracks is applied, in order to avoid background contamination.

The electron reconstruction efficency as a function of the number of primary vertices and the reconstructed Z boson mass using tight electrons are shown in Figure 4.4.

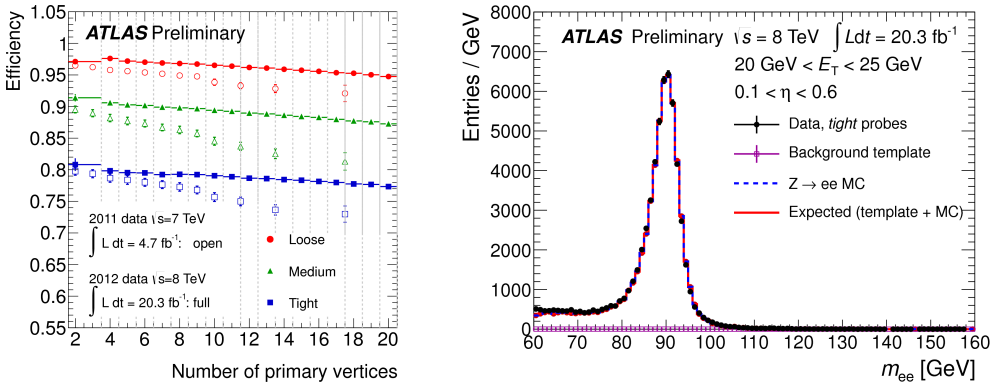

Figure 4.4: Electron efficiency measurements with a tag-and-probe method [88]. Left: identification efficiency in data for the various cut-based selections measured with 2011 and 2012 data as a function of the number of reconstructed primary vertices. Right: recostruction of the Z mass using reconstructed *tight* electrons in a $Z \to ee$ sample, with tagged electrons of 20 GeV$< E_T <$25 GeV and $0.1 < \eta < 0.6$.

Online and offline electron selection in the analysis

The online selection of the electrons is performed using the `EF_e24vhi_medium1` or `EF_e60_medium1` triggers, which require the presence of a candidate electron with $p_T > 24$ GeV (for isolated electrons) or $p_T > 60$ GeV for non isolated ones. These triggers are also simulated in the Monte Carlo samples.

The triggered electrons have to satisfy other offline criteria in order to be selected for the analysis:

- There should not be errors in the Liquid Argon electromagnetic calorimeter during the data taking.

- The quality definition of the electron chosen for the analysis is a particular variant of the *tight* criteria called *tight++* which include stringent selection cuts on calorimeter, tracking and combined variables, in order to have good separation between isolated electrons and jets. The *tight++* algorithm working points have been set in order to have an efficiency of 78%, after an evaluation performed with a Z boson sample.

- The distance between the track impact parameter and the z component of the primary vertex ($|Z_0^{PV}|$) should be less than 2 mm.

- The pseudorapidity of the clusters formed by the candidates in the Calorimeter has to be $|\eta_{cl}| < 2.47$, excluding the transition region of $1.37 < |\eta_{cl}| < 1.52$.

- The transverse energy has to be $E_T > 25$ GeV, where $E_T = \frac{E_{cl}}{\cosh \eta_{track}}$.

- Every electron should be isolated in order to avoid background from jets misidentifid as leptons. Considering the collimation of the top decay products in boosted topology, a "mini-isolation" criterion [89] is used, leading to an isolation cone radius decreasing with increasing p_T of the leptons. The isolation variable is defined as $I_{mini} = \sum_{tracks} \frac{p_T track}{p_T^e}$, where p_T^e is the electron transverse momentum and the sum is over all tracks (excluding the electron candidate track) that have $p_T > 0.4$ GeV, pass quality cuts and have $\Delta R(track, e) < \frac{K_T}{p_T^e}$. The parameter K_T is set to 10 GeV and the "mini-isolation" requirement is $I_{mini} < 0.05$.

- In order to avoid the ambiguities between electron energy deposits in calorimeters and jet signals, an overlap removal is applied. Every jet

which is close to an electron ($\Delta R(e, j_{R=0.4}) < 0.4$) is corrected by subtracting the electron four-vector from the jet four-vector and the JVF is recalculated after removing the electron track. The new electron-subtracted jet must satisfy the usual selection criteria to be retained for the analysis. After this procedure, all electrons that are still within $\Delta R(e, j_{R=0.4}) < 0.2$ from a jet are removed.

4.1.5 Muons

The muon reconstruction can be made through two algorithm families, MuID[90] and STACO[91], which are used by three complementary identification processes [79]. The so called *standalone* process uses both the algorithms to reconstruct the passage of a muon observing the tracks in the Muon Spectrometer, and extrapolating to the beam axis the passage of the particles inside the calorimeter. The information about the energy lost by the particle is extracted from the calorimeter. This reconstruction process covers a larger area than the one covered using only the Inner Tracker ($|\eta| < 2.7$ instead of $|\eta| < 2.5$), but there is no information around $\eta = 0$ and 1.2. In addition, through this process there could be an important background of reconstructed muons which are produced inside the calorimeter from the hadronic interactions with the calorimeter material.

A second reconstruction process is the so called *tagging*, which takes the information from the Inner Tracker and combines it with the ones of the Calorimeter or the Muon Spectrometer. This process is less sensitive to Coulomb scattering and energy loss, resulting more efficient in finding low energy muons in regions which are not covered by the Muon Spectrometer.

The third reconstruction process is the *combined* one, which finds a correspondence between the tracks detected in the Muon Spectrometers and the ones of the Inner Tracker. The track combination has to minimize the χ^2 defined as

$$\chi^2 = \left(\vec{T}_{MS} - \vec{T}_{IT}\right)^T (C_{IT} + C_{MS})^{-1} \left(\vec{T}_{MS} - \vec{T}_{IT}\right)$$

where $\vec{T}$ is the 5 parameters vector of the track, taken in the closest point to the beam axis, and C is its covariance matrix.

The muon reconstruction efficency combining *combined* and *standalone* processes with respect to the p_T and the overall number of *pile-up* interactions in the event is shown in Figure 4.5.

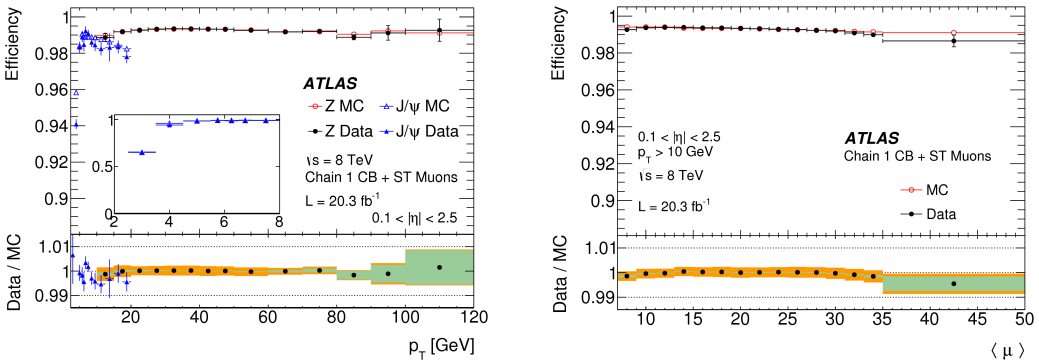

Figure 4.5: Left: reconstruction efficiency for *combined* (CB) and *standalone* (ST) muons as a function of the p_T of the muon, for muons with $0.1 < |\eta| < 2.5$, obtained with $Z \to \mu\mu$ and $J/\Psi \to \mu\mu$ events. Right: measured CB+ST muon reconstruction efficiency for muons with $p_T > 10$ GeV as a function of the average number of inelastic pp collisions per bunch crossing (μ), obtained with $Z \to \mu\mu$. [92]

Online and offline muon selection in the analysis

The triggers used in this analysis for the online event selection of the single muon channel are `EF_mu24i_tight` and `EF_mu36_tight`, which require the presence of a candidate muon with $p_T > 24$ GeV (for isolated muons) or $p_T > 36$ GeV for non isolated ones. These triggers are also simulated in the Monte Carlo samples.

The muon candidates have then to pass the following requirements for the offline selection:

- Muons have to be reconstructed with the MuID algorithm.

- Muons must be identified as *tight*, which means *combined* or *standalone* muons with at least three MDT+CSC hits.

- The distance between the track impact parameter and the z component of the primary vertex ($|Z_0^{PV}|$) should be less than 2 mm.

- The transverse impact parameter of the track (d_0) should be consistent with coming from a hard scattering, $\left|\frac{d_0}{\sigma(d_0)}\right| < 3$.

- Muons have to be within the detector acceptance of the ID and MS, $|\eta| < 2.5$.

- Muons must have transverse momentum $p_T > 25$ GeV.

- In order to avoid an overlap between the muon energy deposit in the calorimeter and jets, every muon which fall inside a cone of $\Delta R(\mu, j_{R=0.4}) < 0.04 + 10\ \text{GeV}/p_{T,\mu}$ around a jet axis is removed.

- Like the electrons, also the candidate muons have to pass a "mini-isolation" criterion [89], in order to avoid background leptons from jets. The isolation variable $I_{mini} = \sum_{tracks} \frac{p_T track}{p_T^\mu}$ has to be smaller than 0.05, where p_T^μ is the muon transverse momentum and the sum is over all tracks (excluding the muon candidate track) that have $p_T > 0.4$ GeV, pass quality cuts and have $\Delta R(track, \mu) < \frac{K_T}{p_T^\mu}$ with $K_T = 10$ GeV.

4.2 Missing Transverse Energy

The presence of a high energy neutrino in the event is linked to a large value of missing energy in the detector. Unfortunately, considering that the initial momentum of the colliding partons along the beam axis is not known, the total missing energy cannot be evaluated. Anyway, with a good approximation the sum of the transverse momentum of the interacting partons

with respect to the beam axis can be considered equal to 0, allowing the determination of the missing transverse energy E_T^{miss}, defined as:

$$E_T^{miss} = \sqrt{(E_x^{miss})^2 + (E_y^{miss})^2}$$

$$E_x^{miss} = -\sum_{i=1}^{N_{cells}} E_i \sin\theta_i \cos\phi_i \qquad E_y^{miss} = -\sum_{i=1}^{N_{cells}} E_i \sin\theta_i \sin\phi_i$$

The E_T^{miss} is evaluated through a *clustering* approach [79], as in the jet reconstruction, using as seeds the calorimeter cells which pass a noise suppression algorithm. All the cells with $|E| > 4\sigma_{noise}$ are selected as origin of the clusters, where there all the neighboring cells with $|E| > 2\sigma_{noise}$ are added. Finally, all the neighboring cells with $|E| > 0$ are added to the cluster.

Then the E_T^{miss} evaluation is done using the contribution from the topological clusters transverse energy corrected for energy losses in the cryostat system and reconstructed muons:

$$E_{x,y}^{miss} = E_{x,y}^{calo} + E_{x,y}^{cryo} + E_{x,y}^{muon}.$$

The cryostat term $E_{x,y}^{cryo}$ considers the non negligible loss of energy in hadronic showers due to the cryostat system installed between the LAr electromagnetic calorimeter and the Tile hadronic calorimeter, and is evaluated through the energy correlation between the last LAr layer and the first Tile one.

The muon term $E_{x,y}^{muon}$ is evaluated from the information on muons extracted from the Inner Detector and Muon spectrometer.

The calorimeter term $E_{x,y}^{calo}$ is evaluated using cells belonging to the topological clusters and included in the pseudorapidity range $|\eta| < 4.9$. The values of $E_{x,y}^{calo}$ are obtained after a refined calibration of every topological cluster to the electromagnetic scale. Every calorimeter cell is associated with a parent high-p_T object which has been reconstructed and identified, in this order: electrons, photons, muons, hadronically decaying taus, b-jets and light jets.

The link between cells and reconstructed objects is done through an association map, which is filled starting from the objects (in the order which has

been mentioned), moving back to their component clusters and to their cells. In order to avoid double counting in the E_T^{miss} calculation, if a cell belongs to more than one kind of objects, only the first association is included in the map; if a cell belongs to more than one object of the same kind, all associations are included in the map, but with geometrical weights which account the shared energy between the topological clusters.

The calibrated $E_{x,y}^{calo}$ is then calculated as follows:

$$E_{x,y}^{calo} = -\left(E_{x,y}^{electrons} + E_{x,y}^{photons} + E_{x,y}^{muons} + E_{x,y}^{taus} + E_{x,y}^{bjets} + E_{x,y}^{jets} + E_{x,y}^{CellOut}\right)$$

where the $E_{x,y}^{CellOut}$ term takes account of the remaining energy from cells which are not associated with a high p_T object.

Not all the missing transverse energy is due to the presence of a neutrino: there are also effects related to the energy resolution (especially in some transition regions between different detectors), the electronical noise of the calorimeter and muon spectrometer, which enlarge the value of the missing energy, and errors in the muon reconstruction, due to fake muons and non-detection in regions where the coverage of the Spectrometer is lower (like $\eta = 0$ and $|\eta| > 2.7$).

The main contribution to the fake missing energy is due to the measurements in the calorimeters, where there are transition regions with lower resolution, in particular for $1.3 < |\eta| < 1.6$ and $3.1 < |\eta| < 3.3$.

The performance and systematic uncertainties of the E_T^{miss} calculation are determined examining the distributions obtained with data and simulations in $Z \to \ell\ell$ and $W \to \ell\nu$ events, like the ones shown in Figure 4.6.

4.3 Event reconstruction and selection

4.3.1 Event Selection

After the reconstruction of all the objects in the events is done, several requests are applied in order to select events originating from the decay of

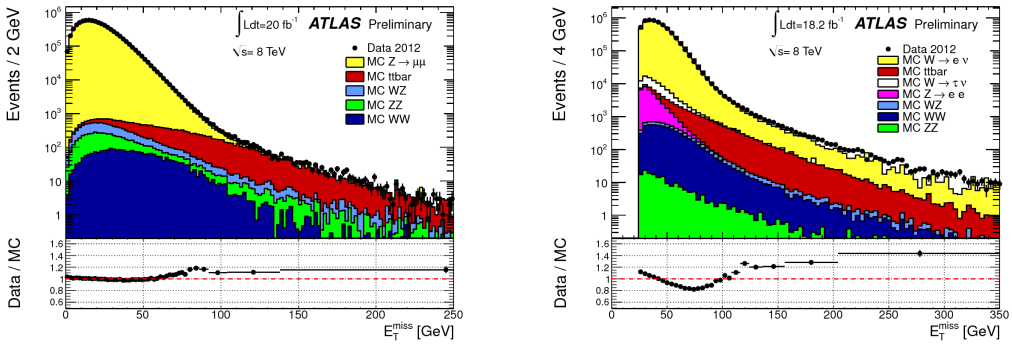

Figure 4.6: The distribution of E_T^{miss} in (left) $Z \to \mu\mu$ events and (right) $W \to e\nu$ events.[93]

a $t\bar{t}$ event, rejecting as much as possible all non-$t\bar{t}$ contributions. The event selection is done as follows:

- Each event must have a reconstructed primary vertex with five or more associated tracks.
- Every event must contain exactly one reconstructed lepton candidate geometrically matched to the trigger object, with at least $p_T > 25$ GeV.
- Every event must have $E_T^{miss} > 20$ GeV due to the presence of the neutrino.
- In order to suppress QCD multijet events, the sum $E_T^{miss} + m_T^W$ must be over 60 GeV, where m_T^W is the transverse mass of the W boson defined as $\sqrt{2p_T^{\ell} E_T^{miss} (1 - \cos\Delta\phi)}$ and $\Delta\phi$ is the azimuthal angle between the lepton and E_T^{miss}.
- Since highly boosted top quark decay products tend to be collimated, each event must have at least one jet ($R = 0.4$) close to the charged lepton ($\Delta R(\ell, j_{R=0.4}) < 1.5$), with at least $p_T > 25$ GeV.
- For the same reason, the decay products of the hadronic top are selected looking for the highest-p_T large-R trimmed jet with $p_T > 300$ GeV,

mass $m_{jet} > 100$ GeV, splitting scale $\sqrt{d_{12}} > 40$ GeV, well separated from the lepton ($\Delta\phi(\ell, j_{R=1}) > 2.3$) and from the jet associated to the lepton ($\Delta R(j_{R=1}, j_{R=0.4}) > 1.5$).

- At least one of the two top candidates must be b-tagged: either the highest p_T jet close to the lepton ($\Delta R(\ell, j_{R=0.4}) < 1.5$) or at least one jet close to the large-R jet ($\Delta R(j_{R=1}, j_{R=0.4}) < 1$) must be b-tagged.

The number of events selected in the el+jets and μ+jets channels will be showed in Section 5.2, as well as some control plots.

4.3.2 Leptonic Top and $t\bar{t}$ system reconstruction

Once the events are selected, the $t\bar{t}$ system can be reconstructed as the sum of the four-vectors of the reconstructed objects composing the two top quarks. The reconstructed hadronically decaying top quark corresponds exactly to the large-R jet with the highest p_T which has been found in the event.

On the other side, the reconstruction of the leptonically decaying top cannot be obtained directly using measured quantities because of the missing information on the longitudinal momentum of the neutrino. The first step is the recontruction of the W boson. While there are no difficulties to reconstruct the charged lepton, the momentum of the neutrino can only be inferred from the reconstructed E_T^{miss}, which defines only the x and y components, but leaves the z component completely unknown. The missing component of the neutrino momentum can be reconstructed, imposing that the W boson is on-shell and using its pole mass $M_W = 80.4$ GeV as a constraint[15].

Indeed, if the neutrino originates from the leptonical decay of the W boson, the sum of the four-vectors $\mathbf{P}_\ell$ and $\mathbf{P}_\nu$ of the charged lepton and the neutrino, respectively, has to be equal to the four-vector $\mathbf{P}_W$ of the W boson:

$$\mathbf{P}_W = \mathbf{P}_\ell + \mathbf{P}_\nu$$

Squaring this equation

$$\mathbf{P}_W^2 = (\mathbf{P}_\ell + \mathbf{P}_\nu)^2 = \mathbf{P}_\ell^2 + \mathbf{P}_\nu^2 + 2\mathbf{P}_\ell \cdot \mathbf{P}_\nu,$$

and neglecting the invariant mass of the neutrino $\mathbf{P}_\nu^2 = M_\nu^2$, it is possible to obtain

$$\begin{aligned} M_W^2 - M_\ell^2 = 2\mathbf{P}_\ell \cdot \mathbf{P}_\nu &= 2\left(E_\ell E_\nu - \overrightarrow{p}_\ell \cdot \overrightarrow{p}_\nu\right) \\ &= 2\left(E_\ell E_\nu - \overrightarrow{p}_{T,\ell} \cdot \overrightarrow{p}_{T,\nu} - p_{z,\ell} p_{z,\nu}\right) \\ &= 2\left(E_\ell E_\nu - p_{T,\ell} E_T^{miss} \cos\Delta\phi - p_{z,\ell} p_{z,\nu}\right), \end{aligned}$$

where $E_T^{miss} = p_{T,\nu}$ for massless neutrinos and $\Delta\phi$ is the azimuthal angle difference between the charged lepton and E_T^{miss}. By introducing the abbreviation $\mu = \frac{M_W^2 - M_\ell^2}{2} + p_{T,\ell} E_T^{miss} \cos\Delta\phi$, the equation can be written as

$$E_\ell E_\nu = \mu + p_{z,\ell} p_{z,\nu}.$$

The energy E_ν of the massless neutrino can be expressed in terms of E_T^{miss} and z component of the momentum.

$$E_\ell \sqrt{E_T^{miss\,2} + p_{z,\nu}^2} = \mu + p_{z,\ell} p_{z,\nu}.$$

Squaring the equation it is possible to obtain a quadratic equation in $p_{z,\nu}$:

$$p_{z,\nu}^2 - 2\frac{\mu p_{z,\ell}}{E_\ell^2 - p_{z,\ell}^2} p_{z,\nu} + \frac{E_\ell^2 E_T^{miss\,2} - \mu^2}{E_\ell^2 - p_{z,\ell}^2} = 0$$

and the solution will be

$$p_{z,\nu}^{\pm} = \frac{\mu p_{z,\ell}}{E_\ell^2 - p_{z,\ell}^2} \pm \frac{\sqrt{\Delta}}{2}$$

where Δ is the discriminant $\Delta = 4\frac{\mu^2 p_{z,\ell}^2}{E_\ell^4 - p_{z,\ell}^4} - 4\frac{E_\ell^2 E_T^{miss\,2} - \mu^2}{E_\ell^2 - p_{z,\ell}^2}$.

In case $\Delta \geq 0$, the chosen solution for $p_{z,\nu}$ is the one with the smallest absolute value of the possible two, while in case $\Delta < 0$ only the real part of the solution will be considered as the z component of the neutrino momentum.

Once $p_{z,\nu}$ is calculated, it is possible to reconstruct the four-momentum of the leptonic W boson, as the sum of the four-momenta of the charged lepton

and the neutrino. After that, the leptonic top quark can be reconstructed composing the W boson with the candidate b-jet of the process $t \to Wb$, which is selected as the jet with the highest p_T among the ones close to the charged lepton within a region $\Delta R(\ell, j) < 1.5$. Once the hadronic and leptonic top quarks are reconstructed, the $t\bar{t}$ system is reconstructed by simply summing their four-momenta.

4.4 Background estimation

Several background processes contribute to the real data selected events and must be evaluated before the cross section measurements. The most important background sources which must be taken into account are

- The W boson production in association with multiple jets (W+jets).
- $t\bar{t}$ production in the dilepton channel, considered here as a background process.
- Single top production.
- QCD Multijet production.
- Diboson: production of couple of bosons (WW, WZ, ZZ).
- The Z boson production in association with multiple jets (Z+jets).

The W+jets, $t\bar{t}$ dilepton, single top, Z+jets and diboson processes are estimated with Monte Carlo simulations, taking into account the expected production cross sections of each process, as listed in Table 4.1.

The overall normalization for the W+jets processes and the QCD multijet background in its entirety, which are the most significant background contributions, are described with data driven methods since their prediction is affected by a quite large uncertainty.

The contamination of all these background sources in the event selection will be showed in Section 5.2.

Process	8 TeV Cross Section (pb)
$t\bar{t}$ Not fully hadronic channel	137.32
Single top Leptonic t-channel Leptonic s-channel Inclusive Wt-channel	~ 53
W+jets $W \to \ell\nu$+jets	$\sim 3.86 \cdot 10^4$
Z+jets $Z \to \ell^+\ell^-$+jets	$\sim 3.58 \cdot 10^3$
Diboson+jets $(ZW \to \ell\ell qq)$+light and heavy jets $(ZZ \to \ell\ell qq)$+light and heavy jets $(WW \to \ell\nu qq)$+light and heavy jets	~ 34
QCD Multijet	$\sim 7.18 \cdot 10^{10}$

Table 4.1: Production cross sections for signal and background sources.

4.4.1 QCD Multijet estimation

QCD Multijet events can be confused with the signal if one jet is misidentified as a charged lepton and uncertainties in the calculations of energy balance lead to an apparent E_T^{miss} in the event. In particular, it is possible to identify as *fake leptons* long living mesons (like $\pi^{\pm}$ or $K^{\pm}$), photons and hadronic jets. Even if this misidentification has a very small rate, the huge multijet cross section makes its contribution not negligible.

In order to make predictions of the QCD multijet backgrounds the so-called "Matrix Method" (developed by the Tevatron experiments [94]) is used, determining the efficiency between signal-like and fake-like events selected with different lepton requirements.

The matrix method divides a sample into two categories, based on the

definition of electron used in the analysis, *loose* and *tight*. So it is possible to write

$$N^{loose} = N^{loose}_{real} + N^{loose}_{fake}$$
$$N^{tight} = N^{tight}_{real} + N^{tight}_{fake}$$

where there is the decomposition of the number of events in the samples into events with real leptons and with fake leptons. The number of events passing the tight selection can be further decomposed as

$$N^{tight} = \epsilon_{real} N^{loose}_{real} + \epsilon_{fake} N^{loose}_{fake}$$

where $\epsilon_{real} = \frac{N^{tight}_{real}}{N^{loose}_{real}}$ and $\epsilon_{fake} = \frac{N^{tight}_{fake}}{N^{loose}_{fake}}$ are the efficiencies for real and fake leptons in the loose sample to pass the tight criteria.

If it is possible to measure these two efficiencies indipendently, there are two equations for two unknowns (the number of real and fake events in the tight sample). The solution is

$$N^{tight}_{fake} = \frac{\epsilon_{fake}}{\epsilon_{real} - \epsilon_{fake}} \cdot \left(N^{loose} \epsilon_{real} - N^{tight} \right).$$

If the two efficiencies are significantly different this equation will provide a good estimation of the fake fraction of events in the tight selection.

The efficiency of real leptons is obtained from a $Z \to \ell\ell$ events, on which the same selection of the analysis is applied, with the exception of the jet-related requirements.

The fake efficiency is estimated from a $t\bar{t}$ sample, which is enhanced in fake leptons by *loosening* the lepton identification requirements. The efficiency is obtained making the ratio between events in the selected *loose* lepton which also pass the *tight* requirements, divided by the total number of the *loose* events.

4.4.2 Estimation of W+jets background

The estimation of the W+jets background has been performed using a combination of Monte Carlo simulations and data driven corrections[95],

since there is not a clear theoretical description of the overall normalization and of the heavy flavor contribution.

W+jets normalisation

The estimation of the overall normalization of the W+jets background is done exploiting the charge asymmetry in the production of W bosons. In LHC the difference between the parton distribution functions for quarks and antiquarks leads to an overall charge asymmetry in the W boson production, which reflects on a charge asymmetry of the leptons from the W decay. Even if the normalization is not well theoretically described, it is possible to determine it from the ratio of W^+ to W^- in order to have a normalization constraint.

The signal and other background contributions can be considered charge symmetric, so it can be written:

$$N_{W^+} + N_{W^-} = \left(\frac{r_{MC}+1}{r_{MC}-1}\right)\left(D^+ - D^-\right),$$

where D^+ and D^- are the number of events with positively and negatively charged leptons and $r_{MC} = \frac{\sigma(pp\to W^+)}{\sigma(pp\to W^-)}$. This value has been measured as a function of the jet multiplicity.

Since the signal sample has too few events to be used to derive the overall W+jets normalization, a sample enhanced in W+jets events has been obtained by dropping the b-tagging, $\Delta\phi(j_{R=1}, \ell)$, large-$R$ jet mass and $\sqrt{d_{12}}$ requirements.

W+heavy flavor normalization

The number of tagged jets in the ith jet multiplicity bin can be written as

$$N^{tag}_{i\text{-}jet} = N^{pre\text{-}tag}_{i\text{-}jet}(F_{b\bar{b},i}P_{b\bar{b}} + F_{c\bar{c},i}P_{c\bar{c}} + F_{cl,i}P_{cl} + F_{ll,i}P_{ll})$$

where N^{tag}_{i-jet} is the number of tagged jets in the ith jet multiplicity bin, $F_{xx,i}$ is the real fraction of events which have b, c or light jet composition and P_{xx} is the probability to tag an event with xx flavor composition.

Two main constraining conditions have to be considered. First of all, the flavor fractions must sum up to to 1; secondly, the number of W+jet events in the ith bin has to be the number in data after subtracting the non-W component. These two conditions can be translated as follows

$$F_{b\bar{b},i} + F_{c\bar{c},i} + F_{cl,i} + F_{ll,i} = 1,$$

$$N_{i\text{-}jet} = N_{i\text{-}jet}^{data} - N_{i\text{-}jet}^{MC,non\text{-}W}.$$

Introducing the correction $F_{cc} = k_{b\bar{b}\to c\bar{c}} F_{b\bar{b}}$ and likewise for cl ad ll, the 2 jet bin becomes, for example

$$\begin{aligned} N_{i\text{-}jet}^{tag} = N_{i\text{-}jet}^{pre\text{-}tag} (& k_{b\bar{b}2jet\to i\text{-}jet} F_{b\bar{b},i} P_{b\bar{b}} + k_{cc2jet\to i\text{-}jet} F_{c\bar{c},i} P_{c\bar{c}} \\ & + k_{cl2jet\to i\text{-}jet} F_{cl,i} P_{cl} + k_{ll2jet\to i\text{-}jet} F_{ll,i} P_{ll}) \end{aligned}$$

where some Monte Carlo factors are introduced, describing the number of xx flavor events in the 2 jet bin that migrate to the ith bin.

If it is possible to measure the tagged jet probabilities, there are still four unknowns, corresponding to the heavy flavor fractions, which can be extracted for any jet multiplicity using four independent constraining equations.

The 2 jet multiplicity bin is dominated by W+jet production, so it is used to extract a set of k-factors between the measurements and Monte Carlo predictions. After that, because these scale factors are not the same in all jet multiplicity bins, they are renormalized to unity on a jet bin multiplicity basis.

These estimations have been done in a $t\bar{t}$ sample with the same lepton and E_T^{miss} selections as the signal selection, but with two small-R jets and no b-tagging cuts.

Chapter 5

Boosted $t\bar{t}$ Differential Cross Section Measurement

In this chapter the techniques used to measure the $t\bar{t}$ differential production cross section are presented, as well as the unfolding procedures used to remove the smearing effects due to the detector and the analysis. A detailed description of how the statistical and systematic uncertainties have been treated is also presented. Finally, the results obtained in the e+jets channel, μ+jets channel and in the combined channel are shown and commented.

5.1 Measurement strategy

As outlined in the previous chapters, the measurement of the boosted $t\bar{t}$ differential cross section is done by selecting a sample enriched in lepton+jets $t\bar{t}$ events ($\sim 85\%$) requiring the following prescriptions:

- The hadronically decaying top quark is reconstructed using an $R = 1.0$ jet, which is reconstructed with the anti-kt algorithm and trimmed in order to reduce the effects coming from initial state radiation, underlying event activity, and pile-up. To discard jets coming from QCD radiation, other cuts on the substructure of the large-R jets are applied, investigating their mass and the p_T of the subjects.

- The hadronically decaying and the leptonically decaying top quarks are required to have a certain a spatial separation, because they are produced mainly back-to-back. The leptonically decaying top is reconstructed looking for a lepton (electron or muon), a close $R = 0.4$ anti-kt jet and a significant value of missing transverse energy, which is used to reconstruct the transverse momentum of the neutrino. The longitudinal component of the neutrino momentum is then extrapolated using the W boson pole mass $M_W = 80.4$ GeV as a constraint, imposing that it is on-shell.

- Once the events are selected and the $t\bar{t}$ system is reconstructed making the vectorial sum of the two top quarks's four-momenta, there is still some background contamination, composed mainly, in order of importance, of W+jets, $t\bar{t}$ dilepton, single-top, and QCD multijets events. Their effect is estimated with a Monte Carlo simulation, except for W+jets normalization and the QCD multijets events, which are extracted using data-driven techniques.

The measurement of the cross section as a function of different kinematical variables of the $t\bar{t}$ system is performed using the unfolded distributions of these variables, where the detector inefficiencies and the smearing effects are corrected. These measurements are obtained both at *particle level* in a fiducial region which follows closely the event selection at detector-level, and at *parton level* in the full phase space of $t\bar{t}$ events.The unfolded *particle level* and *parton level* differential cross sections are eventually compared to the predictions of different Monte Carlo generators. The methods used to perform the measurement of the differential cross section are described in detail in the following sections.

5.2 Control plots

The selection criteria listed in the previous chapter lead to the event yields on data and MC samples which are listed in Table 5.1.

Sample	e+jets	μ+jets
$t\bar{t}$ ℓ+jets	4008	3496
$t\bar{t}$ dilepton	223	210
W+jets	234	226
Single top	129	130
QCD multijet	91	3
Z+jets	34	14
Diboson	22	18
Prediction	4743	4101
Data	4145	3603

Table 5.1: Observed and expected number of events in e+jets and μ+jets channel.

To verify whether the measurements are well described by the Monte Carlo simulation and whether the analysis is done correctly it is useful to check the distribution of some of the involved variables. Control plots have been produced separately for the electron channel and for the muon channel and are shown from Figure 5.1 to Figure 5.8. In the plots, the distribution obtained using real data are represented by the black points, while the Monte Carlo simulation corresponds to a series of coloured histograms: the $t\bar{t}$ signal (ℓ+jets channel) is white, while the the dileptonic top events are green, the single top events are blue, the background processes due to electroweak interactions are yellow. Finally, the systematic uncertainties are represented by the hatched band.

In Figure 5.1 and 5.2 it is possible to see the distribution of the reconstructed lepton p_T, the missing transverse energy E_T^{miss}, the leptonic W mass and the b-tagged jet p_T, in both electron and muon channel. As can be seen, the data distribution is well described by the Monte Carlo simulation.

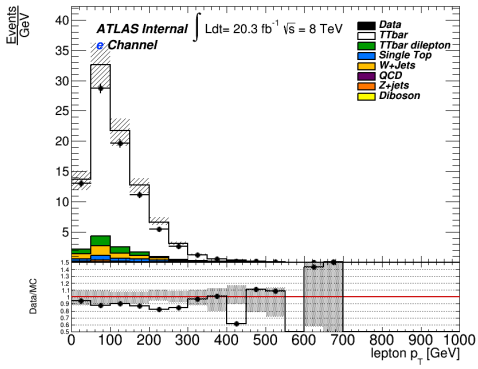

(a) Electron p_T

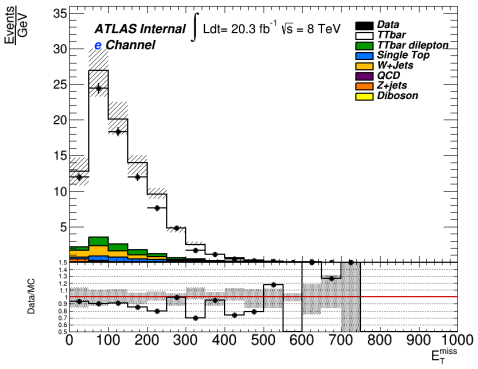

(b) Missing Transverse Energy

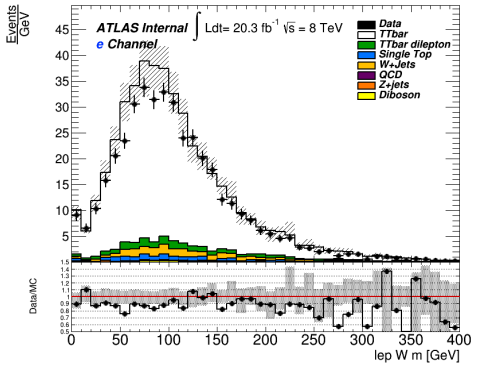

(c) Leptonic W mass

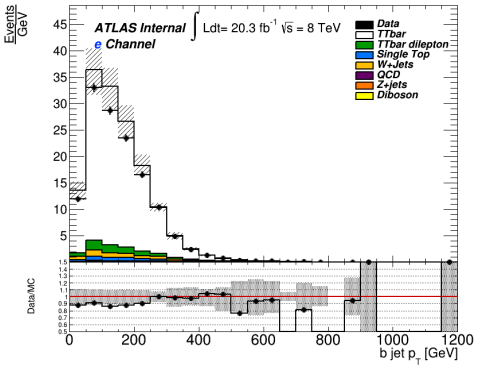

(d) b-jet p_T

Figure 5.1: The (a) lepton p_T, (b) Missing Transverse Energy, (c) leptonic W mass and (c) b-jet p_T in the electron channel. The distribution obtained from the real data is represented by the black points, the white histograms represent the simulation of the $t\bar{t}$ lepton+jets signal, while colored hisograms correspond to the estimated background contamination and the hatched band represent the systematic uncertainties.

Combining different reconstructed objects, it has been possible to define the boosted hadronically decaying top, as a large-R jet with $p_T > 300$ GeV, distributions in mass, transverse momentum and pseudorapidity are shown in Figure 5.3 and 5.4. For these distributions, also the QCD multijet background has been considered and its contribution is shown in purple. As

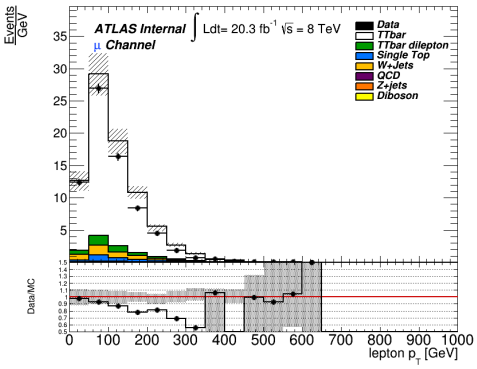

(a) Muon p_T

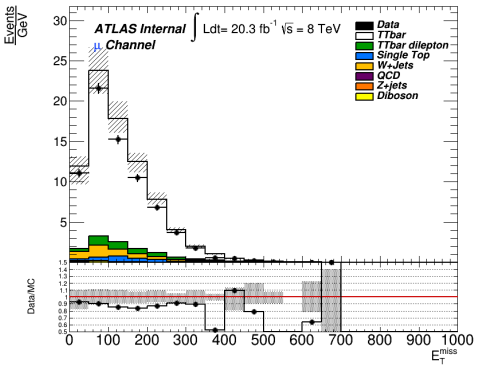

(b) Missing Transverse Energy

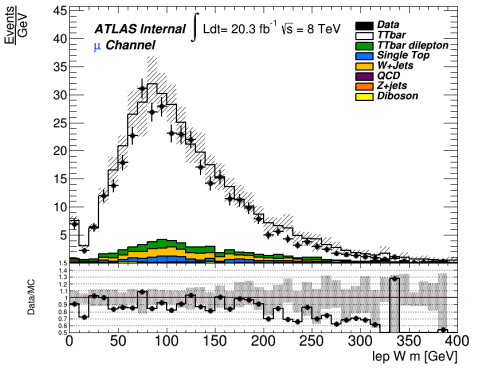

(c) Leptonic W mass

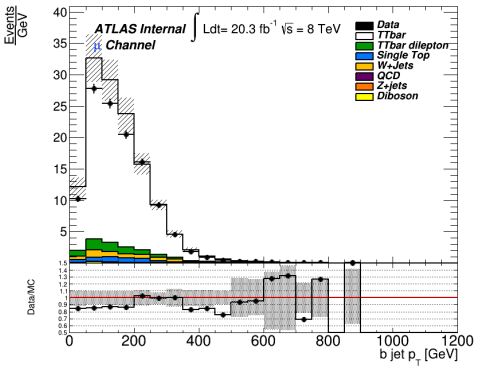

(d) b-jet p_T

Figure 5.2: The (a) lepton p_T, (b) Missing Transverse Energy, (c) leptonic W mass and (c) b-jet p_T in the muon channel. The distribution obtained from the real data is represented by the black points, the white histograms represent the simulation of the $t\bar{t}$ lepton+jets signal, while colored hisograms correspond to the estimated background contamination and the hatched band represents the systematic uncertainties.

can be seen in the Figures, the reconstructed boosted hadronic top is well described by the Monte Carlo simulation.

With the reconstructed leptons, jets and missing transverse energy used to select the signal, it has been possible to reconstruct the leptonically decaying top, whose distributions in mass, p_T and η are shown in Figure 5.5 and 5.6.

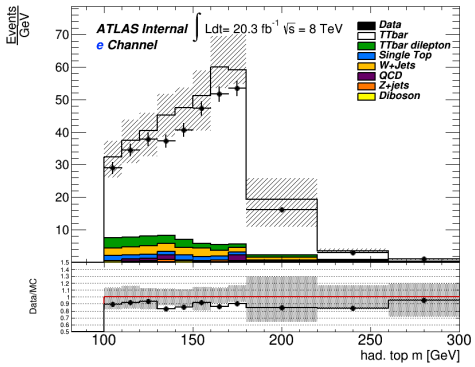

(a) Hadronic Top candidate Mass

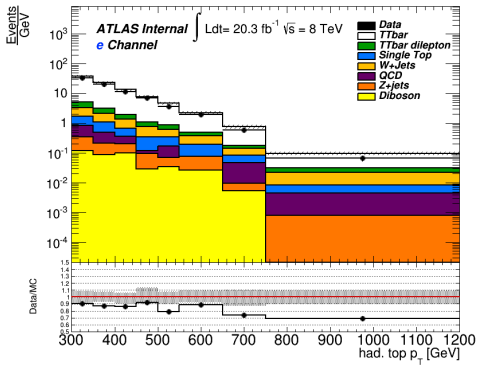

(b) Hadronic Top candidate p_T

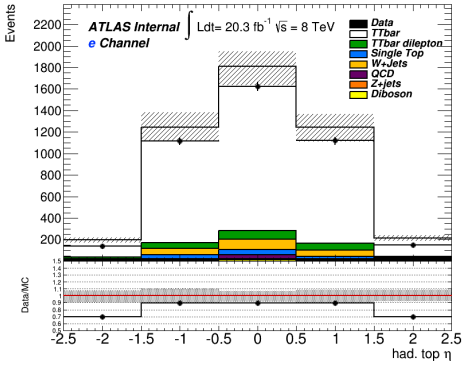

(c) Hadronic Top candidate η

Figure 5.3: The (a) mass, (b) p_T and (c) η of the hadronic top in the electron channel. The distribution obtained from the real data is represented by the black points, the white histograms represent the simulation of the $t\bar{t}$ lepton+jets signal, while colored hisograms correspond to the estimated background contamination and the hatched band represents the systematic uncertainties.

Unlike on the hadronic top, no selection criteria has been applied on the p_T of the leptonic top, which is expected to be similar. Because of that, the binning on the transverse momentum plot is different from the one made for the hadronic top, starting from $p_T = 200$ GeV, in order not to loose events and to evaluate the statistics in those bins, which appears to be low.

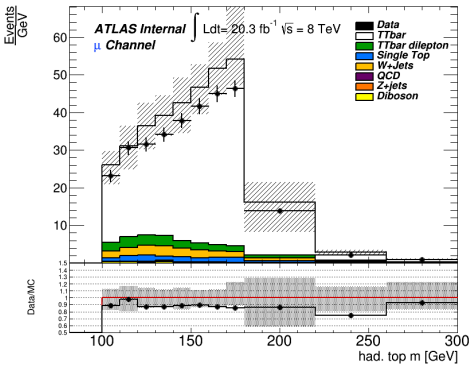

(a) Hadronic Top candidate Mass

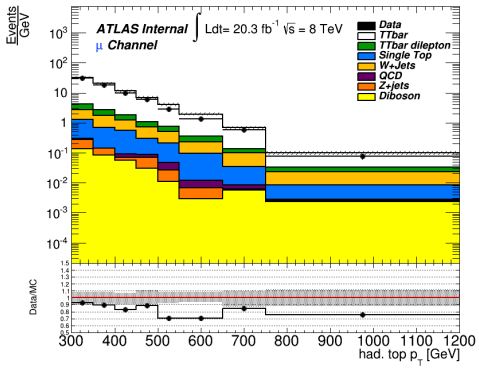

(b) Hadronic Top candidate p_T

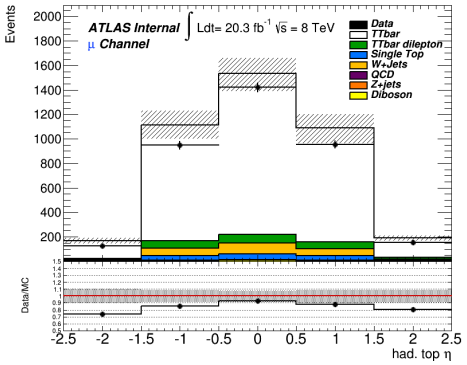

(c) Hadronic Top candidate η

Figure 5.4: The (a) mass, (b) p_T and (c) η of the hadronic top in the muon channel. The distribution obtained from the real data is represented by the black points, the white histograms represent the simulation of the $t\bar{t}$ lepton+jets signal, while colored hisograms correspond to the estimated background contamination and the hatched band represents the systematic uncertainties.

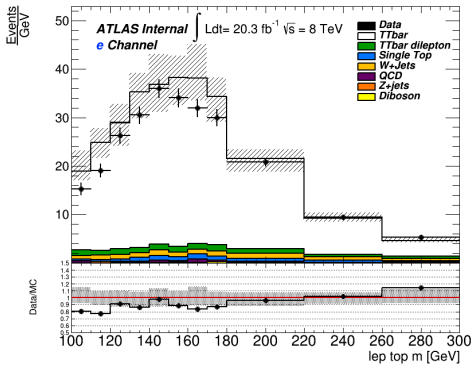

(a) Leptonic Top candidate Mass

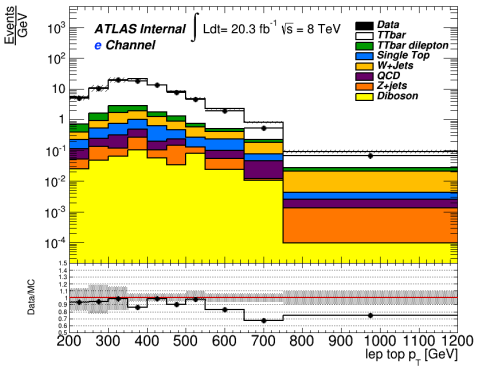

(b) Leptonic Top candidate p_T

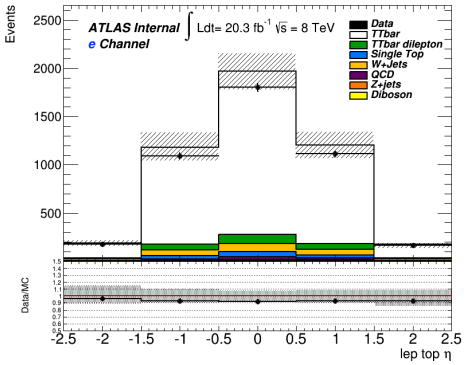

(c) Leptonic Top candidate η

Figure 5.5: The (a) mass, (b) p_T and (c) η of the leptonic top in the electron channel. The distribution obtained from the real data is represented by the black points, the white histograms represent the simulation of the $t\bar{t}$ lepton+jets signal, while colored hisograms correspond to the estimated background contamination and the hatched band represents the systematic uncertainties.

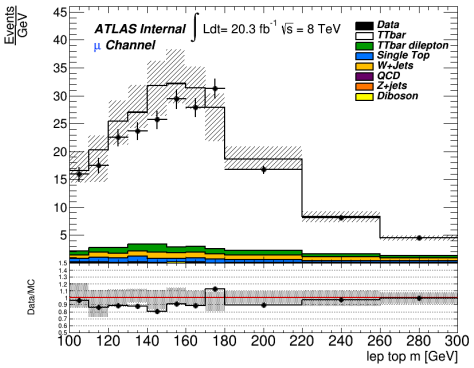

(a) Leptonic Top candidate Mass

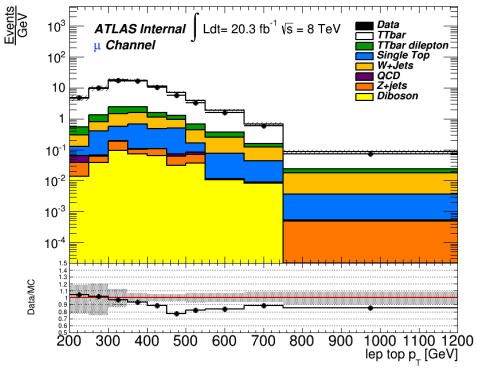

(b) Leptonic Top candidate p_T

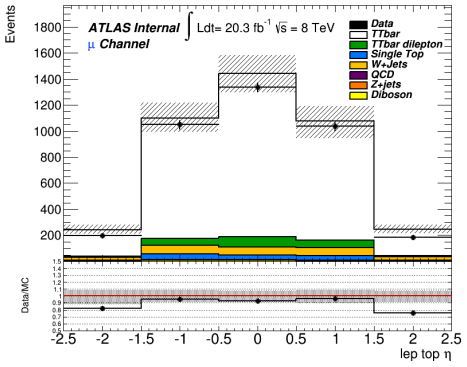

(c) Leptonic Top candidate η

Figure 5.6: The (a) mass, (b) p_T and (c) η of the leptonic top in the muon channel. The distribution obtained from the real data is represented by the black points, the white histograms represent the simulation of the $t\bar{t}$ lepton+jets signal, while colored hisograms correspond to the estimated background contamination and the hatched band represents the systematic uncertainties.

Also in this case, it can be seen that the leptonic top distributions are well described by the Monte Carlo simulation. Hence, it is possible to reconstruct the $t\bar{t}$ system. The mass, p_T and η spectra of the $t\bar{t}$ system in electron and muon channel are shown in Figure 5.7 for the electron channel and Figure 5.8 for the muon channel.

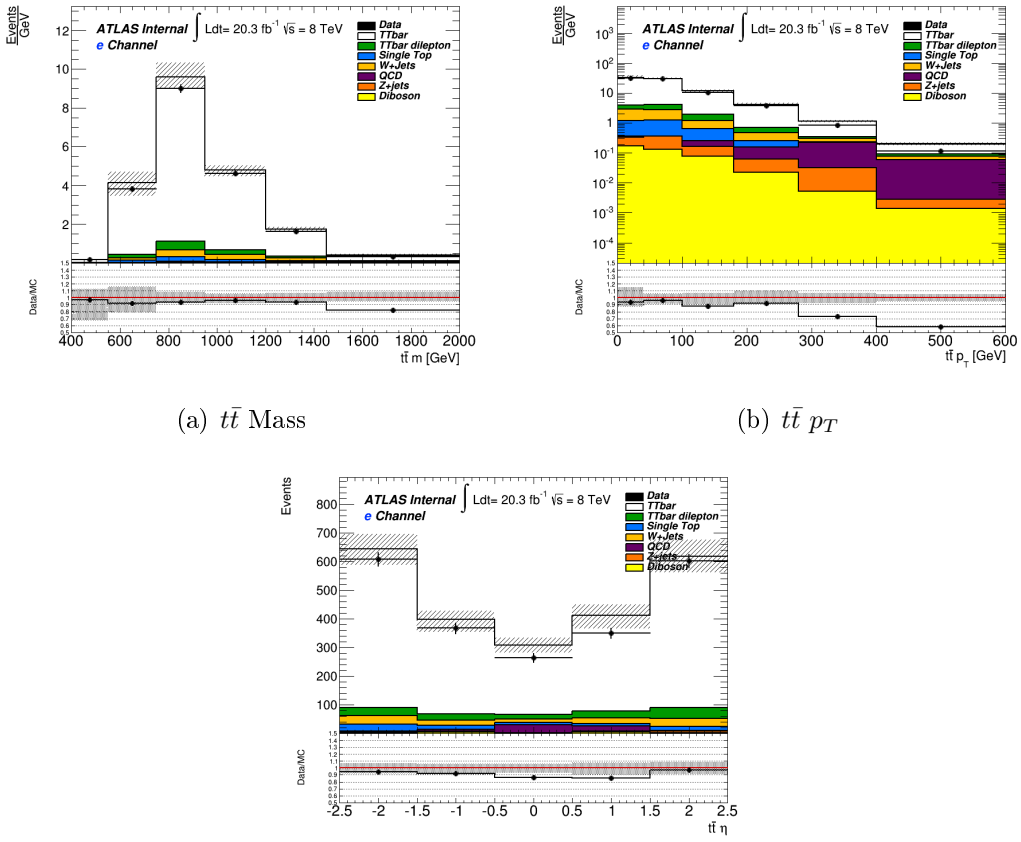

(a) $t\bar{t}$ Mass

(b) $t\bar{t}$ p_T

(c) $t\bar{t}$ η

Figure 5.7: The (a) mass, (b) p_T and (c) η of the $t\bar{t}$ system in the electron channel. The distribution obtained from the real data is represented by the black points, the white histograms represent the simulation of the $t\bar{t}$ lepton+jets signal, while colored hisograms correspond to the estimated background contamination and the hatched band represents the systematic uncertainties.

The reconstructed $t\bar{t}$ is well described by the Monte Carlo simulation, both in the electronic channel and muonic channel. Hence, the Monte Carlo

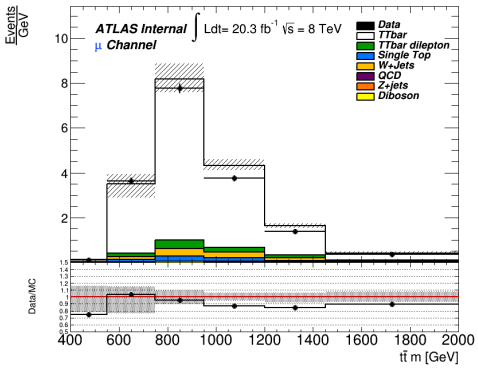

(a) $t\bar{t}$ Mass

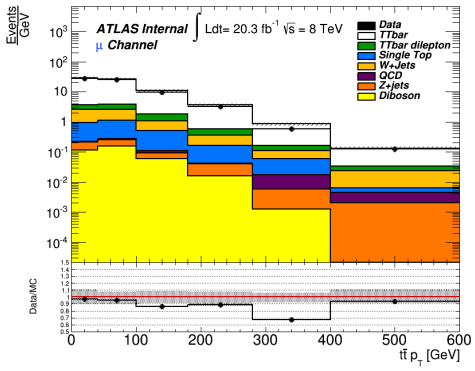

(b) $t\bar{t}$ p_T

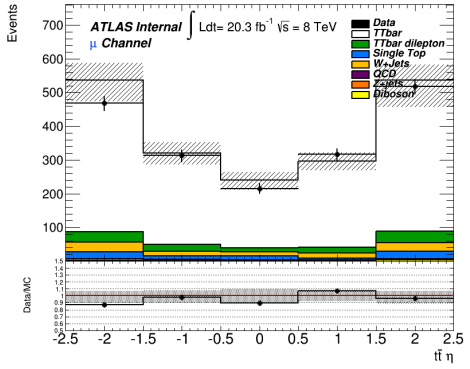

(c) $t\bar{t}$ η

Figure 5.8: The (a) mass, (b) p_T and (c) η of the $t\bar{t}$ system in the muon channel. The distribution obtained from the real data is represented by the black points, the white histograms represent the simulation of the $t\bar{t}$ lepton+jets signal, while colored hisograms correspond to the estimated background contamination and the hatched band represents the systematic uncertainties.

distribution can be used to subtract the background effect from the distributions and to unfold them, in order to extract the right values of the $t\bar{t}$ differential cross section.

5.3 Unfolding

The limited experimental resolution and geometric acceptance of the detectors produce a distortion in the measurement of the spectra of physical observables. Indeed, a direct comparison between the reconstructed distributions of physical variables and their theoretical predictions is not possible, as well as a comparison between the results of different experiments. In order to do so, measurements must be corrected for these detector effects before any comparison, with a procedure which is called *unfolding*.

The unfolding provides the distribution $f(x)$ of a certain physical variable x, starting from the measurement y and its distribution $g(y)$, distorted both by detector effects and the analysis method. In particular the detector affects the measurements with its limited acceptance, its limited resolution of the observed variables, and mis-identification of reconstructed objects.

The limited acceptance means that the variable cannot always be measured, because of the geometrical acceptance or trigger efficiency or the selection efficiency. All these factors contribute to a total efficiency ϵ.

On the contrary, the limited resolution means that it is impossible to measure the variable x with an infinite accuracy and so the measured value y can be different with respect to the true one x, leading to a distribution $g(y)$ which is a convolution of the true $f(x)$ with the resolution function.

The folding integral establishes a link between the true and measured variables [96]:

$$g(y) = \int_a^b A(y,x) f(x) dx$$

where a and b are the interval where x is defined and $A(y,x)$ is the resolution function. The integral is needed, since $g(y)$ and y are smeared by a limited resolution in the measurements of x and every measurement y has contributions from a series of true x. The function $A(y,x)$ is usually estimated through Monte Carlo simulations which allow to study the detector effects on a known distribution $f(x)$, determining the relation between $g(y)$ and $f(x)$.

Hence the unfolding procedures are techniques that allow to solve the inverse problem with respect to the folding integral shown above. In case of discrete variables x and y, the problem and hence the solution is easier. In this case, the $f(x)$ and $g(y)$ are simple histograms and the unfolding equation becomes

$$\mathbf{g} = R\mathbf{f},$$

where $\mathbf{f}$ is a n-dimensional vector, $\mathbf{g}$ is a m-dimensional vector, and R is a $m \times n$ matrix called *response matrix*.

Some events generated in bin j can be reconstructed in bin $i \neq j$ with a phenomenon called migration, so the R matrix is not diagonal. The probability that an event generated in bin j is reconstructed in bin i can be expressed by another matrix, the *migration matrix*, which is obtained normalizing the response matrix by the acceptance of the detector.

$$M_{ij} = \frac{1}{A_j} R_{ij}$$

where A_j is the acceptance of the jth bin. Since, once the acceptance is accounted for, a generated event has to be reconstructed somewhere, the elements in the columns are normalized to unity.

In the ideal case with perfect resolution and no mis-reconstructed objects, no migrations between the bins are observed, M_{ij} is diagonal and its elements represent the reconstruction efficiency of the x variable in the jth bin, which can be evaluated through Monte Carlo simulations. The reconstruction of the variable x, generated with the known distribution $\bar{f}$ through Monte Carlo simulations, gives the distribution $\bar{g}$: the reconstruction efficiency results $\epsilon_j = \frac{\bar{g}_j}{\bar{f}_j}$ and so the true population of the j-th bin is

$$f_j = \frac{g_j}{\epsilon_j} = g_j \cdot \left(\frac{\bar{f}_j}{\bar{g}_j} \right)$$

In the real case where migrations are present, the M matrix is not diagonal, and so also the M_{ij} bins with $i \neq j$ have to be considered. The simplest way to solve the unfolding problem is to perform a *matrix inversion*

$$\mathbf{f} = M^{-1}\mathbf{g},$$

where M^{-1} is the inverse matrix of M. This approach to solve the unfolding problem is conceptually the simplest one, but it has some disadvantages, mainly related to the stability of the solutions. Indeed, the solution can oscillate because of the measurement uncertainties, since small deviations from the input distribution could lead to large differences in the output unfolded results.

In order to avoid these kind of oscillating results, other unfolding procedures have been developed, like the Singular Value Decomposition (SVD), which handle the instability of the solutions through some regularization techniques.

5.3.1 Singular Value Decomposition

The Singular Value Decomposition[97], is a regularized extension of the simple matrix inversion, where direct solutions can lead to rapidly oscillating solution. This unfolding method consists in a decomposition of the migration matrix M, obtaining regularised solutions by adding a normalisation term. Indeed, the matrix M ($m \times n$, where $m \geq n$) can be written as

$$M = USV^T$$

where U is an $m \times m$ orthogonal matrix, V is an $n \times n$ orthogonal matrix and S is an $m \times n$ diagonal matrix, whose elements are null or positive. These three matrices have the following properties:

$$U^T U = UU^T = 1$$

$$V^T V = VV^T = 1$$

$$S_{ij} = \lambda_i \delta_{ij}, \quad \lambda_i \geq 0$$

So the inverted migration matrix is

$$M^{-1} = (USV^T)^{-1} = (V^T)^{-1} S^{-1} U^{-1} = VS^{-1}U^T.$$

In this way the inversion process is simplified, and the problem is to find the right matrices to decompose M.

In order to reduce the highly oscillating distributions which can be obtained with a simple matrix inversion, a Tichonov regularization [98] can be done by adding a regularization term:

$$(M\mathbf{f} - \mathbf{g})^T(M\mathbf{f} - \mathbf{g}) + \tau \times (C\mathbf{f})^T C\mathbf{f}$$

where τ is the regularization parameter that weights the initial condition imposed on the solution expressed by the matrix C, which is usually chosen using the theoretical distributions obtained from MC simulation.

Also the solution of the new equation system can be calculated using the SVD inversion procedure and rotating vectors and matrices in a different phase space:

$$USV^T = MC^{-1}, \qquad \mathbf{d} = U^T\mathbf{g}, \qquad \mathbf{z} = V^T C\mathbf{f}.$$

The vectors $\mathbf{d}$ and $\mathbf{z}$ can be expanded in Fourier series, and if the initial distributions are reasonably smooth only the first few terms will be significant and the expansions can be truncated. The number of terms which are considered in the expansion is expressed by the *k factor*, which is a free parameter in the SVD method. This parameter is linked to the regularization parameter τ by the equation

$$\tau = \left[\frac{\mathbf{d}_k}{\mathbf{z}_k}\right]^2.$$

The value of the *k factor* has to be set depending on the boundary conditions. A small value of the *k factor* leads to a strong regularization, also linked to a loss of information and more importance to the a priori knowledge on the distribution, while a higher value allows more oscillating terms in the solution. Typically the chosen value is $k \leq \frac{n}{2}$, where n is the number of bins of the distribution histogram.

5.4 Particle and Parton Level fiducial regions

A differential distribution measured at *detector level* can be corrected at *particle level* or *parton level*, depending on how the "true" particles are defined.

- The *particle level* is defined using stable particles from simulated $t\bar{t}$ events, with a mean lifetime greater than $0.3 \cdot 10^{-10}$ seconds, coming from the hard-scattering pp interaction or from subsequent decays of particles with a shorter lifetime. The simulated $t\bar{t}$ sample used to determine the *particle level* correction is limited to the lepton+jets channel, in which exactly one of the W bosons from the decay of the $t\bar{t}$ pair decays to an electron or a muon either directly or through a τ lepton decay.

  All leptons which are not from hadron decays are considered as prompt isolated leptons, including the ones coming from τ decays, if the parent τ is not a hadron decay product itself. The leptons are *dressed*, adding to their four-momenta the ones of the photons within a cone of $\Delta R \leq 0.1$ around their direction. All stable particles except the selected dressed leptons are used to reconstruct the jets, which are subjected to the same trimming procedure of the *detector level* jets. The b tagging is performed asking whether among the constituents of a jet there is an hadron which contains b quark and has a transverse momentm greater than 5 GeV. The missing transverse energy E_T^{miss} is calculated summing the momenta of neutrinos not resulting from hadron decays.

  The *particle level* fiducial region is chosen to follow closely the *detector level* event selection, including all the requirements on the kinematics of objects and topology of events, with the only exception of the lepton-jet overlap removal procedure and the lepton isolation requirement, which are not applied.

- The *parton level* is defined considering the top quarks before their decay

and after the QCD radiation.The simulated $t\bar{t}$ sample used to determine the *parton level* correction is limited to the lepton+jets channel, in which exactly one of the W bosons from the decay of the $t\bar{t}$ pair decays to an electron or a muon or a τ lepton, including hadronic τ decays.

The *parton level* correction is defined in the full phase-space, taking into account the branching ratio of $t\bar{t}$ pairs to the lepton+jets channel.

5.5 Calculation of differential cross section

Once the distribution of a certain variable X_{reco} reconstructed at *detector level* is obtained, it is possible to extract the differential cross section with respect to that variable, through the unfolding procedure. The differential cross section corrected at *particle level* can be calculated as:

$$\frac{d\sigma}{dX_{particle}}(X^i_{particle}) = \frac{N^i_{particle}}{\Delta X^i_{particle}\mathcal{L}}$$

$$= \frac{1}{\Delta X^i_{particle}\mathcal{L}f^i_{eff.}} \cdot \sum_j M^{-1}_{ij} f^j_{acc.} f_{t\bar{t},\ell+jets} \left(N^j_{reco} - N^j_{reco,bkg}\right)$$

where N^j_{reco} is the number of observed events in bin j of X_{reco} with the *detector level* selection applied, $N^i_{particle}$ is the total number of events in bin i of $X_{particle}$ that meet the fiducial region selection, $\Delta X^i_{particle}$ is the size of bin i of $X_{particle}$ and $\mathcal{L}$ is the integrated luminosity of the data sample.

The contamination $N^j_{reco,bkg}$ coming from the background processes is subtracted from the number of reconstructed events in each bin of the X_{reco} variable. Each bin is then corrected by the multiplicative factor $f_{t\bar{t},\ell+jets}$, which is the fraction of ℓ+jets events in the Monte Carlo $t\bar{t}$ sample, in order to take into account the possible contributions from events which are not semileptonic.

The distribution of the variable X_{reco} reconstructed at *detector level* is then corrected by the acceptance, using the factor $f^j_{acc.}$, which takes account of the $t\bar{t}$ events that pass the *detector level* selection but fail the *particle level*

selection. In particular, $f^j_{acc.}$ is defined as the ratio between the number of events in the bin j of X_{reco} that pass the selection criteria both at *detector level* and *particle level* and the ones that pass the *detector level* selection.

After the acceptance correction, the distribution is corrected for the detector resolution effect through the inversion of the migration matrix M_{ij} that correlate the X_{reco} binned distribution to the $X_{particle}$ distribution. In Figure 5.9 it is possible to see the migration matrices at *particle level* for $m_{t\bar{t}}$, $p_{T,t\bar{t}}$ and $\eta_{t\bar{t}}$ obtained in the electron channel, while in Figure 5.10 there are the ones obtained in the muon channel.

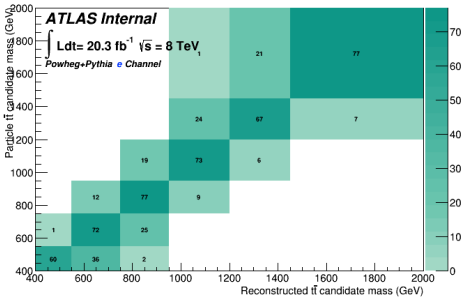

(a) $m_{t\bar{t}}$

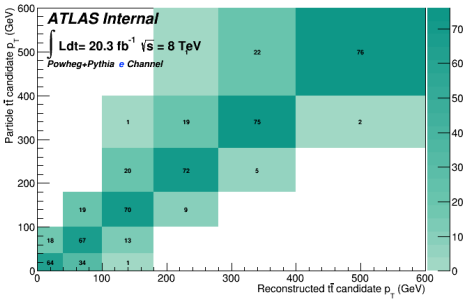

(b) $p_{T,t\bar{t}}$

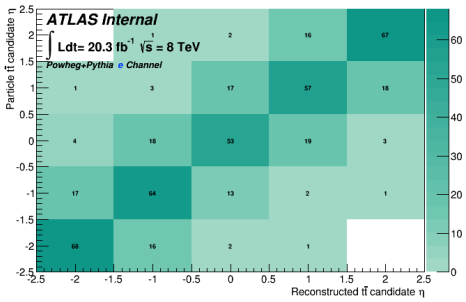

(c) $\eta_{t\bar{t}}$

Figure 5.9: Migration matrices at *particle level* for $m_{t\bar{t}}$, $p_{T,t\bar{t}}$ and $\eta_{t\bar{t}}$ in electron channel

These migration matrices are generally diagonal, with few terms greater then 0 outside the diagonal, proving a good reconstruction of all the variables. η represents the only exception, because at low p_T its measurement is

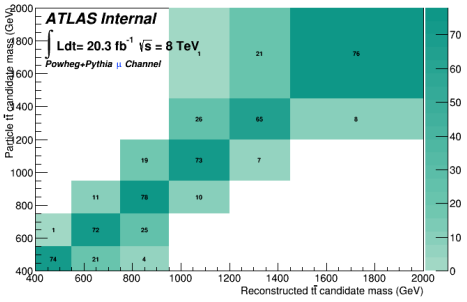

(a) $m_{t\bar{t}}$

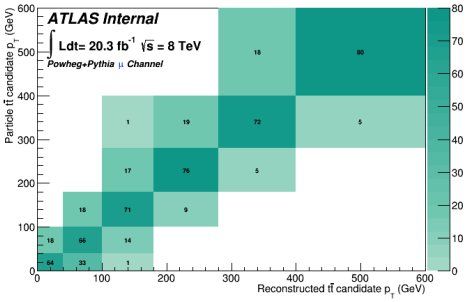

(b) $p_{T,t\bar{t}}$

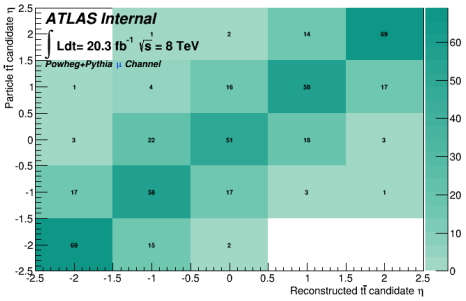

(c) $\eta_{t\bar{t}}$

Figure 5.10: Migration matrices at *particle level* for $m_{t\bar{t}}$, $p_{T,t\bar{t}}$ and $\eta_{t\bar{t}}$ in muon channel

subjected to great fluctuations. However, since these cases are quite limited, these fluctuations does not affect the goodness of the final results.

M_{ij}^{-1} is obtained through an unfolding technique. The unfolding method which has been chosen in this analysis is the Singular Value Decomposition (SVD)[97], because of its property of reducing the statistical fluctuations introduced by the matrix inversion.

After the unfolding, the distribution has to be corrected for the efficiency through the factor $f_{eff.}^{i}$, which is the ratio between the number of events that overcome the selection criteria both at *particle level* and *detector level* selections and the number of the ones which pass only the *particle level* selection.

The differential cross section corrected at *parton level* as a function of

X_{parton} is obtained in a similar way:

$$\frac{d\sigma}{dX_{parton}}(X^i_{parton}) = \frac{N^i_{parton}}{\mathcal{B}\Delta X^i_{parton}\mathcal{L}}$$

$$= \frac{1}{\mathcal{B}\Delta X^i_{parton}\mathcal{L}f^i_{eff.}} \cdot \sum_j M^{-1}_{ij} f^j_{acc.} f_{t\bar{t},\ell+jets} \left(N^j_{reco} - N^j_{reco,bkg}\right)$$

Also in this case, N^j_{reco} is the number of observed events in bin j of X_{reco} with the *detector level* selection applied, N^k_{parton} is the number of events in bin k of X_{parton} in the full phase space, ΔX^k_{parton} is the size of bin k of the *parton level* variable X_{parton}, $f^j_{acc.}$ and $f^i_{eff.}$ are the acceptance and efficiency factors, $f_{t\bar{t},\ell+jets}$ is the fraction of lepton+jets events in the Monte Carlo $t\bar{t}$ sample, $\mathcal{L}$ is the integrated luminosity of the data sample and $\mathcal{B} = 0.4388$ is the branching ratio for $t\bar{t}$ events with exactly one of the W bosons, from the decay of the $t\bar{t}$ pair, decaying to an electron or a muon or a τ lepton.

In Figure 5.11 it is possible to see the migration matrices at *parton level* for $m_{t\bar{t}}$, $p_{T,t\bar{t}}$ and $\eta_{t\bar{t}}$ obtained in the electron channel, while in Figure 5.12 there are the ones obtained in the muon channel.

5.6 Treatment of the uncertainties

5.6.1 Statistical Uncertainties

The measurement is affected by an uncertainty due to the finite size of the data sample. The evaluation of the statistical uncertainty in the case of the cross section measurement requires special attentions. In fact, while the original countings are just subject to Poisson fluctuations, the background subtracted unfolded distributions have uncertainties that depend also on the inverted matrix, introducing a non zero uncertainty correlation mainly among adjacent bins. In addition, an overall correlation is present due to the regularization procedure of the matrix inversion itself. For a general treatment, it has been decided to evaluate the final uncertainties on the cross section measurement using the average fluctuations on a series of pseudo-experiments.

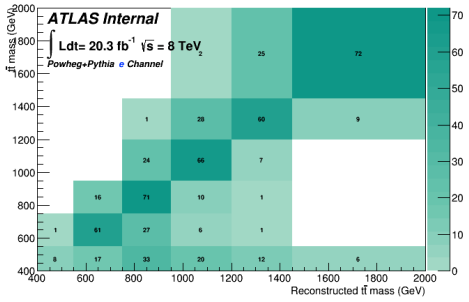

(a) $m_{t\bar{t}}$

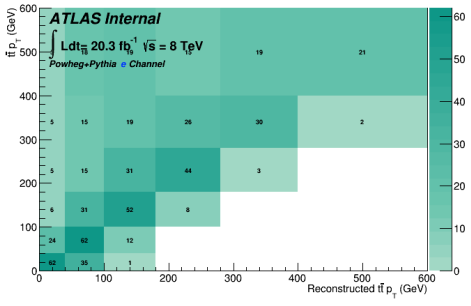

(b) $p_{T,t\bar{t}}$

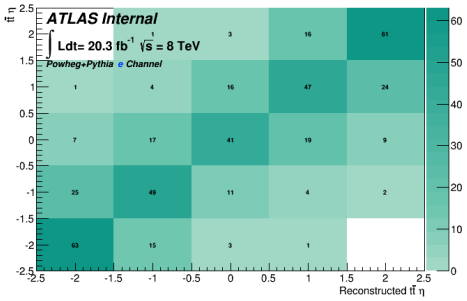

(c) $\eta_{t\bar{t}}$

Figure 5.11: Migration matrices at *parton level* for $m_{t\bar{t}}$, $p_{T,t\bar{t}}$ and $\eta_{t\bar{t}}$ in electron channel

A thousand slightly different replicas of the data is obtained smearing the number of events in each bin N^i_{reco} with a random factor that follows a Poisson distribution. These different distributions are then unfolded to obtain other cross section distributions, which are used to build a covariance matrix. The square roots of the diagonal elements of the covariance matrix correspond to the statistical uncertainties in each bin.

The bin size of every distribution has been chosen in order to have a lower statistical uncertainty with respect to the total systematic uncertainty. In addition, the width of each bin has to be at least one and a half times the expected resolution in that bin.

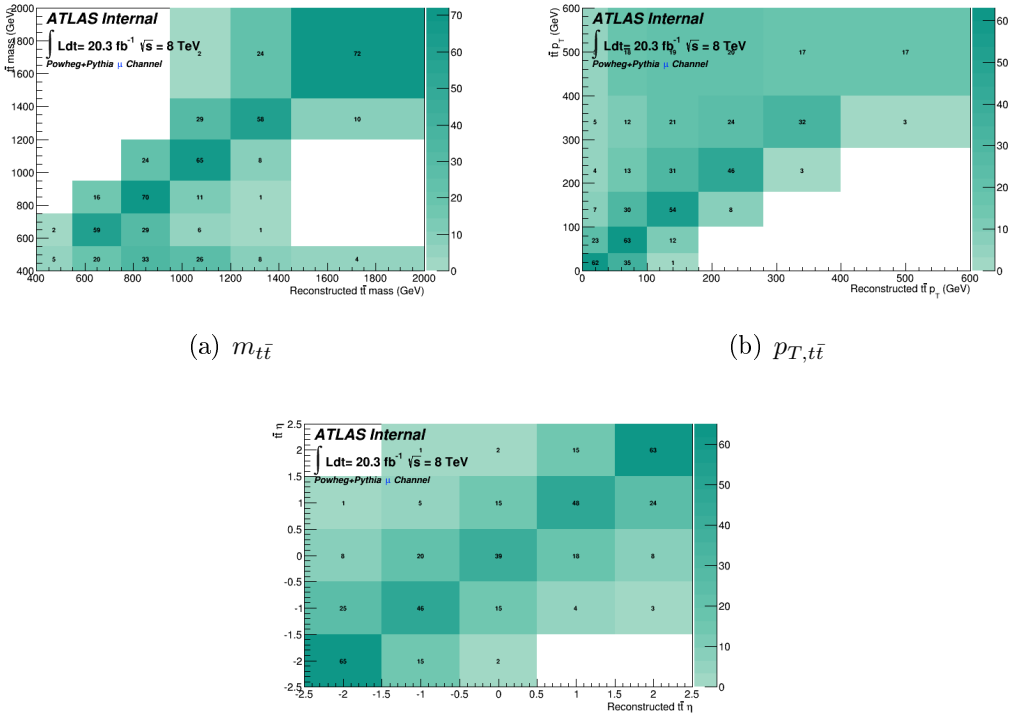

(a) $m_{t\bar{t}}$

(b) $p_{T,t\bar{t}}$

(c) $\eta_{t\bar{t}}$

Figure 5.12: Migration matrices at *parton level* for $m_{t\bar{t}}$, $p_{T,t\bar{t}}$ and $\eta_{t\bar{t}}$ in muon channel

5.6.2 Systematic uncertainties

The evaluation of every systematic uncertainty is done with variations of the nominal distribution by a standard deviation on the error source which is considered, obtaining a new distribution for each source of uncertainty which is shifted with respect to the nominal one. Then, after the event selection and the unfolding procedure, the uncertainty is obtained in each bin as the difference between the nominal and the shifted distribution.

The luminosity measurement is one of the sources of systematic uncertainty; its total uncertainty for the 2012 data set is estimated to be the 3%[99].

This analysis focuses on the measurement of the p_T of the top quartk

through the measuremet of the p_T of the large-R jet. The Jet Energy Scale (JES) calibration term is one of the main contributions to the systematic uncertainty, because of the difficult environment of hadron-hadron colliders. This term depends on various physics effects like the non linearity in the calorimeter response, hardware instabilities of the different detectors which are used; in addition, the measurement can be modified also by energy losses during he jet reconstruction procedures and by additional measured energy linked to underlying and pile-up events.

In particular, in this analysis the dominant uncertainty is the large-R jet energy scale, which is determined computing the uncertainties on the jet energy scale (JES), the mass scale (JMS) and the $\sqrt{d_{12}}$ scale as a function of the large-R jet kinematical variables are calculated, using two different data-driven methods[100]. For $p_T > 800$ GeV in case of JES, and for all p_T in case of JMS and $\sqrt{d_{12}}$ scale, the uncertainty is obtained with a comparison between data and MC in the ratio of the large-R jets kinematic variables reconstructed from the calorimeter cluster to inner detector tracks. In the case of JES and $p_T < 800$ GeV, the values of p_T of large-R jets are compared to the p_T of photons, whose calibration is much more precise, in a large statistics photon+jets sample. In order to consider the different response that the jets may have in these calibration samples (where there are gluon or light quark jets) with respect to $t\bar{t}$ events (where the large-R jets are due to top quarks), an uncertainty linked to large-R JES *topology* is also included. This uncertainty is obtained by evaluating the difference between the responses of these two types of jets in MC events.

Among these uncertainties, the ones on the large-R JES due to the topology represent the dominant contribution to the total uncertainty of the measurement.

Regarding the jets with $R = 0.4$, JES uncerainty is obtained with a combination of simulations, test beam data on high energy hadrons, collision data and *in situ* measurements, as prescribed by the common ATLAS top working group [101], taking in account also additional contributions from

the jet flavour composition, calorimeter response to different jet flavours and pile-up.

The jet energy resolution (JER) and jet mass resolution (JMR) uncertainties take into account the finite resolution on the estimation of these values in the reconstruction phase. In the case of large-R jets, these uncertainties are obtained by evaluating the final results after a smearing of values of energy and mass, obtained after increasig their resolution by 20%[102]. In the case of the jets with $R = 0.4$, they are obtained with an *in situ* measurement of the jet response asymmetry in di-jet events [103].

The efficiency of the b-tagging algorithm on real and fake b jets is corrected in Monte Carlo events by applying scale factors in order to compensate for the residual difference between data and simulation. These scale factors are obtained as a function of p_T and η in $t\bar{t}$ and di-jet samples, using data-driven techniques. The systematic uncertainty linked to the b-tagging is then obtained with a variation of these scale factors within their uncertainty [104], for p_T which are up to 300 GeV. For larger transverse momenta an additional MC-based uncertainty is extrapolated, ranging from $\sim$ 10% to 30%, as the p_T of the b jet increase from 300 GeV to 1200 GeV.

The lepton trigger and reconstruction efficiency in simulation is corrected using scale factors extracted from data in $Z \to \ell^+\ell^-$ enriched control regions. These scale factors are varied within their uncertainties, as well as the lepton energy scale and resolution.

The systematic uncertainty associated to E_T^{miss} is obtaining with the propagation of energy scale and resolution systematics on all physical objects to the E_T^{miss} calculation. The energy deposits which are not associated with any reconstructed object are also considered, leading to additional E_T^{miss} uncertainties.

The main contributions of the background estimation to the systematic uncertainties come from the data-driven calculations.

The systematic uncertainties linked to W+jets are calculated varying the data-driven normalization and the heavy flavour composition scale factors

within their uncertainties.

The fake lepton background uncertainty is estimated using a data driven technique. The efficiency for mis-identifying a jet as an isolated lepton (fake rate) is computed using a fake-enhanced control region. The uncertainty in the parametrisation of the lepton efficiency and the fake rate can be propagated to the *particle* and *parton level*s in order to evaluate the correspondent systematic uncertainty.

The statistical uncertainty on the MC simulation of the $t\bar{t}$ signal and of the background has been estimated to be of the order of $\sim 2\%$, considering the values obtained by the analysis done on the hadronically decaying top p_T spectrum [41] and considering an average statistical error per bin of the MC samples of $\sim 2\%$. The evaluation of uncertainties on the PDFs used in the MC simulation is still on going, but the study done on the hadronically decaying top p_T spectrum [41] shows that their impact is less then 2%.

5.7 Results

The methods described previously have been used to calculate the differential cross section of boosted $t\bar{t}$ production with respect to the mass, the p_T and the η of the $t\bar{t}$ system, both in electron and muon channel.

The results are compared to the predictions obtained with three NLO matrix-element plus parton shower Monte Carlo generators, normalized to the NNLO+NNLL inclusive cross section $\sigma_{t\bar{t}} = 253^{+13}_{-15}$ pb: *Powheg+Pythia*, *Powheg+Herwig* and *MC@NLO+Herwig*.

5.7.1 Cross section measurement for $\frac{d\sigma}{dM_{t\bar{t}}}$

The differential cross section with respect to the mass of the $t\bar{t}$ system has been extracted from the unfolded distribution, which has been obtained with the SVD method, with a *k factor*=3 and a truth distribution made with the *Powheg+Pythia* generator. The resulting spectra of the unfolded differential cross section, compared with the predictions from *Powheg+Pythia*,

Powheg+Herwig and *MC@NLO+Herwig*, are shown in Figure 5.13, for the results obtained at *particle level* in the fiducial phase space, and in Figure 5.14 for the *parton level* in the full phase space.

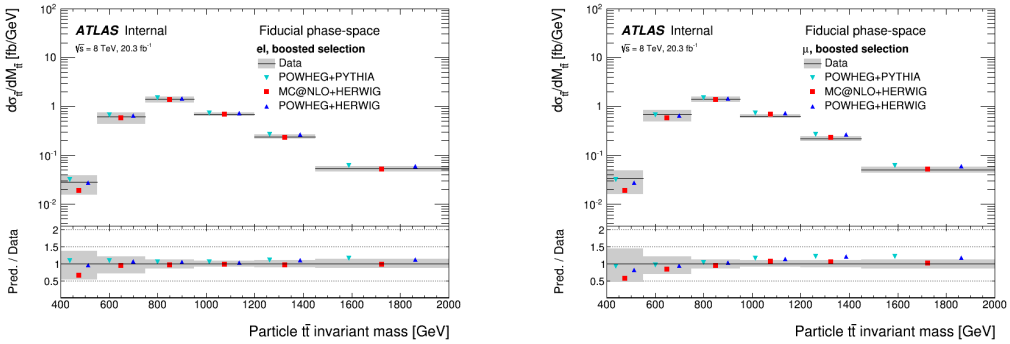

(a) el+jets (b) μ+jets

Figure 5.13: Unfolded differential cross section for the $M_{t\bar{t}}$ spectrum calculated at *particle level* in the fiducial phase space in (a)electron channel and (b) muon channel. The shaded area correspons to the measured valus and the total uncertainty, while the coloured marks represent the MC predictions. In the lower part of the plots there is the ratio between the MC predictions and the measured values.

At *particle level*, the unfolded distribution is in good agreement with the theoretical predictions: for every bin of the histogram describing the distribution, the ratio between the population from the Monte Carlo simulations and the unfolding of real data (shown in the bottom part of the plots) is within the uncertainties in the first bins, and always lower then 1.5. It can be seen a general tendency of the Monte Carlo simulation to overestimate the data distribution, especially for increasing invariant masses. The same consideration are valid for the μ+jets channel.

At *parton level*, the unfolded distribution is in even better agreement with the theoretical predictions with respect to the *particle level*: for every bin of the histogram describing the distribution, the ratio between the population from the unfolding of real data and the Monte Carlo simulations (shown in the bottom part of the plots) is very close to 1. In the electron channel the

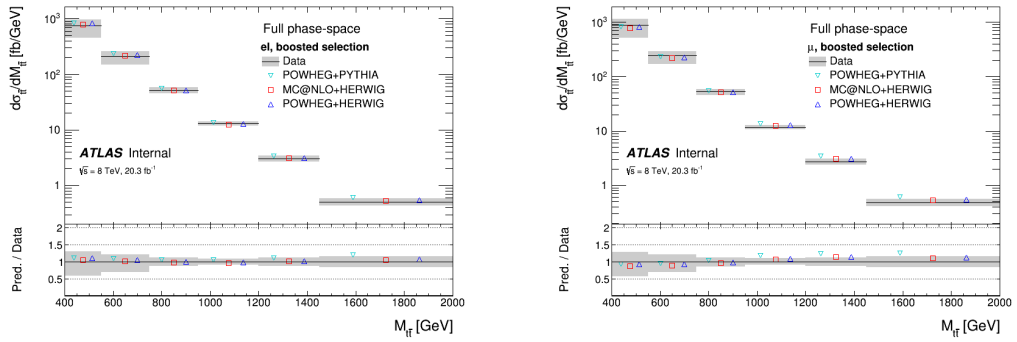

(a) el+jets (b) μ+jets

Figure 5.14: Unfolded differential cross section for the $M_{t\bar{t}}$ spectrum calculated at *parton level* in the full phase space in (a)electron channel and (b) muon channel. The shaded area correspons to the measured valus and the total uncertainty, while the coloured marks represent the MC predictions. In the lower part of the plots there is the ratio between the MC predictions and the measured values.

ratio for Powheg+Pythia, Powheg+Herwig and MC@NLO is always within the uncertainties, even if it can be seen a general tendency to overestimate the data for increasing invariant masses. This effect is even more visible in the μ+jets channel.

The differential cross section with respect to the mass of the $t\bar{t}$ system at *particle* and *parton level* in the different bins is listed in Table 5.2 for the electron channel, and in Table 5.3 for the muon channel.

	Particle level			Parton level		
$M_{t\bar{t}}$[GeV]	$d\sigma_{t\bar{t}}/dM_{t\bar{t}}$[fb/GeV]	Stat. Unc.[%]	Total Unc.[%]	$d\sigma_{t\bar{t}}/dM_{t\bar{t}}$[fb/GeV]	Stat. Unc.[%]	Total Unc.[%]
400 - 550	0.028	±28	+46/-37	748.4	±15	+40/-30
550 - 750	0.61	±6	+29/-21	212.7	±6	+29/-22
750 - 950	1.39	±3	+14/-13	51.6	±3	+13/-13
950 - 1200	0.69	±3	+9/-9	13.0	±4	+9/-9
1200 - 1450	0.24	±6	+10/-11	3.05	±7	+11/-12
1450 - 2000	0.053	±9	+13/-14	0.504	±12	+15/-17

Table 5.2: The electron+jets unfolded spectrum at *particle level* in the fiducial phase space and *parton level* in the full phase space.

In Table 5.4 and 5.5 there is a summary of the effects of the systematic

	Particle level			Parton level		
$M_{t\bar{t}}$[GeV]	$d\sigma_{t\bar{t}}/dM_{t\bar{t}}$[fb/GeV]	Stat. Unc.[%]	Total Unc.[%]	$d\sigma_{t\bar{t}}/dM_{t\bar{t}}$[fb/GeV]	Stat. Unc.[%]	Total Unc.[%]
400 - 550	0.033	±38	+53/-44	889.2	±15	+42/-29
550 - 750	0.68	±7	+30/-21	242.0	±7	+30/-21
750 - 950	1.41	±3	+14/-13	52.6	±4	+13/-13
950 - 1200	0.63	±4	+9/-11	11.6	±5	+9/-11
1200 - 1450	0.22	±6	+11/-11	2.73	±8	+12/-12
1450 - 2000	0.050	±9	+13/-13	0.481	±12	+15/-16

Table 5.3: The muon+jets unfolded spectrum at *particle level* in the fiducial phase space and *parton level* in the full phase space.

uncertainties at *particle* and *parton level* which have been considerded in the analysis for the electron channel, while Table 5.6 and 5.7 are referred to the muon channel.

PARTICLE LEVEL SPECTRUM - *el*+jets						
Uncertainity	400 - 550	550 - 750	750 - 950	950 - 1200	1200 - 1450	1450 - 2000
Large-R jet p_T resolution	5.2/-5.2	3.7/-3.7	- / -	- / -	- / -	- / -
Large-R jet $\sqrt{d_{12}}$ scale	2.7/ -	2.1/ -	- / -	- / -	- / -	- / -
Large-R jet mass scale	- / -	- /-2.1	2.7/-3.2	3.3/-3.3	3.4/-3.1	3.5/-3.2
Large-R jet JES (data vs MC)	10.6/-8.6	8.5/-7.1	4.4/-4.4	3.1/-2.9	3.2/-3.1	3.5/-3.8
Large-R jet JES (cut on subleading small-R jet)	3.1/ -	2.4/ -	- / -	- / -	- / -	- / -
Large-R jet JES (photon energy scale)	5.8/-3.4	4.5/-2.9	- / -	- / -	- / -	- / -
Large-R jet JES (generator)	2.9/ -	2.3/ -	- / -	- / -	- / -	- / -
Large-R jet JES (statistics)	2.6/ -	2.0/ -	- / -	- / -	- / -	- /-2.4
Large-R jet JES (correlation with JMS)	3.6/-3.0	2.9/-2.6	- / -	- / -	- / -	- / -
Large-R jet JES (topology)	31.0/-19.0	24.2/-15.8	11.0/-9.5	4.3/-4.8	2.0/-3.2	- /-2.9
Small-R jet JES	9.8/-10.1	7.0/-6.6	-/-	-/-	-/-	-/-2.1
b-tagging b-jet efficiency	- / -	- / -	- / -	2.8/-2.6	3.7/-3.5	4.2/-4.0
e energy scale	- / -	- / -	- / -	-2.2/ -	-3.2/2.2	-4.0/2.4
Luminosity	3.0/-3.0	3.0/-3.0	3.0/-3.0	3.0/-3.0	3.0/-3.0	3.0/-3.0
Systematic	36.5/-24.5	28.4/-20.2	13.4/-12.3	8.5/-8.7	8.5/-9.5	8.9/-11.0
Data statistics	±28	±6	±3	±3	±6	±9
Total	46/-37	29/-21	14/-13	9/-9	10/-11	13/-14

Table 5.4: Systematic uncertainties on the electron+jets unfolded spectrum at *particle level* in the fiducial phase space. Values below 2% are not shown.

PARTON LEVEL SPECTRUM - *el*+jets						
Uncertainity	400 - 550	550 - 750	750 - 950	950 - 1200	1200 - 1450	1450 - 2000
Large-R jet p_T resolution	5.3/-5.3	3.7/-3.7	- / -	- / -	- / -	- / -
Large-R jet $\sqrt{d_{12}}$ scale	2.7/ -	2.1/ -	- / -	- / -	- / -	- / -
Large-R jet mass scale	- / -	- /-2.1	2.7/-3.3	3.4/-3.3	3.5/-3.1	3.6/-3.2
Large-R jet JES (data vs MC)	11.0/-9.3	8.6/-7.5	4.1/-4.3	2.8/-2.5	3.1/-2.9	3.3/-3.8
Large-R jet JES (cut on subleading small-R jet)	3.2/ -	2.5/ -	- / -	- / -	- / -	- / -
Large-R jet JES (photon energy scale)	6.2/-3.4	4.6/-2.9	- / -	- / -	- / -	- / -
Large-R jet JES (generator)	3.0/ -	2.3/ -	- / -	- / -	- / -	- / -
Large-R jet JES (statistics)	2.6/ -	2.0/ -	- / -	- / -	- / -	- /-2.9
Large-R jet JES (correlation with JMS)	3.8/-3.0	3.1/-2.6	- / -	- / -	- / -	- / -
Large-R jet JES (topology)	31.8/-20.1	24.4/-16.4	10.3/-9.4	3.0/-3.9	- /-2.1	- / -
Small-R jet JES	10.1/-10.5	7.2/-6.9	-/-	-/-	-/-2.2	-/-3.2
b-tagging b-jet efficiency	- / -	- / -	- / -	3.0/-2.8	4.0/-3.9	4.7/-4.5
e energy scale	- / -	- / -	- / -	-2.3/ -	-3.7/2.5	-4.6/2.7
Luminosity	3.0/-3.0	3.0/-3.0	3.0/-3.0	3.0/-3.0	3.0/-3.0	3.0/-3.0
Systematic	37.6/-25.7	28.8/-20.8	12.6/-12.1	8.0/-8.4	8.7/-9.9	9.4/-12.1
Data statistics	±15	±6	±3	±4	±7	±12
Total	40/-30	29/-22	13/-13	9/-9	11/-12	15/-17

Table 5.5: Systematic uncertainties on the electron+jets unfolded spectrum at *parton level* in the full phase space. Values below 2% are not shown.

PARTICLE LEVEL SPECTRUM - μ+jets						
Uncertainity	400 - 550	550 - 750	750 - 950	950 - 1200	1200 - 1450	1450 - 2000
Large-R jet p_T resolution	6.6/-6.6	4.9/-4.9	- / -	- / -	- / -	- / -
Large-R jet mass resolution	3.1/-3.1	2.1/-2.1	- / -	- / -	- / -	- / -
Large-R jet mass scale	- /2.4	- / -	2.8/-2.5	3.3/-3.8	3.3/-3.7	3.2/-3.6
Large-R jet JES (data vs MC)	10.4/-9.1	8.4/-7.7	4.6/-5.0	2.6/-3.4	3.0/-3.3	3.7/-3.8
Large-R jet JES (cut on subleading small-R jet)	3.6/ -	2.8/ -	- / -	- / -	- / -	- / -
Large-R jet JES (photon energy scale)	5.0/-2.8	4.1/-2.6	2.1/-2.3	- / -	- / -	- / -
Large-R jet JES (generator)	3.2/ -	2.6/ -	- / -	- / -	- / -	- / -
Large-R jet JES (definition of small-R jet inside large-R jet)	2.7/ -	2.0/ -	- / -	- / -	- / -	- / -
Large-R jet JES (statistics)	2.9/ -	2.3/ -	- / -	- / -	- / -	- / -
Large-R jet JES (correlation with JMS)	4.4/-3.5	3.7/-3.1	2.1/-2.2	- / -	- / -	- / -
Large-R jet JES (topology)	29.6/-18.2	23.3/-15.4	10.9/-9.5	3.9/-5.1	2.5/-3.2	2.5/-2.8
Large-R jet JES (pileup offset) μ	- /2.7	- / -	- / -	- / -	- / -	- / -
Small-R jet JES	5.5/-12.0	3.4/-8.1	-/-	-/-	-/-	-/-2.1
Small-R jet energy resolution	3.7/-3.7	2.7/-2.7	- / -	- / -	- / -	- / -
b-tagging b-jet efficiency	- / -	- / -	2.0/ -	2.8/-2.5	3.5/-3.5	3.9/-4.1
μ trigger efficiency	3.0/ -	2.8/ -	2.1/ -	- / -	- / -	- / -
Luminosity	3.0/-3.0	3.0/-3.0	3.0/-3.0	3.0/-3.0	3.0/-3.0	3.0/-3.0
Systematic	37.1/-23.6	28.8/-19.6	13.6/-12.5	8.1/-9.7	8.7/-9.3	9.5/-9.8
Data statistics	±38	±7	±3	±4	±6	±9
Total	53/-44	30/-21	14/-13	9/-11	11/-11	13/-13

Table 5.6: Systematic uncertainties on the muon+jets unfolded spectrum at *particle level* in the fiducial phase space. Values below 2% are not shown.

PARTON LEVEL SPECTRUM - μ+jets						
Uncertainity	400 - 550	550 - 750	750 - 950	950 - 1200	1200 - 1450	1450 - 2000
Large-R jet p_T resolution	7.2/-7.2	5.1/-5.1	- / -	- / -	- / -	- / -
Large-R jet mass resolution	3.2/-3.2	2.1/-2.1	- / -	- / -	- / -	- / -
Large-R jet mass scale	- /2.8	- / -	2.8/-2.7	3.4/-4.1	3.3/-4.0	3.2/-3.8
Large-R jet JES (data vs MC)	11.0/-9.6	8.7/-8.0	4.4/-4.9	2.1/-2.9	2.8/-3.1	3.7/-3.8
Large-R jet JES (cut on subleading small-R jet)	3.9/ -	3.0/ -	- / -	- / -	- / -	- / -
Large-R jet JES (photon energy scale)	5.1/-3.0	4.1/-2.7	2.1/-2.3	- / -	- / -	- / -
Large-R jet JES (generator)	3.3/ -	2.6/ -	- / -	- / -	- / -	- / -
Large-R jet JES (definition of small-R jet inside large-R jet)	2.8/ -	2.1/ -	- / -	- / -	- / -	- / -
Large-R jet JES (statistics)	3.0/ -	2.3/ -	- / -	- / -	- / -	- / -
Large-R jet JES (correlation with JMS)	4.6/-3.7	3.8/-3.2	2.0/-2.2	- / -	- / -	- / -
Large-R jet JES (topology)	31.3/-19.1	24.0/-15.9	10.2/-9.4	2.3/-4.2	- /-2.1	- / -
Large-R jet JES (pileup offset) μ	- /2.9	- / -	- / -	- / -	- / -	- / -
Small-R jet JES	6.8/-12.7	3.7/-8.3	-/-	-/-	3.1/-3.0	3.9/-3.2
Small-R jet energy resolution	3.8/-3.8	2.6/-2.6	- / -	- / -	- / -	- / -
b-tagging b-jet efficiency	- / -	- / -	2.1/ -	2.9/-2.7	3.8/-3.8	4.3/-4.6
μ trigger efficiency	2.9/ -	2.7/ -	2.1/ -	- / -	- / -	- / -
Luminosity	3.0/-3.0	3.0/-3.0	3.0/-3.0	3.0/-3.0	3.0/-3.0	3.0/-3.0
Systematic	39.1/-24.9	29.6/-20.3	12.9/-12.4	7.7/-9.7	8.9/-9.5	10.1/-10.3
Data statistics	±15	±7	±4	±5	±7	±12
Total	42/-29	30/-21	13/-13	9/-11	12/-12	15/-16

Table 5.7: Systematic uncertainties on the muon+jets unfolded spectrum at *parton level* in the full phase space. Values below 2% are not shown.

5.7.2 Cross section measurement for $\frac{d\sigma}{dp_{T,t\bar{t}}}$

The differential cross section with respect to the p_T of the $t\bar{t}$ system has been extracted from the unfolded distribution, which has been obtained with the SVD method, with a *k factor*=3 and a truth distribution made with the *Powheg+Pythia* generator.

The resulting spectra of the unfolded differential cross section, compared with the predictions from *Powheg+Pythia*, *Powheg+Herwig* and *MC@NLO+Herwig*, are shown in Figure 5.15, for the results obtained at *particle level* in the fiducial phase space, and in Figure 5.16 for the *parton level* in the full phase space.

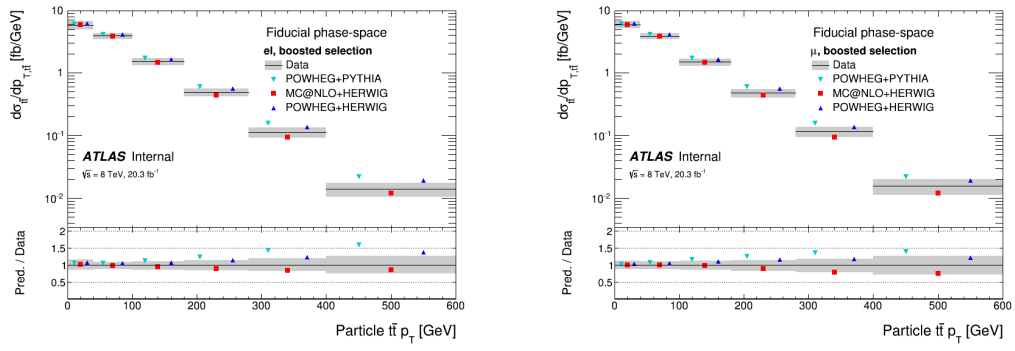

(a) el+jets (b) μ+jets

Figure 5.15: Unfolded differential cross section for the $p_{T,t\bar{t}}$ spectrum calculated at *particle level* in the fiducial phase space in (a)electron channel and (b) muon channel. The shaded area correspons to the measured valus and the total uncertainty, while the coloured marks represent the MC predictions. In the lower part of the plots there is the ratio between the MC predictions and the measured values.

At *particle level*, the unfolded distribution is in good agreement with the theoretical predictions: for every bin of the histogram describing the distribution, the ratio between the population from the unfolding of real data and the Monte Carlo simulations (shown in the bottom part of the plots) is lower then 1.5. In particular, for Powheg+Pythia and Powheg+Herwig the ratio tends to rise for higher values of p_T, while for MC@NLO it is generally

within the uncertainties, showing higher values in the first bins, and lowering for higher values of p_T.

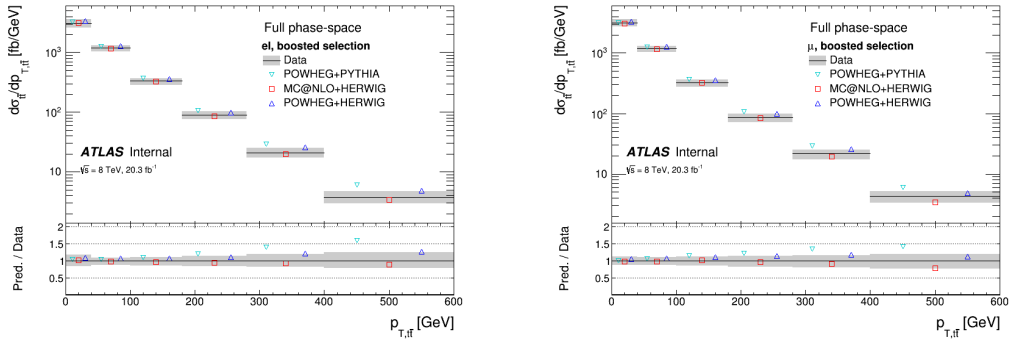

(a) el+jets (b) μ+jets

Figure 5.16: Unfolded differential cross section for the $p_{T,t\bar{t}}$ spectrum calculated at *parton level* in the full phase space in (a)electron channel and (b) muon channel. The shaded area correspons to the measured valus and the total uncertainty, while the coloured marks represent the MC predictions. In the lower part of the plots there is the ratio between the MC predictions and the measured values.

At *parton level*, the unfolded distribution shows the same agreement with the theoretical predictions as at *particle level*: for every bin of the histogram describing the distribution, the ratio between the population from the unfolding of real data and the Monte Carlo simulations (shown in the bottom part of the plots) is lower then 1.5. Also in this case, for Powheg+Pythia and Powheg+Herwig the ratio tends to rise for higher values of p_T, while for MC@NLO lowers for the same values, remaining always within the uncertainties.

The differential cross section with respect to the mass of the $t\bar{t}$ system at *particle* and *parton level* in the different bins is listed in Table 5.8 for the electron channel, and in Table 5.9 for the muon channel.

In Table 5.10 and 5.11 there is a summary of the effects of the systematic uncertainties at *particle* and *parton level* which have been considerded in the analysis for the electron channel, while Table 5.12 and 5.13 are referred to

	Particle level			Parton level		
$p_{T,t\bar{t}}$[GeV]	$d\sigma_{t\bar{t}}/dp_{T,t\bar{t}}$[fb/GeV]	Stat. Unc.[%]	Total Unc.[%]	$d\sigma_{t\bar{t}}/dp_{T,t\bar{t}}$[fb/GeV]	Stat. Unc.[%]	Total Unc.[%]
0 - 40	5.79	±4	+15/-17	3062.8	±4	+15/-17
40 - 100	3.93	±3	+12/-9	1194.5	±4	+13/-10
100 - 180	1.55	±5	+14/-11	334.0	±5	+14/-11
180 - 280	0.49	±7	+15/-15	89.2	±7	+15/-15
280 - 400	0.11	±12	+18/-20	20.9	±11	+17/-20
400 - 600	0.014	±21	+25/-27	3.77	±17	+22/-24

Table 5.8: The electron+jets unfolded spectrum at *particle level* in the fiducial phase space and *parton level* in the full phase space.

	Particle level			Parton level		
$p_{T,t\bar{t}}$[GeV]	$d\sigma_{t\bar{t}}/dp_{T,t\bar{t}}$[fb/GeV]	Stat. Unc.[%]	Total Unc.[%]	$d\sigma_{t\bar{t}}/dp_{T,t\bar{t}}$[fb/GeV]	Stat. Unc.[%]	Total Unc.[%]
0 - 40	5.96	±4	+13/-13	3167.4	±4	+13/-13
40 - 100	3.90	±3	+12/-11	1182.7	±4	+12/-12
100 - 180	1.50	±5	+15/-13	321.9	±6	+15/-13
180 - 280	0.49	±8	+18/-14	87.0	±8	+18/-14
280 - 400	0.12	±13	+20/-18	21.7	±11	+20/-17
400 - 600	0.016	±24	+29/-27	4.26	±16	+23/-20

Table 5.9: The muon+jets unfolded spectrum at *particle level* in the fiducial phase space and *parton level* in the full phase space.

the muon channel.

PARTICLE LEVEL SPECTRUM - *el*+jets						
Uncertainty	0 - 40	40 - 100	100 - 180	180 - 280	280 - 400	400 - 600
Large-R jet p_T resolution	- / -	- / -	2.8/-2.8	2.1/-2.1	- / -	- / -
Large-R jet mass scale	2.5/-3.0	3.1/-3.0	3.2/-3.1	2.8/-3.1	2.4/-3.3	2.1/-3.3
Large-R jet JES (data vs MC)	4.6/-6.2	3.6/-2.4	4.6/-3.2	5.7/-5.8	6.3/-7.0	6.4/-7.4
Large-R jet JES (photon energy scale)	2.5/-2.8	- / -	- / -	2.0/-2.2	2.6/-3.2	2.9/-3.7
Large-R jet JES (statistics)	- / -	- / -	- / -	- / -	2.8/-2.7	3.2/-3.2
Large-R jet JES (correlation with JMS)	2.5/-2.5	- / -	- / -	- /-2.5	2.5/-3.5	2.7/-4.0
Large-R jet JES (topology)	10.3/-11.2	9.2/-6.3	9.6/-6.6	9.3/-8.5	8.4/-9.1	7.7/-9.1
Small-R jet JES	5.0/-3.9	-/-	-/-	-/-3.7	-/-4.7	2.7/-5.3
Small-R jet energy resolution	-2.4/2.4	- / -	- / -	- / -	- / -	- / -
b-tagging b-jet efficiency	- / -	2.2/ -	2.4/ -	2.4/ -	2.3/ -	2.3/ -
E_T^{miss} unassociated cells scale	-2.3/ -	- / -	- / -	- / -	- / -	- / -
Luminosity	3.0/-3.0	3.0/-3.0	3.0/-3.0	3.0/-3.0	3.0/-3.0	3.0/-3.0
Multijet	- / -	- / -	- / -	- / -	- /-2.1	2.8/-3.0
Systematic	14.2/-16.1	11.8/-8.9	13.0/-10.0	13.2/-13.4	13.3/-15.7	13.6/-16.8
Data statistics	±4	±3	±5	±7	±12	±21
Total	15/-17	12/-9	14/-11	15/-15	18/-20	25/-27

Table 5.10: Systematic uncertainties on the electron+jets unfolded spectrum at *particle level* in the fiducial phase space. Values below 2% are not shown.

PARTON LEVEL SPECTRUM - *el*+jets						
Uncertainty	0 - 40	40 - 100	100 - 180	180 - 280	280 - 400	400 - 600
Large-R jet p_T resolution	- / -	- / -	3.1/-3.1	2.3/-2.3	- / -	- / -
Large-R jet mass scale	2.4/-3.0	3.1/-3.0	3.4/-3.0	2.9/-3.1	2.4/-3.3	2.1/-3.3
Large-R jet JES (data vs MC)	4.5/-6.4	3.5/-2.2	4.4/-2.5	5.7/-5.5	6.3/-7.3	6.6/-7.9
Large-R jet JES (cut on subleading small-R jet)	- / -	- / -	- / -	- / -	- / -	- /-2.3
Large-R jet JES (photon energy scale)	2.6/-3.0	- / -	- / -	- /-2.0	2.6/-3.3	3.0/-4.0
Large-R jet JES (definition of small-R jet inside large-R jet)	- / -	- / -	- / -	- / -	- / -	- /-2.2
Large-R jet JES (statistics)	- / -	- / -	- / -	- / -	2.9/-2.7	3.3/-3.3
Large-R jet JES (correlation with JMS)	2.6/-2.5	- / -	- / -	- /-2.3	2.6/-3.6	2.8/-4.2
Large-R jet JES (topology)	10.3/-11.5	9.3/-6.2	9.7/-6.1	9.5/-8.4	8.5/-9.4	7.7/-9.6
Small-R jet JES	6.0/-4.6	-/-	-/-	-/-2.2	-/-4.6	2.6/-5.2
Small-R jet energy resolution	-2.6/2.6	- / -	- / -	- / -	- / -	- / -
b-tagging b-jet efficiency	- / -	2.2/-2.0	2.4/-2.0	2.4/ -	2.3/ -	2.3/ -
E_T^{miss} unassociated cells scale	-2.6/ -	- / -	2.0/ -	- / -	- / -	- / -
Luminosity	3.0/-3.0	3.0/-3.0	3.0/-3.0	3.0/-3.0	3.0/-3.0	3.0/-3.0
Multijet	- / -	- / -	- / -	- / -	- /-2.0	2.9/-3.1
Systematic	14.5/-16.8	11.9/-8.8	13.2/-9.5	13.3/-13.1	13.4/-16.0	13.6/-17.5
Data statistics	±4	±4	±5	±7	±11	±17
Total	15/-17	13/-10	14/-11	15/-15	17/-20	22/-24

Table 5.11: Systematic uncertainties on the electron+jets unfolded spectrum at *parton level* in the full phase space. Values below 2% are not shown.

PARTICLE LEVEL SPECTRUM - μ+jets						
Uncertainty	0 - 40	40 - 100	100 - 180	180 - 280	280 - 400	400 - 600
Large-R jet p_T resolution	- / -	- / -	2.3/-2.3	2.2/-2.2	- / -	- / -
Large-R jet $\sqrt{d_{12}}$ scale	- / -	- / -	- / -	- / -	- / -	2.1/ -
Large-R jet mass scale	2.7/-2.8	2.9/-2.7	3.1/-2.6	3.0/-2.2	2.7/ -	2.4/ -
Large-R jet JES (data vs MC)	4.1/-4.9	3.8/-4.1	4.6/-5.0	6.2/-5.4	6.9/-5.6	7.2/-5.8
Large-R jet JES (cut on subleading small-R jet)	- / -	- / -	- / -	- / -	2.1/ -	2.2/ -
Large-R jet JES (photon energy scale)	- /-2.1	- / -	2.2/-2.1	2.7/ -	2.8/-2.2	2.8/-2.4
Large-R jet JES (statistics)	- / -	- / -	- / -	2.2/ -	2.9/-2.1	3.1/-2.5
Large-R jet JES (correlation with JMS)	- /-2.2	- /-2.0	2.3/-2.1	3.2/ -	3.3/ -	3.2/ -
Large-R jet JES (topology)	9.1/-9.2	8.7/-7.4	10.0/-7.5	10.6/-7.6	10.0/-7.4	9.4/-7.2
Small-R jet energy resolution	- / -	- / -	- / -	2.8/-2.8	3.1/-3.1	3.1/-3.1
b-tagging b-jet efficiency	2.4/-2.1	2.5/-2.1	2.4/-2.1	2.5/-2.5	2.7/-2.8	2.8/-3.0
μ trigger efficiency	- / -	- / -	2.2/ -	2.4/ -	2.2/ -	2.1/ -
Luminosity	3.0/-3.0	3.0/-3.0	3.0/-3.0	3.0/-3.0	3.0/-3.0	3.0/-3.0
Systematic	12.1/-12.7	11.5/-10.7	13.8/-11.7	15.9/-11.9	16.0/-12.1	15.9/-12.3
Data statistics	±4	±3	±5	±8	±13	±24
Total	13/-13	12/-11	15/-13	18/-14	20/-18	29/-27

Table 5.12: Systematic uncertainties on the electron+jets unfolded spectrum at *particle level* in the fiducial phase space. Values below 2% are not shown.

PARTON LEVEL SPECTRUM - μ+jets						
Uncertainty	0 - 40	40 - 100	100 - 180	180 - 280	280 - 400	400 - 600
Large-R jet p_T resolution	- / -	- / -	2.4/-2.4	2.4/-2.4	- / -	- / -
Large-R jet $\sqrt{d_{12}}$ scale	- / -	- / -	- / -	- / -	- / -	2.2/ -
Large-R jet mass scale	2.7/-2.8	2.9/-2.8	3.1/-2.8	3.1/-2.3	2.7/ -	2.3/ -
Large-R jet JES (data vs MC)	4.0/-4.7	3.5/-4.1	4.3/-5.0	6.0/-5.5	6.9/-5.7	7.2/-5.9
Large-R jet JES (cut on subleading small-R jet)	- / -	- / -	- / -	- / -	2.1/ -	2.2/ -
Large-R jet JES (photon energy scale)	- /-2.1	- /-2.0	2.1/-2.1	2.6/ -	2.8/-2.2	2.8/-2.4
Large-R jet JES (statistics)	- / -	- / -	- / -	2.1/ -	2.8/-2.1	3.1/-2.5
Large-R jet JES (correlation with JMS)	- /-2.2	- /-2.1	2.2/-2.2	3.2/ -	3.3/ -	3.2/ -
Large-R jet JES (topology)	8.9/-9.2	8.6/-7.5	10.0/-7.6	10.9/-7.7	10.1/-7.5	9.4/-7.3
Small-R jet energy resolution	- / -	- / -	- / -	2.8/-2.8	3.0/-3.0	3.0/-3.0
b-tagging b-jet efficiency	2.4/-2.1	2.4/-2.0	2.3/-2.0	2.4/-2.4	2.7/-2.8	2.8/-3.1
μ trigger efficiency	- / -	- / -	2.2/ -	2.4/ -	2.3/ -	2.1/ -
Luminosity	3.0/-3.0	3.0/-3.0	3.0/-3.0	3.0/-3.0	3.0/-3.0	3.0/-3.0
Systematic	11.9/-12.7	11.3/-10.8	13.6/-11.8	16.0/-12.0	16.1/-12.2	15.9/-12.4
Data statistics	±4	±4	±6	±8	±11	±16
Total	13/-13	12/-12	15/-13	18/-14	20/-17	23/-20

Table 5.13: Systematic uncertainties on the electron+jets unfolded spectrum at *parton level* in the full phase space. Values below 2% are not shown.

5.7.3 Cross section measurement for $\frac{d\sigma}{d\eta_{t\bar{t}}}$

The differential cross section with respect to the η of the $t\bar{t}$ system has been extracted from the unfolded distribution, which has been obtained with the SVD method, with a $k\,factor$=3 and a truth distribution made with the *Powheg+Pythia* generator.

The resulting spectra of the unfolded differential cross section, compared with the predictions from *Powheg+Pythia*, *Powheg+Herwig* and *MC@NLO+Herwig*, are shown in Figure 5.17, for the results obtained at *particle level* in the fiducial phase space, and in Figure 5.18 for the *parton level* in the full phase space.

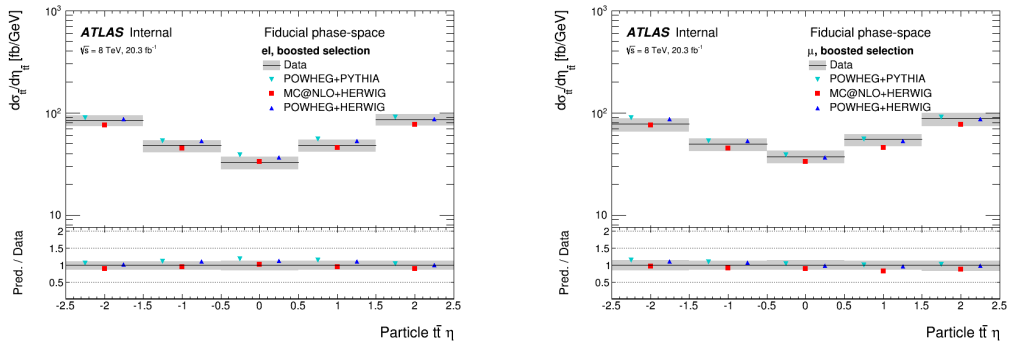

(a) el+jets (b) μ+jets

Figure 5.17: Unfolded differential cross section for the $\eta_{t\bar{t}}$ spectrum calculated at *particle level* in the fiducial phase space in (a)electron channel and (b) muon channel. The shaded area correspons to the measured valus and the total uncertainty, while the coloured marks represent the MC predictions. In the lower part of the plots there is the ratio between the MC predictions and the measured values.

At *particle level*, the unfolded distribution is slightly overestimated by the theoretical predictions, but still in good agreement: for every bin of the histogram describing the distribution, the ratio between the population from the unfolding of real data and the Monte Carlo simulations (shown in the bottom part of the plots) is within the uncertainties.

At *parton level*, there is the same agreement between unfolded distri-

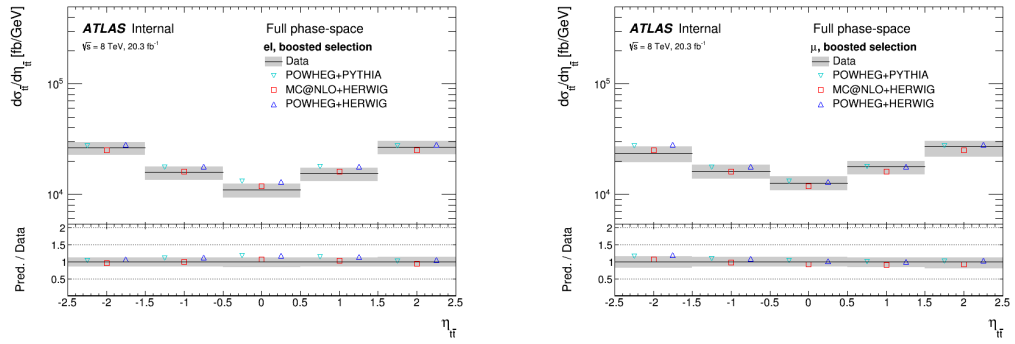

(a) el+jets (b) μ+jets

Figure 5.18: Unfolded differential cross section for the $\eta_{t\bar{t}}$ spectrum calculated at *parton level* in the full phase space

bution and theoretical predictions as at *particle level*: for every bin of the histogram describing the distribution, the ratio between the population from the unfolding of real data and the Monte Carlo simulations (shown in the bottom part of the plots) is within the uncertainties.

The differential cross section with respect to the rapidity of the $t\bar{t}$ system at *particle* and *parton level* in the different bins is listed in Table 5.14 for the electron channel, and in Table 5.15 for the muon channel.

	Particle level			Parton level		
$\eta_{t\bar{t}}$	$d\sigma_{t\bar{t}}/d\eta_{t\bar{t}}$[fb]	Stat. Unc.[%]	Total Unc.[%]	$d\sigma_{t\bar{t}}/d\eta_{t\bar{t}}$[fb]	Stat. Unc.[%]	Total Unc.[%]
-2.5 - -1.5	84.76	±7	+13/-11	26237.6	±8	+13/-12
-1.5 - -0.5	47.90	±7	+14/-12	15825.1	±7	+14/-12
-0.5 - 0.5	32.88	±8	+15/-13	11043.2	±9	+16/-13
0.5 - 1.5	48.23	±7	+15/-13	15443.0	±8	+15/-13
1.5 - 2.5	86.15	±7	+14/-13	26654.9	±9	+14/-14

Table 5.14: The electron+jets unfolded spectrum at *particle level* in the fiducial phase space and *parton level* in the full phase space.

In Table 5.16 and 5.17 there is a summary of the effects of the systematic uncertainties at *particle* and *parton level* which have been considerded in the analysis for the electron channel, while Table 5.18 and 5.19 are referred to

	Particle level			Parton level		
$\eta_{t\bar{t}}$	$d\sigma_{t\bar{t}}/d\eta_{t\bar{t}}$[fb]	Stat. Unc.[%]	Total Unc.[%]	$d\sigma_{t\bar{t}}/d\eta_{t\bar{t}}$[fb]	Stat. Unc.[%]	Total Unc.[%]
-2.5 - -1.5	77.86	±8	+16/-14	23477.7	±10	+18/-15
-1.5 - -0.5	49.20	±8	+14/-13	16162.0	±8	+15/-14
-0.5 - 0.5	37.27	±9	+14/-14	12678.0	±9	+15/-14
0.5 - 1.5	55.02	±8	+14/-13	17735.4	±8	+15/-13
1.5 - 2.5	88.48	±8	+17/-12	26944.6	±9	+19/-13

Table 5.15: The muon+jets unfolded spectrum at *particle level* in the fiducial phase space and *parton level* in the full phase space.

the muon channel.

PARTICLE LEVEL SPECTRUM - *el*+jets					
Uncertainty	-2.5 - -1.5	-1.5 - -0.5	-0.5 - 0.5	0.5 - 1.5	1.5 - 2.5
Large-R jet p_T resolution	2.4/-2.4	2.1/-2.1	- / -	- / -	- / -
Large-R jet mass scale	2.8/-3.2	2.9/-3.6	3.2/-3.9	3.4/-3.4	3.4/-2.7
Large-R jet JES (data vs MC)	3.3/ -	3.2/ -	3.0/-2.1	3.6/-3.0	4.2/-3.8
Large-R jet JES (photon energy scale)	- / -	- / -	2.0/ -	2.2/ -	- / -
Large-R jet JES (topology)	8.0/-6.4	10.1/-6.9	10.8/-7.4	10.2/-7.8	8.5/-7.7
b-tagging b-jet efficiency	2.5/-2.3	2.2/ -	- / -	- / -	- / -
Luminosity	3.0/-3.0	3.0/-3.0	3.0/-3.0	3.0/-3.0	3.0/-3.0
Systematic	11.1/-9.0	12.7/-9.5	13.1/-10.2	12.8/-10.5	11.5/-10.6
Data statistics	±7	±7	±8	±7	±7
Total	13/-11	14/-12	15/-13	15/-13	14/-13

Table 5.16: Systematic uncertainties on the electron+jets unfolded spectrum at *particle level* in the fiducial phase space. Values below 2% are not shown.

PARTON LEVEL SPECTRUM - *el*+jets					
Uncertainty	-2.5 - -1.5	-1.5 - -0.5	-0.5 - 0.5	0.5 - 1.5	1.5 - 2.5
Large-R jet p_T resolution	2.4/-2.4	2.2/-2.2	- / -	- / -	- / -
Large-R jet mass scale	2.9/-3.1	2.9/-3.6	3.1/-3.9	3.4/-3.3	3.3/-2.4
Large-R jet JES (data vs MC)	3.2/ -	3.2/ -	3.1/-2.1	3.7/-3.1	4.4/-4.1
Large-R jet JES (topology)	7.0/-6.1	9.8/-6.8	10.8/-7.4	9.9/-7.8	7.7/-7.7
b-tagging b-jet efficiency	2.5/-2.4	2.3/ -	- / -	- / -	2.0/ -
Luminosity	3.0/-3.0	3.0/-3.0	3.0/-3.0	3.0/-3.0	3.0/-3.0
Systematic	10.5/-9.0	12.4/-9.4	13.2/-10.2	12.5/-10.4	11.0/-10.9
Data statistics	±8	±7	±9	±8	±9
Total	13/-12	14/-12	16/-13	15/-13	14/-14

Table 5.17: Systematic uncertainties on the electron+jets unfolded spectrum at *parton level* in the full phase space. Values below 2% are not shown.

PARTICLE LEVEL SPECTRUM - μ+jets					
Uncertainty	-2.5 - -1.5	-1.5 - -0.5	-0.5 - 0.5	0.5 - 1.5	1.5 - 2.5
Large-R jet p_T resolution	2.5/-2.5	- / -	- / -	- / -	2.7/-2.7
Large-R jet mass scale	3.0/-3.4	2.8/-2.7	2.6/-2.2	2.8/-2.1	3.5/-2.5
Large-R jet JES (data vs MC)	4.6/-3.6	3.3/-3.3	2.6/-3.2	3.3/-3.3	4.9/-3.2
Large-R jet JES (cut on subleading small-R jet)	- / -	- / -	- / -	- / -	2.2/ -
Large-R jet JES (photon energy scale)	2.2/-2.1	2.1/-2.1	- /-2.1	2.1/-2.1	2.7/ -
Large-R jet JES (correlation with JMS)	- / -	- / -	- / -	- / -	2.3/ -
Large-R jet JES (topology)	10.6/-7.4	9.4/-7.8	8.5/-8.2	8.9/-7.4	10.9/-6.1
Small-R jet energy resolution	2.6/-2.6	- / -	- / -	- / -	- / -
b-tagging b-jet efficiency	2.3/ -	2.5/-2.3	2.6/-2.4	2.4/-2.0	2.0/ -
μ trigger efficiency	- /-2.0	2.1/ -	2.2/ -	2.2/ -	2.3/ -
Luminosity	3.0/-3.0	3.0/-3.0	3.0/-3.0	3.0/-3.0	3.0/-3.0
Systematic	13.9/-11.3	12.0/-10.8	11.2/-11.0	12.1/-10.0	15.4/-9.2
Data statistics	±8	±8	±9	±8	±8
Total	16/-14	14/-13	14/-14	14/-13	17/-12

Table 5.18: Systematic uncertainties on the electron+jets unfolded spectrum at *particle level* in the fiducial phase space. Values below 2% are not shown.

PARTON LEVEL SPECTRUM - μ+jets					
Uncertainty	-2.5 - -1.5	-1.5 - -0.5	-0.5 - 0.5	0.5 - 1.5	1.5 - 2.5
Large-R jet p_T resolution	2.9/-2.9	- / -	- / -	- / -	3.2/-3.2
Large-R jet mass scale	2.9/-3.6	2.8/-2.7	2.6/-2.1	3.0/-2.1	3.8/-2.6
Large-R jet JES (data vs MC)	4.9/-3.8	3.4/-3.3	2.6/-3.2	3.5/-3.2	5.4/-3.1
Large-R jet JES (cut on subleading small-R jet)	- / -	- / -	- / -	- / -	2.6/ -
Large-R jet JES (photon energy scale)	2.2/-2.1	2.0/-2.1	- /-2.1	2.2/ -	3.0/ -
Large-R jet JES (generator)	- / -	- / -	- / -	- / -	2.2/ -
Large-R jet JES (correlation with JMS)	- / -	- / -	- / -	- / -	2.8/ -
Large-R jet JES (topology)	11.0/-7.5	9.5/-7.8	8.5/-8.1	9.3/-7.2	11.7/-5.6
Small-R jet energy resolution	3.3/-3.3	- / -	- / -	- / -	2.9/-2.9
b-tagging b-jet efficiency	2.2/ -	2.4/-2.3	2.6/-2.4	2.3/-2.0	- / -
μ trigger efficiency	- /-2.0	2.0/ -	2.1/ -	2.2/ -	2.4/ -
Luminosity	3.0/-3.0	3.0/-3.0	3.0/-3.0	3.0/-3.0	3.0/-3.0
Systematic	14.5/-11.8	12.0/-10.8	11.2/-10.9	12.6/-9.7	17.0/-9.4
Data statistics	$\pm$10	$\pm$8	$\pm$9	$\pm$8	$\pm$9
Total	18/-15	15/-14	15/-14	15/-13	19/-13

Table 5.19: Systematic uncertainties on the electron+jets unfolded spectrum at *parton level* in the full phase space. Values below 2% are not shown.

5.7.4 Combination of electron and muon channels

The results obtained in the e+jets and μ+jets channel are partially independent measurements on the same variables. To see the consistency of these measurements, a first estimate of the χ^2 has been calculated. The measurements have been treated as uncorrelated, considering only the statistical uncertainties and neglecting the systematic ones, since many of them are fully correlated.

With the measurements on $\frac{d\sigma}{dM_{t\bar{t}}}$, it has been calculated $\chi^2 = 6.23$ for *particle level* and $\chi^2 = 7.11$ for *parton level*, with 6 degree of freedom.

Regarding $\frac{d\sigma}{dp_{T,t\bar{t}}}$, it has been calculated $\chi^2 = 0.99$ for *particle* and *parton level*, with 6 degree of freedom.

For $\frac{d\sigma}{d\eta_{t\bar{t}}}$, it has been calculated $\chi^2 = 3.33$ for *particle level* and $\chi^2 = 3.47$ for *parton level*, with 5 degree of freedom.

These values of χ^2 suggest an overall consistency between the obtained distributions, and a combined ℓ+jets measurement has been performed in order to reduce the uncertainties. The samples are combined with a logical "OR" of the e+jets and μ+jets channel at the detector-level. Also to the Monte Carlo simulations are subjected to the same combined selection, with the proportions of e+jets and μ+jets events which take into account their respective efficiency. The data-driven backgrounds have been derived in each channel independently and then added to the combined simulated predictions. The uncertainties which are evaluated in the unfolding are based on the sum of the events, taking into account all correlations, calculating the effects related to only one channel only in their specific sub-sample (like the electron scale factors in the electron channel), while the common effects are calculated in the whole sample weighting appropriately the contribution coming from each channel.

Combined measurement of $\frac{d\sigma}{dM_{t\bar{t}}}$

The resulting spectra of the unfolded differential cross section with respect to the invariant mass of the $t\bar{t}$ system, compared with the with the predictions from *Powheg+Pythia*, *Powheg+Herwig* and *MC@NLO+Herwig*, are shown in Figure 5.19.

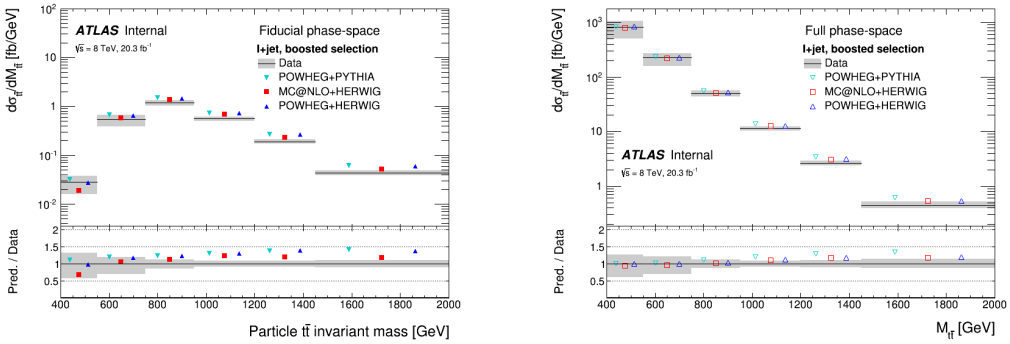

(a) Particle Level (b) Parton Level

Figure 5.19: Unfolded differential cross section for the $M_{t\bar{t}}$ spectrum calculated in the combined lepton+jets channel at (a)*particle level* in the fiducial phase space and (b) *parton level* in the full phase space. The shaded area correspons to the measured valus and the total uncertainty, while the coloured marks represent the MC predictions. In the lower part of the plots there is the ratio between the MC predictions and the measured values.

The results obtained combining the measurements in electron and muon channel can be seen in Table 5.20, while Tables 5.21 and 5.22 show the summary of the effects of the main systematic uncertainties at *particle* and *parton level*.

	Particle level			Parton level		
$M_{t\bar{t}}$[GeV]	$d\sigma_{t\bar{t}}/dM_{t\bar{t}}$[fb/GeV]	Stat. Unc.[%]	Total Unc.[%]	$d\sigma_{t\bar{t}}/dM_{t\bar{t}}$[fb/GeV]	Stat. Unc.[%]	Total Unc.[%]
400 - 550	0.031	±22	+43/-32	819.5	±10	+40/-27
550 - 750	0.65	±5	+29/-20	227.2	±5	+29/-21
750 - 950	1.40	±2	+14/-13	52.1	±3	+13/-12
950 - 1200	0.66	±3	+9/-9	12.3	±3	+8/-9
1200 - 1450	0.23	±3	+9/-10	2.90	±6	+11/-11
1450 - 2000	0.052	±5	+10/-12	0.494	±9	+13/-14

Table 5.20: The combined unfolded spectrum at *particle level* in the fiducial phase space and *parton level* in the full phase space.

PARTICLE LEVEL SPECTRUM - l+jets						
Uncertainity	400 - 550	550 - 750	750 - 950	950 - 1200	1200 - 1450	1450 - 2000
Large-R jet p_T resolution	5.9/-5.9	4.3/-4.3	- / -	- / -	- / -	- / -
Large-R jet $\sqrt{d_{12}}$ scale	2.2/ -	- / -	- / -	- / -	- / -	- / -
Large-R jet mass scale	- / -	- / -	2.7/-2.9	3.3/-3.5	3.3/-3.4	3.3/-3.4
Large-R jet JES (data vs MC)	10.6/-8.9	8.5/-7.4	4.5/-4.7	2.9/-3.1	3.1/-3.2	3.5/-3.8
Large-R jet JES (cut on subleading small-R jet)	3.4/ -	2.6/ -	- / -	- / -	- / -	- / -
Large-R jet JES (photon energy scale)	5.6/-3.1	4.4/-2.7	2.1/-2.0	- / -	- / -	- / -
Large-R jet JES (generator)	3.1/ -	2.5/ -	- / -	- / -	- / -	- / -
Large-R jet JES (statistics)	2.8/ -	2.2/ -	- / -	- / -	- / -	- /-2.1
Large-R jet JES (correlation with JMS)	4.0/-3.2	3.3/-2.8	- / -	- / -	- / -	- / -
Large-R jet JES (topology)	30.6/-18.7	24.0/-15.7	11.1/-9.5	4.1/-5.0	2.2/-3.2	- /-2.8
Large-R jet JES (pileup offset) μ	- /2.1	- / -	- / -	- / -	- / -	- / -
Small-R jet JES	7.9/-11.6	5.5/-7.8	-/-	-/-	-/-2.3	-/-3.4
b-tagging b-jet efficiency	- / -	- / -	- / -	2.8/-2.6	3.6/-3.5	4.1/-4.0
Luminosity	3.0/-3.0	3.0/-3.0	3.0/-3.0	3.0/-3.0	3.0/-3.0	3.0/-3.0
Systematic	37.0/-23.9	28.8/-19.7	13.5/-12.3	8.1/-9.0	8.4/-9.3	9.0/-10.4
Data statistics	±22	±5	±2	±3	±3	±5
Total	43/-32	29/-20	14/-13	9/-9	9/-10	10/-12

Table 5.21: Systematic uncertainties on the combined unfolded spectrum at *particle level* in the fiducial phase space. Values below 2% are not shown.

PARTON LEVEL SPECTRUM - l+jets						
Uncertainity	400 - 550	550 - 750	750 - 950	950 - 1200	1200 - 1450	1450 - 2000
Large-R jet p_T resolution	6.2/-6.2	4.4/-4.4	- / -	- / -	- / -	- / -
Large-R jet $\sqrt{d_{12}}$ scale	2.1/ -	- / -	- / -	- / -	- / -	- / -
Large-R jet mass scale	- / -	- / -	2.8/-3.0	3.4/-3.7	3.4/-3.5	3.4/-3.5
Large-R jet JES (data vs MC)	11.0/-9.4	8.6/-7.7	4.3/-4.6	2.5/-2.7	2.9/-3.0	3.5/-3.8
Large-R jet JES (cut on subleading small-R jet)	3.5/ -	2.7/ -	- / -	- / -	- / -	- / -
Large-R jet JES (photon energy scale)	5.8/-3.1	4.5/-2.8	- / -	- / -	- / -	- / -
Large-R jet JES (generator)	3.2/ -	2.5/ -	- / -	- / -	- / -	- / -
Large-R jet JES (definition of small-R jet inside large-R jet)	2.3/ -	- / -	- / -	- / -	- / -	- / -
Large-R jet JES (statistics)	2.9/ -	2.2/ -	- / -	- / -	- / -	- /-2.4
Large-R jet JES (correlation with JMS)	4.2/-3.3	3.4/-2.8	- / -	- / -	- / -	- / -
Large-R jet JES (topology)	31.5/-19.7	24.2/-16.2	10.3/-9.4	2.7/-4.1	- /-2.1	- / -
Large-R jet JES (pileup offset) μ	- /2.2	- / -	- / -	- / -	- / -	- / -
Small-R jet JES	8.5/-12.0	6.0/-7.9	-/-	-/-	2.0/-3.6	2.0/-4.1
b-tagging b-jet efficiency	- / -	- / -	- / -	2.9/-2.7	3.9/-3.9	4.5/-4.5
e energy scale	- / -	- / -	- / -	- / -	- / -	-2.3/ -
Luminosity	3.0/-3.0	3.0/-3.0	3.0/-3.0	3.0/-3.0	3.0/-3.0	3.0/-3.0
Systematic	38.2/-25.0	29.1/-20.3	12.7/-12.1	7.6/-8.8	8.6/-9.7	9.5/-11.2
Data statistics	±10	±5	±3 ±3	±60	±9	
Total	40/-27	29/-21	13/-12	8/-9	11/-11	13/-14

Table 5.22: Systematic uncertainties on the combined unfolded spectrum at *parton level* in the full phase space. Values below 2% are not shown.

Combined measurement of $\frac{d\sigma}{dp_{T,t\bar{t}}}$

The resulting spectra of the unfolded differential cross section with respect to the transverse momentum of the $t\bar{t}$ system, compared with the with the predictions from *Powheg+Pythia*, *Powheg+Herwig* and *MC@NLO+Herwig*, are shown in Figure 5.20.

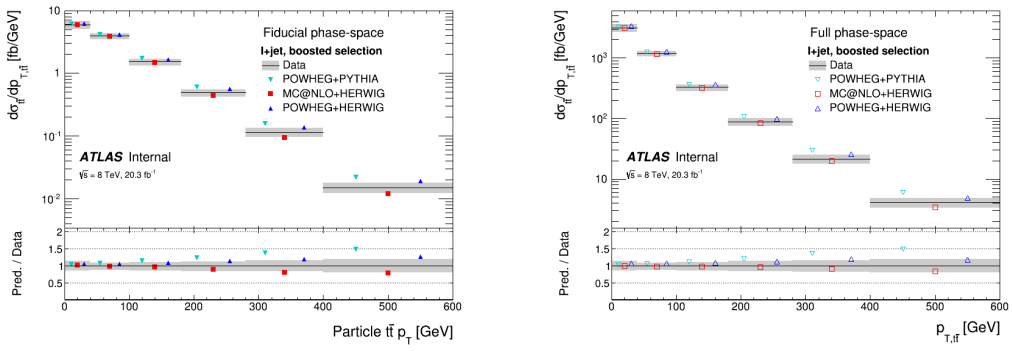

(a) Particle Level (b) Parton Level

Figure 5.20: Unfolded differential cross section for the $p_{T,t\bar{t}}$ spectrum calculated in the combined lepton+jets channel at (a)*particle level* in the fiducial phase space and (b) *parton level* in the full phase space. The shaded area correspons to the measured valus and the total uncertainty, while the coloured marks represent the MC predictions. In the lower part of the plots there is the ratio between the MC predictions and the measured values.

The results obtained combining the measurements in electron and muon channel can be seen in Table 5.23, while Tables 5.24 and 5.25 show the summary of the effects of the main systematic uncertainties at *particle* and *parton level*.

	Particle level			Parton level		
$p_{T,t\bar{t}}$[GeV]	$d\sigma_{t\bar{t}}/dp_{T,t\bar{t}}$[fb/GeV]	Stat. Unc.[%]	Total Unc.[%]	$d\sigma_{t\bar{t}}/dp_{T,t\bar{t}}$[fb/GeV]	Stat. Unc.[%]	Total Unc.[%]
0 - 40	5.87	±3	+13/-15	3113.0	±3	+13/-15
40 - 100	3.92	±2	+12/-10	1188.4	±3	+12/-10
100 - 180	1.53	±3	+14/-11	328.0	±4	+14/-11
180 - 280	0.49	±4	+15/-13	88.3	±6	+15/-14
280 - 400	0.12	±8	+16/-16	21.4	±8	+17/-16
400 - 600	0.015	±13	+19/-19	4.05	±12	+19/-19

Table 5.23: The combined unfolded spectrum at *particle level* in the fiducial phase space and *parton level* in the full phase space.

PARTICLE LEVEL SPECTRUM - l+jets						
Uncertainty	0 - 40	40 - 100	100 - 180	180 - 280	280 - 400	400 - 600
Large-R jet p_T resolution	- / -	- / -	2.6/-2.6	2.1/-2.1	- / -	- / -
Large-R jet mass scale	2.6/-2.9	3.0/-2.9	3.2/-2.9	2.9/-2.7	2.5/-2.6	2.3/-2.6
Large-R jet JES (data vs MC)	4.4/-5.6	3.7/-3.2	4.6/-4.0	5.9/-5.6	6.5/-6.4	6.8/-6.6
Large-R jet JES (photon energy scale)	2.1/-2.5	- / -	- / -	2.3/-2.1	2.7/-2.7	2.8/-3.1
Large-R jet JES (statistics)	- / -	- / -	- / -	2.1/ -	2.8/-2.4	3.1/-2.8
Large-R jet JES (correlation with JMS)	2.1/-2.3	- / -	- / -	2.6/-2.2	2.9/-2.7	3.0/-3.0
Large-R jet JES (topology)	9.7/-10.3	9.0/-6.8	9.8/-7.0	9.9/-8.1	9.1/-8.3	8.5/-8.2
Small-R jet JES	3.3/-	-/-	-/-	-/-2.1	-/-3.8	2.3/-4.7
Small-R jet energy resolution	-2.1/2.1	- / -	- / -	- / -	2.1/-2.1	2.5/-2.5
b-tagging b-jet efficiency	2.2/ -	2.3/-2.0	2.4/-2.1	2.4/-2.2	2.5/-2.2	2.6/-2.3
Luminosity	3.0/-3.0	3.0/-3.0	3.0/-3.0	3.0/-3.0	3.0/-3.0	3.0/-3.0
Systematic	13.1/-14.4	11.6/-9.5	13.3/-10.6	14.3/-12.6	14.4/-13.9	14.3/-14.6
Data statistics	±3	±2	±3	±4	±8	±13
Total	13/-15	12/-10	14/-11	15/-13	16/-16	19/-19

Table 5.24: Systematic uncertainties on the combined unfolded spectrum at *particle level* in the fiducial phase space. Values below 2% are not shown.

PARTON LEVEL SPECTRUM - l+jets						
Uncertainty	0 - 40	40 - 100	100 - 180	180 - 280	280 - 400	400 - 600
Large-R jet p_T resolution	- / -	- / -	2.8/-2.8	2.4/-2.4	- / -	- / -
Large-R jet mass scale	2.5/-2.9	3.0/-2.9	3.3/-2.9	3.0/-2.7	2.6/-2.6	2.2/-2.5
Large-R jet JES (data vs MC)	4.3/-5.6	3.5/-3.1	4.4/-3.7	5.8/-5.5	6.6/-6.5	6.9/-6.8
Large-R jet JES (photon energy scale)	2.1/-2.5	- / -	- / -	2.2/ -	2.7/-2.8	2.9/-3.2
Large-R jet JES (statistics)	- / -	- / -	- / -	- / -	2.9/-2.4	3.2/-2.9
Large-R jet JES (correlation with JMS)	2.0/-2.4	- / -	- / -	2.5/-2.1	2.9/-2.7	3.0/-3.1
Large-R jet JES (topology)	9.6/-10.4	9.0/-6.8	9.9/-6.8	10.2/-8.1	9.3/-8.5	8.5/-8.4
Small-R jet JES	4.2/-2.2	-/-	-/-	-/-	-/-3.1	2.3/-4.7
Small-R jet energy resolution	-2.4/2.4	- / -	- / -	- / -	- / -	2.4/-2.4
b-tagging b-jet efficiency	2.2/ -	2.3/-2.0	2.3/-2.0	2.4/-2.1	2.5/-2.2	2.6/-2.3
E_T^{miss} unassociated cells scale	-2.2/ -	- / -	- / -	- / -	- / -	- / -
Luminosity	3.0/-3.0	3.0/-3.0	3.0/-3.0	3.0/-3.0	3.0/-3.0	3.0/-3.0
Systematic	13.1/-14.8	11.5/-9.4	13.3/-10.3	14.4/-12.4	14.5/-13.9	14.4/-14.8
Data statistics	±3	±3	±4	±6	±8	±12
Total	13/-15	12/-10	14/-11	15/-14	17/-16	19/-19

Table 5.25: Systematic uncertainties on the combined unfolded spectrum at *parton level* in the full phase space. Values below 2% are not shown.

Combined measurement of $\frac{d\sigma}{d\eta_{t\bar{t}}}$

The resulting spectra of the unfolded differential cross section with respect to the pseudorapidity of the $t\bar{t}$ system, compared with the with the predictions from *Powheg+Pythia*, *Powheg+Herwig* and *MC@NLO+Herwig*, are shown in Figure 5.21.

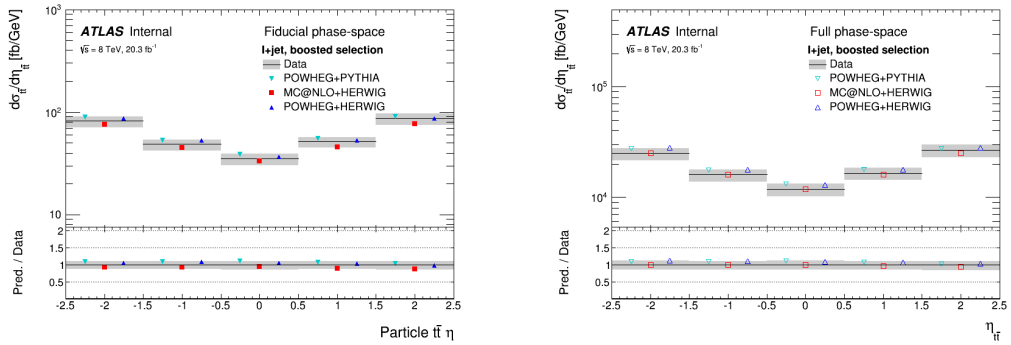

(a) Particle Level (b) Parton Level

Figure 5.21: Unfolded differential cross section for the $\eta_{t\bar{t}}$ spectrum calculated in the combined lepton+jets channel at (a)*particle level* in the fiducial phase space and (b) *parton level* in the full phase space. The shaded area correspons to the measured valus and the total uncertainty, while the coloured marks represent the MC predictions. In the lower part of the plots there is the ratio between the MC predictions and the measured values.

The results obtained combining the measurements in electron and muon channel can be seen in Table 5.26, while Tables 5.27 and 5.28 show the summary of the effects of the main systematic uncertainties at *particle* and *parton level*.

	Particle level			Parton level		
$\eta_{t\bar{t}}$	$d\sigma_{t\bar{t}}/d\eta_{t\bar{t}}$[fb]	Stat. Unc.[%]	Total Unc.[%]	$d\sigma_{t\bar{t}}/d\eta_{t\bar{t}}$[fb]	Stat. Unc.[%]	Total Unc.[%]
-2.5 - -1.5	81.64	±4	+13/-11	24958.3	±7	+14/-12
-1.5 - -0.5	48.54	±4	+13/-11	16005.2	±6	+13/-11
-0.5 - 0.5	34.93	±5	+13/-12	11822.0	±6	+14/-12
0.5 - 1.5	51.40	±4	+13/-11	16541.8	±6	+14/-11
1.5 - 2.5	87.25	±4	+14/-11	26785.5	±6	+15/-11

Table 5.26: The combined unfolded spectrum at *particle level* in the fiducial phase space and *parton level* in the full phase space.

PARTICLE LEVEL SPECTRUM - l+jets					
Uncertainty	-2.5 - -1.5	-1.5 - -0.5	-0.5 - 0.5	0.5 - 1.5	1.5 - 2.5
Large-R jet p_T resolution	2.5/-2.5	- / -	- / -	- / -	- / -
Large-R jet mass scale	2.9/-3.3	2.9/-3.2	2.9/-3.1	3.2/-2.8	3.5/-2.6
Large-R jet JES (data vs MC)	3.9/-2.7	3.3/-2.5	2.8/-2.6	3.5/-3.1	4.5/-3.5
Large-R jet JES (photon energy scale)	- / -	2.0/ -	2.0/ -	2.2/ -	2.2/ -
Large-R jet JES (topology)	9.2/-6.9	9.8/-7.3	9.8/-7.7	9.7/-7.6	9.7/-7.0
b-tagging b-jet efficiency	2.4/-2.1	2.3/-2.1	2.2/ -	- / -	- / -
Luminosity	3.0/-3.0	3.0/-3.0	3.0/-3.0	3.0/-3.0	3.0/-3.0
Systematic	12.1/-9.8	12.3/-9.9	12.1/-10.3	12.3/-10.1	13.1/-9.7
Data statistics	±4	±4	±5	±4	±4
Total	13/-11	13/-11	13/-12	13/-11	14/-11

Table 5.27: Systematic uncertainties on the combined unfolded spectrum at *particle level* in the fiducial phase space. Values below 2% are not shown.

PARTON LEVEL SPECTRUM - l+jets					
Uncertainty	-2.5 - -1.5	-1.5 - -0.5	-0.5 - 0.5	0.5 - 1.5	1.5 - 2.5
Large-R jet p_T resolution	2.7/-2.7	- / -	- / -	- / -	2.1/-2.1
Large-R jet mass scale	2.9/-3.3	2.8/-3.2	2.9/-3.1	3.2/-2.8	3.6/-2.5
Large-R jet JES (data vs MC)	4.0/-2.8	3.3/-2.5	2.9/-2.6	3.7/-3.2	4.9/-3.6
Large-R jet JES (photon energy scale)	- / -	- / -	2.1/ -	2.2/ -	2.2/ -
Large-R jet JES (correlation with JMS)	- / -	- / -	- / -	- / -	2.2/ -
Large-R jet JES (topology)	8.8/-6.8	9.7/-7.3	9.9/-7.7	9.8/-7.5	9.6/-6.7
b-tagging b-jet efficiency	2.4/-2.0	2.3/-2.1	2.2/ -	2.0/ -	- / -
Luminosity	3.0/-3.0	3.0/-3.0	3.0/-3.0	3.0/-3.0	3.0/-3.0
Systematic	12.0/-9.8	12.2/-9.9	12.2/-10.3	12.5/-9.9	13.5/-9.6
Data statistics	±7	±6	±6	±6	±6
Total	14/-12	13/-11	14/-12	14/-11	15/-11

Table 5.28: Systematic uncertainties on the combined unfolded spectrum at *parton level* in the full phase space. Values below 2% are not shown.

Combined measurement of $\sigma_{t\bar{t}}^{fiducial}$

As a check, the ℓ+jets combined data sample has been used to calculate the total $t\bar{t}$ production cross section at *particle level*, defined in a fiducial region which follow closely the detector-level event selection.

The measured fiducial $t\bar{t}$ production cross section, for boosted top quarks with $p_T > 300$ GeV from pp collisions at $\sqrt{s} = 8$ TeV, is

$$\sigma_{t\bar{t}}^{fiducial} = 660^{+70}_{-90} \text{ fb}.$$

This value is compatible with the predictions of the same measurement obtained with the tested Monte Carlo generators, which have a theoretical relative uncertainty of the order of 15% [41]:

$$\sigma_{t\bar{t}}^{Powheg+Pythia} = 720 \text{ fb}, \qquad \sigma_{t\bar{t}}^{MC@NLO} = 640 \text{ fb}, \qquad \sigma_{t\bar{t}}^{Powheg+Herwig} = 700 \text{ fb}.$$

Conclusions

The aim of this analysis was to perform the measurement of the boosted top pair production differential cross section, with respect to the mass, the transverse momentum and the pseudorapidity of the $t\bar{t}$ system, which are three important kinematical variables.

The analysis has been done both on real data and on Monte Carlo simulations, concentrating on the single lepton decay channel, because it is the best compromise in terms of statistics and signal-to-background ratio. The real data come from proton-proton collisions made at LHC at $\sqrt{s} = 8$ TeV and collected by the ATLAS detector during the 2012, corresponding to an integrated luminosity of $\mathcal{L} \sim 20$ fb^{-1}.

In order to evaluate the detector acceptance and efficiencies detailed Monte Carlo simulations have been performed. To understand part of the measurement systematics related to th simulations, several different generators have been used in the Monte Carlo event generation, hadronization and showering steps. The $t\bar{t}$ processes have been simulated using *Powheg* for the hard scattering and using *Pythia* for the parton showers and the hadronizations. The single top events have been generated using *AcerMC* for the t-channel and *Powheg* for the s-channel and the Wt production, interfaced with *Pythia* to make the parton showering in both cases. The W+jets and Z+jets background processes have been simulated using *AlpGen* interfaced with the *Pythia* generator for the parton showering, while the *diboson* processes have been generated with *Sherpa*. The QCD multijet background processes as well as the overall normalization for the W+jets, which are the most

relevant backgrounds, have been estimated using data-driven techniques.

In order to isolate the signal and reject the background processes, a cut based analysis has been performed. The events have been selected to have one isolated lepton with high transverse momentum, missing transverse energy due to the presence of the neutrino, constraints on the transverse mass of the reconstructed leptonic W in order to reject the QCD multijet background, at least one jet with a cone of $\Delta R \leq 0.4$ close to the lepton and at least one large R jet ($\Delta R \leq 1$) spatially separated from the lepton, containing the hadronically decaying top decay products. At least one of the jets of the event has to be compatible with the presence of a bottom quark. The data sample obtained applying all the cuts consists of 4145 events in the e+jets channel and 3603 events in the μ+jets channel.

Once the events have been selected with such criteria, the $t\bar{t}$ system is reconstructed making the vectorial sum of the four-momenta of the hadronically decaying and the leptonically decaying top. The former is chosen as the large R jet with the highest transverse momentum, while the latter is reconstructed making a vectorial sum of the four-momenta of the the lepton, the jet with the highest transverse momentum and the neutrino, whose components are estimated from the missing transverse energy and the lepton with a quadratic equation, using as constraint the W boson pole mass $M_W = 80.4$ GeV.

The differential distributions of the reconstructed variables are affected by the resolution of the measurements, the acceptance of the detector and the efficiency of the selection. Unfolding techniques have been used in order to remove such effects so that the unfolded differential distributions can be directly compared with the results of different experiments and with the theoretical predictions. The resolution of the measurements are considered in the *migration matrix*, which link the true distribution of a certain physical variable to the reconstructed one. The unfolding procedure consists in estimating the true distribution of the variable from its reconstructed distribution by inverting the *migration matrix*. The unfolding method which

has been used is the Singular Value Decomposition with the addition of a regularization phase of the solution.

The unfolded differential distributions of the mass, the transverse momentum and the pseudorapidity of the $t\bar{t}$ system have been evaluated for the e+jets channel and μ+jets channel, obtaining consistent measurements, leading to a combined measurement of the boosted $t\bar{t}$ production differential cross section at *particle level*, in a fiducial phase space defined by the event selection ($p_{T,t} > 300$ GeV), and at *parton level* in the full phase space.

The invariant mass of the $t\bar{t}$ system has been studied in the range from 400 to 2000 GeV, while for the transverse momentum the range is from 0 to 600 GeV and for the pseudorapidity the range is from -2.5 to 2.5. The binning of every distribution is variable, choosing the width of every bin in order to have a lower statistical uncertainty with respect to the total systematic uncertainty.

The total measurement uncertainty ranges from 8% to 43% in the case of the invariant mass of the $t\bar{t}$ system, from 10% to 19% in the case of the transverse momentum and from 11% to 15% in the case of the pseudorapidity. A detailed analysis of the sources of systematic uncertainties has been performed and the Jet Energy Scale for large R jets is the dominant one, especially the one linked to the topology, which affects the measurements with an average uncertainty of $\sim 10\%$ in every bin of the studied distributions, with the exception of the invariant mass in the range 400 GeV $< M_{t\bar{t}} <$ 550 GeV, where it reaches a value of $\sim 31\%$.

The measured boosted $t\bar{t}$ differential cross sections have been compared with the predictions obtained using three NLO Monte Carlo generators, normalized to the NNLO+NNLL inclusive cross section $\sigma_{t\bar{t}} = 253^{+13}_{-15}$ pb: *Powheg* interfaced with *Pythia* for the parton showers and the hadronizations, and *MC@NLO* and *Powheg* interfaced with *Herwig*.

Both at *particle level* and *parton level* it is possible to see a general tendency of the theoretical prediction to overestimate the data distribution, especially for the higher values of mass and transverse momentum of the $t\bar{t}$

system. In particular, the fiducial $t\bar{t}$ cross section at *particle level* in the highest-$M_{t\bar{t}}$ bin (1450 GeV $< M_{t\bar{t}} <$ 2000 GeV) is overestimated by approximately 40% by *Powheg+Pythia*, 30% by *Powheg+Herwig* and 13% by *MC@NLO*, while in the highest-p_T bin (400 GeV $< p_T <$ 600 GeV) is overestimated by 50% by *Powheg+Pythia* and 30% by *Powheg+Herwig*. The same trend has been observed in other differential cross section analysis [41]. However, the measurements are still compatible with the Monte Carlo predictions within their experimental uncertainties.

With the selected data sample a total boosted $t\bar{t}$ production cross section in the fiducial region defined by the event selection ($p_{T,t} >$ 300 GeV) has been measured

$$\sigma_{t\bar{t}}^{fiducial} = 660^{+70}_{-90} \text{ fb},$$

which is compatible with the predictions obtained with the tested Monte Carlo generators, which have a theoretical relative uncertainty of the order of 15%:

$$\sigma_{t\bar{t}}^{Powheg+Pythia} = 720 \text{ fb}, \qquad \sigma_{t\bar{t}}^{MC@NLO} = 640 \text{ fb}, \qquad \sigma_{t\bar{t}}^{Powheg+Herwig} = 700 \text{ fb}.$$

In summary, being the first measurement of boosted $t\bar{t}$ production differential cross section with respect to the kinematical variables of the $t\bar{t}$ system performed with the data collected by ATLAS, this analysis can be considered a step forward towards a better knowledge of the top quark production in the boosted regime, with an overall confirmation of the Standard Model theoretical predictions, and gives a relevant contribution in the description of the $t\bar{t}$ background processes in the searches for Beyond Standard Model resonances with the invariant mass in the TeV region.

Appendix 1: RIVET routine to calculate fiducial differential cross section

RIVET

Monte Carlo event generators can be tested against experimental results using the RIVET [105] (Robust Independent Validation of Experiment and Theory) framework, which provides routines that replicate many experimental analyses and can be easily used for MC generator development, validation and tuning. So, RIVET allows to preserve the analysis code used in several measurements for an easy comparison with future theoretical models that can be developed.

RIVET is designed to work with *HepMC* records[61], independently on the generator which has been used to produce them. In particular, RIVET uses all stable and semi-stable particles from simulation to obtain the results at *particle level*. All the physical observables are evaluated using a computationally efficient mechanism based on *projections*, in order to avoid any re-calculation of common quantities. Indeed, these *projections* are in a framework which records automatically their value among the events, making RIVET really scalable with the number of particles and events. In this framework, if two analyses have the same run conditions, like the incoming beam types and energies, for every event that is read by RIVET all the use-

ful *projection*'s values obtained in one analysis are stored in a *cache* memory and used to replace equivalent calculations in the other analyses. Each *projection* has a comparison operator in order to decide if the cached results are acceptable or if it is necessary to perform the calculation again with different settings.

Since RIVET is one of the most used framework by phenomenologists, a RIVET routine to reproduce the boosted $t\bar{t}$ fiducial differential cross section measurement is developed to allow Monte Carlo developers and experimentalists working on the tuning of generators to easily compare Monte Carlo simulations with the measurement at *particle level*.

Cutflow at particle level

The fiducial boosted $t\bar{t}$ fiducial differential cross section at *particle level* is measured through a cut based analysis, where the selection is done following the event selection at reconstruction level, so requiring:

- There must be only one good electron (or muon). A good lepton is dressed with the photons within a radius of $\Delta R < 0.1$ from it (where $\Delta R = \sqrt{\Delta\eta^2 + \Delta\phi^2}$), and must have a p_T greater than 25 GeV and $|\eta| < 2.5$.
- The missing transverse energy must be larger than 20 GeV.
- The sum $M_T^W + E_T^{miss}$ must be larger than 60 GeV (where $M_T^W = \sqrt{2p_T^l p_T^\nu \left(1 - \cos\left(\phi^l - \phi^\nu\right)\right)}$).
- There must be at least one good jet (*anti-kt.4*) within a radius $\Delta R < 1.5$ from the lepton.
- There must be at least one good large R jet ($R = 1$) spatially isolated from the lepton ($\Delta R > 1.5$ and $\Delta\phi > 2.3$). In order to discriminate the signal from the QCD background, these large-R jets have to satisfy selection criteria on mass transverse momentum and splitting scale

($m \geq 100$ GeV, $p_T \geq 300$ GeV, $\sqrt{d_{12}} \geq 40$ GeV), and a trimming algorithm is applied.

- There must be at least one b-tagged *anti-kt.4* jet, namely a jet within which a b hadron has been identified. The tagged jet can be the jet of the leptonic top itself, a b-jet inside the large-R jet, or both.

Implementation and validation of the RIVET routine

The implementation of the *particle level* selection in a RIVET routine has been done through the available *projections* of the framework, using a *projection* for every kind of particle.

The leptons have been selected looking for the projections of dressed leptons (whose four-momentum has been determined summing the four-momenta of every photon inside a cone of $\Delta R = 0.1$ around the leptons) with a transverse momentum larger than 25 GeV, and with $|\eta| < 2.5$. The leptons coming from decays of τ have been considered signal, while the ones coming from the decays of hadrons have been discarded as background.

The missing transverse energy has been determined as the transverse momentum of the vectorial sum of the four-momenta of all the neutrino projections in the event with $|\eta| < 4.5$.

The jets are clustered using the FastJet package [106], using the *anti-kt* algorithm with radius $\Delta R \leq 0.4$ applied to all the final state particles in the event, with the exception of the dressed leptons.

The large R jets are clustered and trimmed with the FastJet package, using the *anti-kt* algorithm with cone $\Delta R \leq 1$ applied to all the final state particles in the event except the dressed leptons, and requiring a mass of the jet of $m \geq 100$ GeV, a transverse momentum of $p_T \geq 300$ GeV and a splitting scale of $\sqrt{d_{12}} \geq 40$ GeV.

The b tagging is done asking whether among the constituents of a jet

there is an hadron which contains b quark and has a transverse momentm greater than 5 GeV.

RIVET uses *HepMC* format for input files (corresponding to the ATLAS *EVNT* files used in the *Athena* framework[107]), while ATLAS analyses use files in the *NTUP_COMMON* ATLAS format, which is obtained after the detector simulation made by Geant4[76] and the whole process of reconstruction of the events. Because of the peculiarities of the reconstruction processes, even if the *NTUP_COMMON* files are produced using the *EVNT* files, there are no variables which identify the events through the different formats.

Two parallel strategies have been followed for the validation of the RIVET routine. A first control was made using a sample of *EVNT* and comparing the population of the events which survived the cuts of the selection with the results obtained by the analysis using a sample of *NTUP_COMMON* events. The effects of the cuts where compared by calculating the relative efficiencies C_n/C_{n-1} and their statistical uncertainties, where C_n is the population of the events which survived after the application of the cut number n.

Through this check it has been possible to correct the discrimination of the signal leptons from the background, avoiding the leptons coming from a decaying hadron. An additional subtle effect involving leptons coming from τ decays remained unnoticed with this procedure.

In parallel, a new sample of *NTUP_COMMON* files has been produced without losing any event from a sample of 40000 *EVNT* (divided in eight subsamples of 5000 events each), in order to make more precise checks. Indeed, in this case the surviving population of every cut C_n should have been exactly the same in RIVET and in the analysis.

Through this check it has been possible to correct the determination of the missing energy, calculated as the sum of the neutrinos.

In order to have the exact replica of the missing energy calculated by the analysis, the description of the lepton coming from tau decays has been improved, using only prompt taus, as it was possible with the newest versions

of RIVET (2.2.1 and newer).

Finally, a comparison of the *NTUP_COMMON* sample with the EVNT sample on an event-by-event basis has been made, comparing the values of p_T, η and ϕ of the leptons and of the most energetic jets and finding the events with the same values in the two samples. In this way it has been possible to solve the last discrepancies between the cutflow obtained by the Rivet routine and the one of the analysis, linked to slight differences in the definitions of muons and jet among the two frameworks.

After the debugging of the routine, the cutflows obtained by RIVET and the analysis framework are exactly the same, corresponding to the one shown in Table 5.29

Cut	Electron Channel	Muon Channel
C0. Number of events	40000	40000
C1. At least one electron (muon)	11876	11953
C2. Only one electron (muon)	11393	11409
C3. Absence of muons (electrons)	10299	10315
C4. $E_T^{miss} > 20$ GeV	9189	9236
C5. $E_T^{miss} + M_T^W > 60$ GeV	8730	8734
C6. At least one good jet	5221	5196
C7. At least one large-R jet	90	112
C8. At least one b-tagged jet	87	108
C8.1. Both the jets are b-tagged	62	89
C8.2. The b-tagged jet is in the large-R jet	18	13
C8.3. The good jet is b-tagged	7	6

Table 5.29: The cutflow obtained by the RIVET routine and by the analysis framework

Results

Once the RIVET routine has been successfully validated, it has been possible to extract the p_T distributions of the hadronically decaying top, corresponding to the large R jet with the highest p_T in the selected events.

With these distribution, the boosted $t\bar{t}$ fiducial cross section with respect to the p_T of the hadronic top can be calculated scaling the population of every bin by the integrated luminosity of the sample, obtained as the ratio between the number of events and the total cross section. The resulting differential cross section is shown in Figure 5.22.

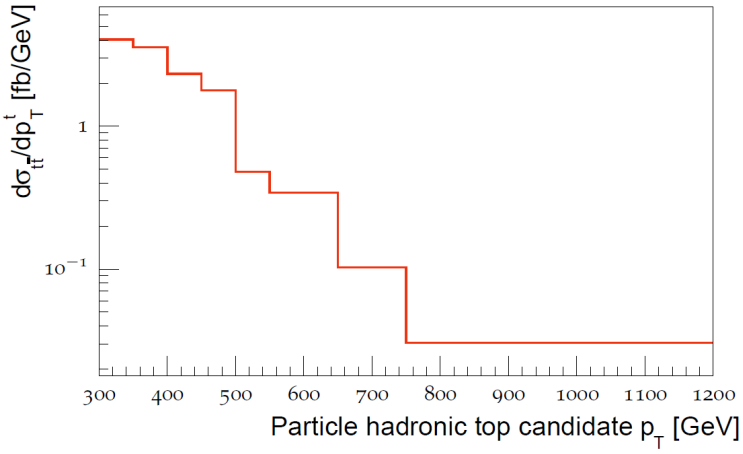

Figure 5.22: The fiducial $t\bar{t}$ differential cross section with respect to the hadronic top p_T calculated with RIVET.

Conclusions and comments

The resulting spectra of the p_T of the hadronic top and the $t\bar{t}$ differential cross section obtained with RIVET is in reasonable agreement with the results at *particle level* published by ATLAS [41].

However, there is a difference between the selection of the sample made in the analysis, and the one made by the RIVET routine. The analysis

selects the phase space with filter at *parton level* which removes the dileptonic events from the Monte Carlo sample, composed both all $t\bar{t}$ events which are not full hadronic. It is not possible to apply this kind of partonic filter in RIVET, which works at *particle level* and is not able to appreciate controls at *parton level*. In order to evaluate how the absence of this filter influences the selection, a control on the cutflow obtained with RIVET is done, looking for the leptons that are present in the events without asking fiducial cuts. In the electron channel 11393 events with only one electron pass the fiducial cuts, and 483 of them has more than one electron without considering the fiducial cuts. In the muon channel 11409 events with only one muon pass the fiducial cuts and 527 of them has more than one electron without considering the fiducial cuts. Hence, about 4% of the events with only one lepton that pass fiducial cuts have at least another lepton which doesn't pass this cuts, and could be dileptonic.

This strategy is compatible with the RIVET recommendations. Replacing the *parton level* cut with the described selection has a negligible impact on the final result, therefore this strategy will be followed in the implementation of the RIVET routine. The routine is now ready to be reviewed by the RIVET authors for the integration in the next RIVET release.

Appendix 2: BIS78 upgrade of the ATLAS muon trigger

High rate in transition region and proposed upgrade

As said in the previous chapters, the ATLAS trigger system is divided into an hardware based level (L1) and a software based higher-level trigger (HLT), reducing the rate from 40 MHz to about 200 Hz. The Level 1 muon is based on RPC and TGC hits which define the Regions of Interest (ROI) that will be used as seeds for the HLT.

Many upgrades are planned at the LHC in the coming years: in 2021 the so called Run-3 will start, characterized by a center-of-mass energy of $\sqrt{s} = 13 \sim 14$ TeV, an instantaneous luminosity up to $L = 3 \cdot 10^{34}$ cm^{-2} s^{-1} and 25 ns of bunch crossing interval. The luminosity is scheduled to rise further in 2026 during the Run-4, reaching a value of about $L =\sim 7.5 \cdot 10^{34}$ cm^{-2} s^{-1}. The trigger and tracking systems of the muon spectrometer will be upgraded to perform well in the new conditions.

Indeed, considering that during the Run-1 the total rate of the Level-1 single muon trigger (with transverse momentum $p_T > 20$ GeV) is 6 kHz with a luminosity of $L = 0.7 \cdot 10^{34}$ cm^{-2} s^{-1} and 50 ns of bunch crossing interval, with a linear extrapolation that takes account the differences between Run-1 and Run-3 in terms of luminosity ($f_L = 3/0.7$), W and Z cross sections ($f_\sigma \sim 1.6$) and bunch spacing ($f_{BS} = 1.4$, considering the 40% higher rate

measured in the 25 ns bunch spacing runs of 2011) it can be estimated that it will rise up to 57.6 kHz, if no measures are taken, while ATLAS can allocate only 25 kHz for muon triggers out of a total Level-1 bandwidth of 100 kHz [108]. In Figure 5.23 it is possible to see this estimation as a function of p_T threshold.

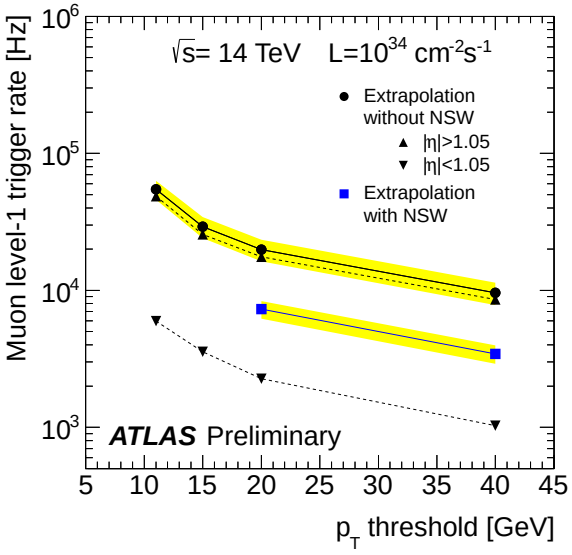

Figure 5.23: Estimation of the contributions to ATLAS muon level-1 trigger rate from the Barrel and the End Caps, extrapolated for pp collisions at $\sqrt{s} = 14$ TeV with instantaneous luminosity of $L \sim 10^{34}$ cm^{-2} s^{-1}, shown as a function of p_T threshold. [109].

Figure 5.24 shows the η distribution of the ROIs of the Level-1 single muon trigger [110].There is great abundance of ROIs in the $|\eta| > 1$ region, while the population of the ROIs associate to reconstructed muons (which are drawn in darker blue) is almost flat. Hence, most of activated ROIs are background, mainly low-p_T protons generated in toroids and shieldings of the spectrometer.

In order to face this expected higher rate, the inner layer of the End Cap will be replaced with the New Small Wheel (NSW) [110], reducing the fake triggers in the $|\eta| > 1.3$ region. An estimation of its effects in the trigger

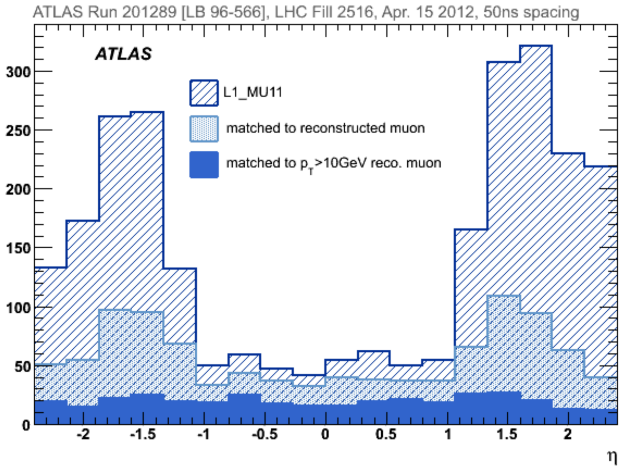

Figure 5.24: η distribution of Level-1 muon ROIs ($p_T > 10$ GeV) with the distribution of the subset matched to an offline reconstructed muon with $p_T > 3$ GeV or $p_T > 10$ GeV [110].

rate can be seen in Figure 5.23.

Unfortunately, there is still a remaining high rate in the transition region between Barrel and End Cap ($1.0 < |\eta| < 1.3$): in runs of 25 ns of bunch crossing interval, almost 21.9% of the activated ROIs are concentrated in this region, which lead to a rate of about 12.6 kHz at $\sqrt{s} = 13$ TeV and $L = 3 \cdot 10^{34}$ cm^{-2} s^{-1}, considering the estimated total rate of 57.6 kHz.

In 2015 another upgrade of the muon trigger has been approved in order to reduce the fake trigger in transition region: the BIS78 project. The project consists in requiring a coincidence between the End Cap trigger and the passage through an inner plane, which can be different depending on the angular coordinates. Indeed, the Barrel of the Muon Spetrometer is divided into 16 sectors in azimuthal angle ϕ, divided into large and small sectors, where the latter contain the coils of the toroidal magnetic field.

The required plane will be covered by the New Small Wheel in the $|\eta| > 1.3$ region, while concerning the the outer part of the large sectors the required inner plane will be covered by the TGCs in the inner layer of

the End Cap (EIL4-5, which can be seen in Figure 5.25, left). Regarding the small sectors new RPCs will be added to BIS 7-8 chambers, which are the inner Barrel MDT chambers that cover the transition region (figure 5.25, right).

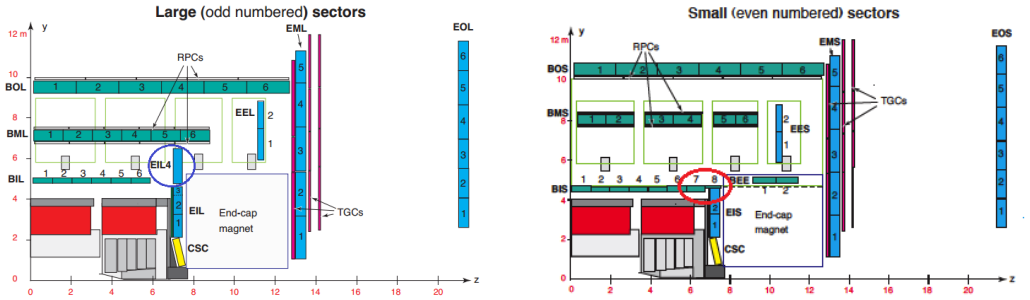

Figure 5.25: On the left: the large sectors of the End Cap of the ATLAS muon spectrometer. The blue circle highlights the EIL4-5 chambers, the TGCs which will be used as an inner plane for the trigger. On the right: the small sectors of the Barrel of the ATLAS muon spectrometer. The red circle highlights the BIS7-8 chambers, where the RPCs are proposed to be added.

Performance studies

In order to evaluate the performance of the proposed upgrade, an analysis has been made using 2012 data, emulating the RPC hits on the proposed chambers using MDT track segments after the request of the End Cap trigger. The study has been done using two samples. One sample was made of standard runs with 50ns of bunch crossing interval, with muons selected by the HLT, which has been used to estimate the efficiency of the proposed trigger. The other sample was made of special "enhanced bias" runs with 25ns of bunch crossing interval, where the background conditions are closer to Run-3 and every event that passes the L1 trigger selection is saved. In particular, this sample has been used to study the rate reduction effects of the proposed trigger.

In order to estimate the acceptance of the BIS78 chambers, the ROIs are matched to a muon when it has a $p_T > 20$ GeV and a ΔR(ROI,reconstructed muon)< 0.1 (where $\Delta R = \sqrt{\Delta\eta^2 + \Delta\phi^2}$). The RPC hits are emulated using particular MDT track segments, which are required to point to the interaction point, to lie within a certain $\Delta\eta = \eta_{segment} - \eta_{ROI}$ from the ROI, and to be in a sector which is compatible with the ϕ coordinate of the ROI.

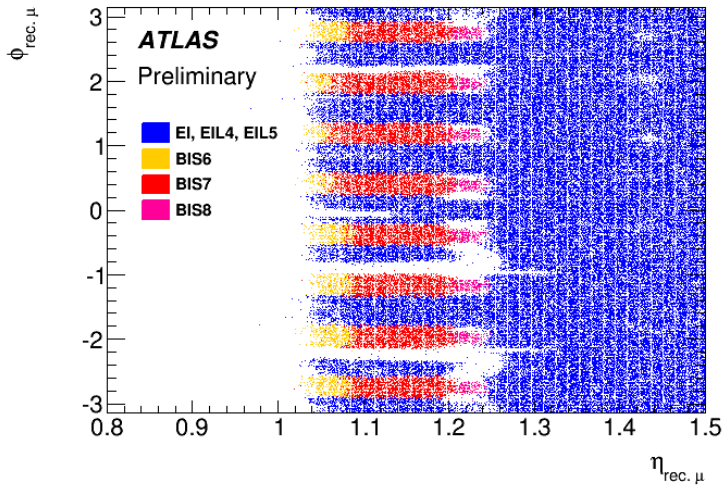

Figure 5.26: $\eta - \phi$ distribution of reconstructed muons ($p_T > 20$ GeV and associated to an End Cap trigger) associated to segments in the inner End Cap Chambers (EI) (in blue) and in the BIS chambers (all other colors) [111].

The $\eta - \phi$ distribution of the reconstructed muons associated with segments in EI and BIS chambers in the range $1 < \eta < 1.3$ is shown in Figure 5.26. This distribution gives a good estimation of the geometrical coverage of the proposed trigger. The rails and the cryo-lines of ATLAS limit with some holes the coverage of the TGCs in large sectors, while the BIS chambers (and in particular the BIS7 chambers) occupy a large part of the transition region, bringing the total coverage of the designed trigger to about 83.5% of the $1 < \eta < 1.3$ region.

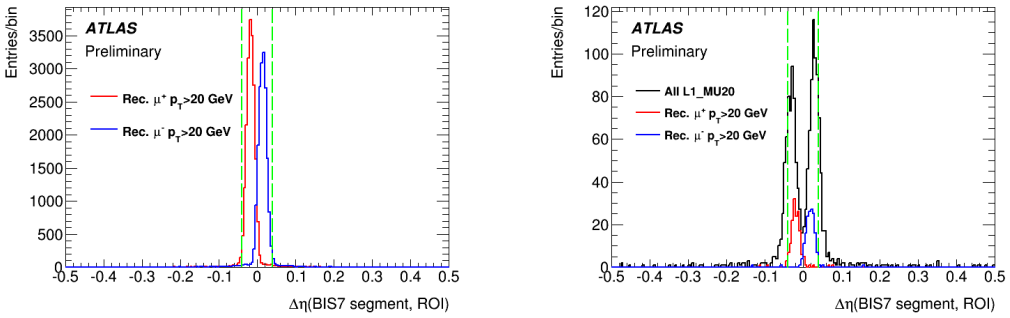

Figure 5.27: The distribution of $\Delta\eta$ between the track segments inside the BIS7 chamber and the ROIs of Level-1 single muon trigger ($p_T > 20$ GeV) associated to the reconstructed muons [111]. On the left the distribution is obtained with runs at 50 ns; on the right the distribution is obtained with runs at 25 ns. On the right the distribution obtained using all the ROIs is also drawn (in black).

The effects of a $\Delta\eta$ cut

The distribution of $\Delta\eta$ in the BIS chambers has been studied, as it is shown in figure 5.27. The picture on the left shows the $\Delta\eta$ distribution the ROIs associated to the reconstructed muons which has been obtained using standard runs at 50 ns. The picture on the right shows the same distribution obtained with special runs at 25 ns, superimposed to the distribution obtained using all the ROIs and so including the background. It can be seen quite clearly that the signal is concentrated in a region of $|\Delta\eta| < 0.04$, suggesting a $\Delta\eta$ criterium in the algorithm of the trigger in order to reject a higher background fraction.

Indeed, figure 5.28 shows that a $\Delta\eta$ cut of 0.04 leads to a further rejection of almost $\sim$30% of the events with a reconstructed muon associated with an MDT track segment, all concentrated in the low p_T spectrum, which correspond to background.

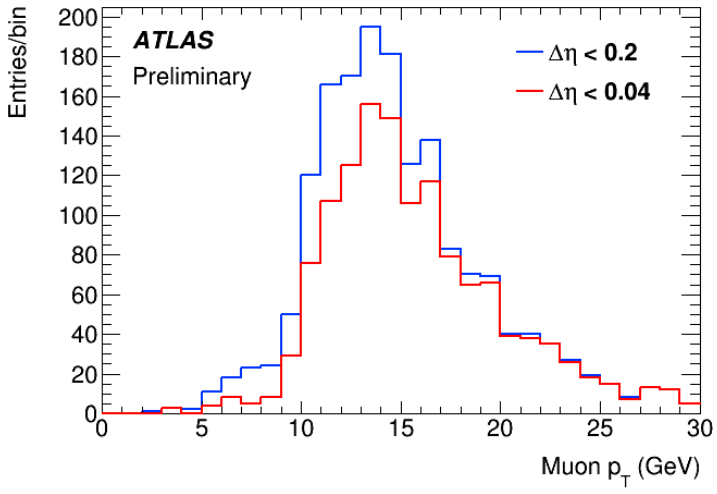

Figure 5.28: Distribution of the transverse momentum of the reconstructed muons obtained with different cuts in the difference $\Delta\eta$ between the segments in the inner plane and the Level-1 single muon ROIs ($p_T > 20$ GeV) [111]. The distribution obtained with $\Delta\eta < 0.2$ is drawn in blue, while the one obtained with $\Delta\eta < 0.04$ is drawn in red.

Results

In figure 5.29 it can be seen the η distribution of ROIs obtained with the "enhanced bias" sample at 25 ns with every event that passes the L1 trigger. This distribution is drastically reduced in transition region by the request of segments in the BIS and EI chambers.

The performance of the new trigger has been evaluated studying the following variables. The *efficiency* is the ratio between the reconstructed muons triggered by End Cap associated with segments in the BIS or EI chambers and all the reconstructed muons triggered by End Cap:

$$\text{Efficiency} = \frac{N_{\text{MuReco}}(\text{EndCap\&(BIS||EI)})}{N_{\text{MuReco}}(\text{EndCap})}$$

The *rate fraction* is the fraction of the End Cap trigger rate remaining after the requirement of a coincidence with the inner plane:

$$\text{Rate Fraction} = \frac{N_{\text{ROI}}(\text{EndCap\&(BIS||EI)})}{N_{\text{ROI}}(\text{EndCap})}$$

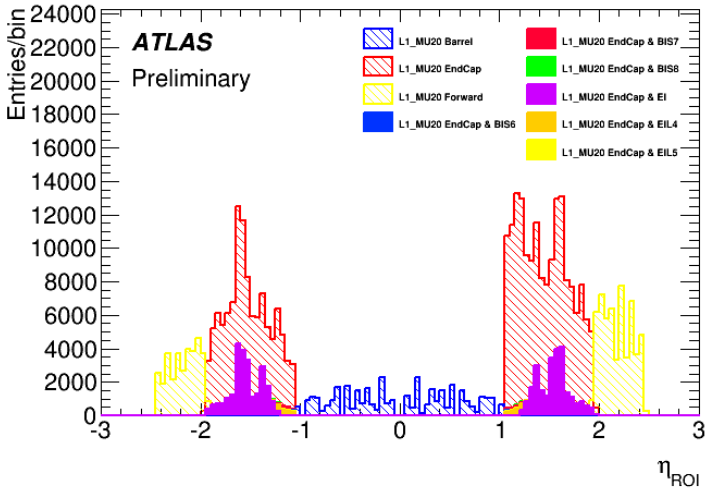

Figure 5.29: The η distribution of the ROIs ($p_T > 20$ GeV) in runs with 25 ns of bunch crossing interval [111]. The hatched blue distribution is obtained with the current Barrel trigger, the hatched red and yellow distristributions are obtained with the current End Cap trigger (divided in End Cap and Forward), while the fully colored distributions are obtained requiring the passage through the EI or the BIS chambers.

The *background fraction* is the fraction of the End Cap trigger background remaining after the requirement of a coincidence with the inner plane:

$$\text{Background Fraction} = \frac{N_{\text{ROI}}(\text{EndCap\&(BIS||EI)\&!MuReco})}{N_{\text{ROI}}(\text{EndCap})}$$

In a realistic trigger scheme the request of a coincidence on the inner plane should be applied only for the ROIs that are within the acceptance of the BIS and EIL chambers of the inner plane. Otherwise it will result in an efficiency loss. For this reason a map of the inner plane acceptance for each Endcap trigger roi was done as shown in Figure 5.30.

The criterion to decide whether a ROI is within the inner plane acceptance is that $\geq$ 95% of the reconstructed muon associated to the ROI have a coincidence in the inner plane.

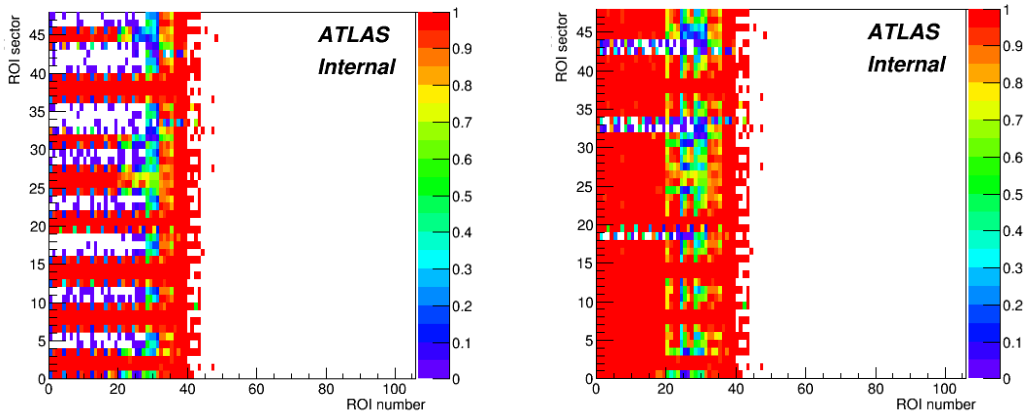

Figure 5.30: The map of the ROIs associated with segments in the EI chambers (on the left) or in BIS+EI chambers (on the right). The colour represents the percentage of cases in which there is a segment on the inner plane associated with the ROI.

Table 5.30 shows the results of the performance evaluation in the region $1 < |\eta| < 1.3$, obtained studing three different possibilities:

- requiring the inner plane coincidence for all the ROIs (BIS+EI everywhere);
- requiring a coincidence only with EI chambers for ROIs within EI acceptance (EI in EI acceptance),
- requiring a coincidence with the inner plane for all the ROIs within EI+BIS acceptance (BIS+EI in BIS+EI acceptance).

The first case shows that the rate can be significantly reduced asking a coincidence with the BIS+EI chambers, at the price of a great loss of efficiency due to the holes of this inner plane. The latter cases show that it is possible to obtain an important reduction of the rate and background fraction with only a small decrease of the efficiency.

	BIS+EI everywhere	**EI in EI acceptance**	**BIS+EI in BIS+EI acceptance**
Efficiency	80.1%	99.8%	98.9%
Rate Fraction	6.8%	54.5%	35.2%
Background Fraction	5.5%	53.5%	34.1%

Table 5.30: Efficiency, rate fraction and background fraction calculated in the transition region for three different cases. In the first column the segments inside BIS and EI are requested in association to all ROIs of the transition region; in the second (third) column the EI (BIS+EI) segments are requested only in association to ROIs in the EI (BIS+EI) acceptance, and no requiremenrs are made on other ROIs.

Mechanical layout

The limited available space in the detector for the new trigger has made the design of its mechanical layout really challenging. The BIS7 and BIS8 MDT chambers will be replaced with integrated chambers holding a new type of small MDT [112] (with diameter of 15 mm instead of 30 mm of standard MDTs) and new RPC [113] in the same envelope of the old MDT chambers, as shown in figure 5.31. The new RPC is a three-layer detector operating with a 2/3 majority configuration, and the chamber thickness will be of about 48 mm.

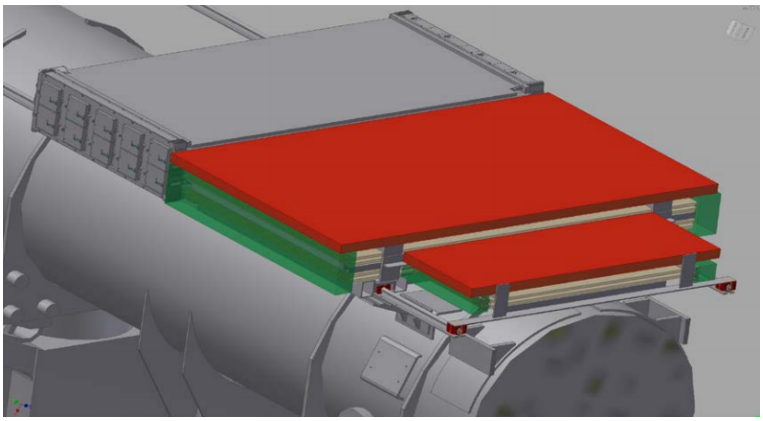

Figure 5.31: The proposed layout of an integrated chamber holding the small MDT (green and gray) and RPC (in red) in the same envelope of the old MDT chambers. The small MDT chamber is made of a single piece covering the area of BIS7 an BIS8, the RPC is instead split in two.

Conclusions

An upgrade of the ATLAS muon trigger in the Barrel - End Cap transition region with RPCs has been proposed in order to reduce the fake trigger rate. To better integrate the new trigger chambers in the limited amount of available space in an already existing system, a new integrated chamber has been developed, with new small MDTs for precise tracking and a triplet of new smaller RPCs with a new front end amplifier, leading to a better rate capability.

I personally realized performance studies made with 2012 data, which show that this upgrade will reduce significantly the rate, keeping almost all the signal, leading to a full coverage of the transition region with a selective trigger. The results of these studies were used in the review that led to the approval of the upgrade project in 2015 by the ATLAS Collaboration.

Bibliography

[1] F. Abe et al. (CDF Collaboration), Physical Review letters 74:2626-2631 (1995)
S. Abachi et al. (D0 Collaboration), Physical Review letters 74:2422-2426 (1995)

[2] ATLAS, CDF, CMS, D0 Collaborations, arXiv:1403.4427

[3] C. Quigg, *"Gauge Theories of the Strong, Weak, and Electromagnetic Interactions"*, Addison-Wesley (1983).
M. Gell-Mann, Phys. Lett. **8** 214 (1964)
G. Zweig, *"CERN Report"*, 8182/Th.401 (1964)

[4] J. Beringer et al. (Particle Data Group), Phys. Rev. D86, 010001 (2012)

[5] S. L. Glashow, Nucl. Phys. 22, 579 (1961)
A. Salam and J. C. Ward, Phys. Lett. 13, 168 (1964)
S. Weinberg, Phys. Rev. Lett. 19, 1264 (1967)

[6] P. W. Higgs, Phys. Lett. 12, 132 (1964)
Phys. Rev. Lett. 13, 508 (1964)
Phys. Rev.145, 1156 (1966)

[7] ATLAS Collaboration, Phys. Lett. B 716, 1, 1-29 (2012)

[8] CMS Collaboration, Phys. Lett. B 716, 1, 30-61 (2012)

[9] N. Cabibbo, Phys. Rev. Lett. 10, 531 (1963)

[10] S.L. Glashow, J. Iliopoulos, L. Maiani, Physical Review D 2 (7) 1285 (1970)

[11] J.H.Christenson et al., Phys. Rev. Lett. 13, 138 (1964)

[12] M. Kobayashi and T. Maskawa, Prog. Theor. Phys. 49, 652 (1973)

[13] J. Davis, Raymond, D. S. Harmer, and K. C. Hoffman, Phys. Rev. Lett. 20, 1205 (1968)
B. T. Cleveland et al., Astrophys. J. 496, 505 (1998)
Super-Kamiokande, Y. Fukuda et al., arXiv:hepex/9807003 (1998)
SNO, Q. R. Ahmad et al., arXiv:nucl-ex/0106015 (2001)
Super-Kamiokande, S. Fukuda et al., arXiv:hepex/0205075 (2002)
K2K, M. H. Ahn et al., arXiv:hep-ex/0212007 (2003)
Particle Data Group, W. M. Yao et al., J. Phys. G33, 1 (2006)

[14] B. Pontecorvo, Sov. Phys. JETP 26, 984 (1968)
Z. Maki, M. Nakagawa, and S. Sakata, Prog. Theor. Phys. 28, 870 (1962)

[15] A.Quadt, Eur. Phys. J. C 48, 835-1000 (2006)

[16] http://lepewwg.web.cern.ch/LEPEWWG/plots/winter2012/

[17] J. C. Collins, D. E. Soper and G. Sterman, Nucl. Phys. B 263, 37 (1986)

[18] V.M. Abazov et al. (D0 Collaboration), Phys. Rev. Lett. 103, 092001 (2009)
T.Aaltonen et al. (CDF Collaboration), Phys. Rev. Lett. 103, 092002 (2009)

[19] ATLAS Collaboration, ATLAS-CONF-2011-027 (2011).
ATLAS Collaboration, ATLAS-CONF-2011-088 (2011).
ATLAS Collaboration, Physics Letters B 717, 330-350 (2012)
ATLAS Collaboration, ATL-PHYS-PUB-2009-001 (2009).
ATLAS Collaboration, ATLAS-CONF-2011-104 (2011)
ATLAS Collaboration, ATLAS-CONF-2011-118 (2011).

[20] CMS Collaboration, Phys.Rev.Lett.107:091802 (2011)
CMS Collaboration, CMS-PAS-TOP-11-021 (2012).
CMS Collaboration, CMS-NOTE-2006/084 (2006).
CMS Collaboration, CMS-PAS-TOP-11-022 (2011).

[21] Nikolaos Kidonakis, Phys.Part.Nucl.45:714 (2014)

[22] ATLAS Collaboration, Eur.Phys.J.C39S2:63-90 (2005)

[23] H. M. Georgi et al., Ann. Phys. 114, 273, (1978)
L. M. Jones and H. W. Wyld, Phys. Rev. D17, 1782, (1978)
M. Gluck, J. F. Owens and E. Reya, Phys. Rev. D17, 2324, (1978)
J. Babcock, D. Sivers and S. Wolfram, Phys. Rev. D18, 162, (1978)
K. Hagiwara and T. Yoshino, Phys. Lett. B80, 282, (1979)
B. L. Combridge, Nucl. Phys. B151, 429, (1979)
W. Beenakker et al., Nucl. Phys. B411, 343, (1994)

[24] P. Nason, S. Dawson and R. Ellis, Nucl. Phys. B303, 607 (1988)
W. Beenakkeret al., Phys. Rev. D40, 54 (1989)

[25] W. Bernreuther et al., Phys. Rev. Lett. 87, 242002 (2001)

[26] M. Czakon and A. Mitov, Nucl.Phys.B824:111-135(2010)

[27] M. Cacciari et al., JHEP 09, 127 (2008)
S. Moch and P. Uwer, Phys. Rev. D78, 034003 (2008)
N. Kidonakis and R. Vogt, Phys. Rev. D78, 074005 (2008)

[28] Michal Czakon, Alexander Mitov, Computer Physics Communications 185 2930 (2014)

[29] U. Langenfeld, S. Moch, and P. Uwer, arXiv:0907.2527 [hep-ph](2009)

[30] M. Barisonzi, AIP Conf.Proc.794:85-88 (2005)

[31] ATLAS Collaboration, CERN/LHCC 99-15 (1999)

[32] R. M. Harris, C. T. Hill, and S. J. Parke, arXiv:9911288 [hep-ph] (1999)

[33] Valentin Ahrens, Andrea Ferroglia, Matthias Neubert, Ben D. Pecjak, and Li-Lin Yang, 10.1007/JHEP09 070 (2011)

[34] John M. Campbell and R.K. Ellis, Nucl.Phys.Proc.Suppl.205-206:10-15 (2010)

[35] T. A.older et al. (CDF Collab.), Phys. Rev. Lett. 102,222003 (2009).

[36] D0 Collab., D0-CONF-6379 (2013).

[37] ATLAS Collab., ATLAS-CONF-2013-099 (2013).

[38] S. Chatrchyan et al. (CMS Collab.), Eur. Phys. J. C73,2339 (2013).

[39] CMS Collab., CMS-PAS-TOP-12-027 (2013)
CMS Collab., CMS-PAS-TOP-12-028 (2013).

[40] CMS Collab., CMS-PAS-TOP-12-042 (2013).

[41] ATLAS Collaboration, arXiv:1510.03818

[42] ATLAS Collaboration, JINST 3 S08003 (2008)

[43] ATLAS Collaboration, ATLAS TDR 4, CERN/LHCC 97-16 (1997)

[44] ATLAS Collaboration, ATLAS TDR 7, CERN/LHCC 97-19 (1997)

[45] ATLAS Collaboration, ATLAS TDR 8, CERN/LHCC 97-20 (1997)

[46] ATLAS Collaboration, ATLAS TDR 9, CERN/LHCC 97-21 (1997)

[47] ATLAS Collaboration, ATLAS TDR 11, CERN/LHCC 98-13 (1998)

[48] J. N. Jackson, Nucl. Instrum. Meth. A541 89-95 (2005)

[49] ATLAS Collaboration, ATL-COM-PHYS-2012-1541

[50] ATLAS Collaboration, ATLAS TDR 2, CERN/LHCC 96-41 (1996)

[51] ATLAS Collaboration, Eur. Phys. J. C 74:3071 (2014)

[52] ATLAS Collaboration, ATLAS TDR 3, CERN/LHCC 96-42 (1996)

[53] Ana Maria Henriques Correia, ATL-TILECAL-SLIDE-2015-195 (2015)

[54] ATLAS Hadronic End-Cap Calorimeter Group, JINST 2 P05005 (2007)

[55] J.P. Archambault et al., JINST 8 P05006 (2013)

[56] ATLAS Collaboration, ATLAS TDR 10, CERN/LHCC 97-22 (1997)

[57] ATLAS Collaboration, Eur. Phys. J. C 73 2518 (2013)

[58] ATLAS Collaboration, CERN/LHCC 98-15 (1998)

[59] ATLAS Collaboration, Eur. Phys. J. C 73 2518 (2013)

[60] ATLAS Collaboration, Eur.Phys.J.C70:823-874 (2010)

[61] M.Dobbs, J.B. Hansen, Comput. Phys. Commun. 134 41-46 (2001)

[62] Michael H. Seymour and Marilyn Marx, arXiv:1304.6677 (2013)

[63] G. Ballocchi et al, Nucl.Phys. B345 (1990)

[64] B. Andersson, JHEP 05 026 (2006)

[65] T.Sjostrand, S. Mrenna and P.Skands, JHEP 05 026 (2006)

[66] B. R. Webber, Nucl. Phys. B238 492 (1984)

[67] G. Corcella et al., JHEP 01 010 (2001)

[68] T. Sjöstrand and M. van Zijl, Phys. Rev. D 36, 2019 (1987)

[69] J. B. J. R. Forshaw and M. Seymour, Z.780 Physics C72 (1996)

[70] S.Frixione, P.Nason and B.R. Webber, JHEP 08 007 (2003)

[71] S.Frixione, P,Nason and C.Oleari, JHEP 11 300-304 (2007)

[72] M.L. Mangano et al., JHEP 07 001 (2003)

[73] B. P. Kersevan and E. Richter-Was, Comput.Phys.Commun. 149, 142 (2003)

[74] T. Gleisberg et al., JHEP 02 056 (2004)

[75] S. Catani, F. Krauss, R. Kuhn, B.R. Webber, JHEP 0111:063 (2001)

[76] S. Agostinelli et al., Nuclear Instruments and Methods A 506 250-303 (2003)

[77] H. Lai, Physical Review D 82 (2010)

[78] J. Pumplin, D.R. Stump, J. Huston, H.L. Lai, P. Nadolsky, W.K. Tung, JHEP 0207:012 (2002)

[79] ATLAS Collaboration, CERN-OPEN-2008-020 (2008)

[80] M.Cacciari and G.Salam, Phys.Lett.B641:57-61 (2006)

[81] Matteo Cacciari, Gavin P. Salam, Gregory Soyez, JHEP 0804:063 (2008)

[82] ATLAS Collaboration, ATLAS-CONF-2015-017

[83] D W Miller, A Schwartzman, and D Su, ATL-COM-PHYS-2009-180 (2009)

[84] D. Krohn, J. Thaler and L.-T. Wang, Jet Trimming, JHEP 02 084 (2010)

[85] ATLAS Collaboration, ATLAS-CONF-2011-102 (2011)

[86] ATLAS Collaboration, ATLAS-CONF-2014-004 (2014)

[87] ATLAS Collaboration, ATLASCONF-2010-005 (2010)

[88] ATLAS Collaboraion, ATLAS-CONF-2014-032

[89] K. Rehermann and B. Tweedie, JHEP 03 059 (2011)

[90] T. Lagouri et al., IEEE Trans. Nucl. Sci. 51, 3030-3033 (2004)

[91] S. Hassani, L. Chevalier, E. Lancon, J. F. Laporte, R. Nicolaidou and A. Ouraou, Nucl.Instrum. Meth. A572, 77 (2007)

[92] ATLAS Collaboraion, Eur.Phys.J. C74 3130 (2014)

[93] ATLAS Collaboration, ATLAS-CONF-2013-082

[94] V. Abazov et al., Phys.Rev. D76, 092007 (2007)

[95] ATLAS Collaboration, Eur. Phys. J. C73 2261 (2013)

[96] V. Bobel, arXiv:hep-ex/0208022v1 (2002)

[97] A. Hocker and V. Kartvelishvili, Nucl.Instrum.Meth.A372:469-481 (1996)

[98] G.H. Golub et al., SIAM Journal on Matrix Analysis and Applications archive Vol.21 N.1, (doi: 10.1137/S0895479897326432) (1999)

[99] ATLAS Collaboration, Eur. Phys. J. C 73 2518 (2013)

[100] https://twiki.cern.ch/twiki/bin/viewauth/AtlasProtected/UJUncertaintyProvider

[101] ATLAS Collaboration, Eur. Phys. J. C 73 2304 (2013)
ATLAS Collaboration, Eur. Phys. J. C 75 17 (2015)
ATLAS Collaboration, Eur. Phys. J. C 73 2305 (2013)

[102] ATLAS Collaboration, JHEP 05 128 (2012)
ATLAS Collaboration, Eur. Phys. J. C73 2306 (2013)

[103] ATLAS Collaboration, Eur. Phys. J. C 73 2306 (2013)

[104] ATLAS Collaboration, ATLAS-CONF-2014-004 (2014).
ATLAS Collaboration, ATLAS-CONF-2012-043 (2012)
ATLAS Collaboration, ATLAS-CONF-2012-040 (2012)

[105] A. Buckley at al., arXiv:1003.0694v8 [hep-ph] (2013)

[106] M. Cacciari, G.P. Salam and G. Soyez, Eur.Phys.J. C72 1896 (2012)

[107] ATLAS Collaboration, ATLAS TDR 17, CERN/LHCC 2005-022 (2005)

[108] ATLAS Collaboration, ATLAS TDR 023, CERN/LHCC-2013-018 (2013)

[109] ATLAS Muon Collaboration, https://twiki.cern.ch/twiki/bin/view/AtlasPublic/MuonTriggerPublicResults

[110] ATLAS Collaboration, ATLAS TDR 020, CERN/LHCC 2013-006 (2013)

[111] ATLAS Muon Collaboration, ATL-COM-MUON-2014-008 (2014)

[112] B. Bittner et al., Nucl. Instr. and Meth. A 628 154 (2011)

[113] R. Santonico, Technology and Instrumentation in Particle Physics, http://indico.cern.ch/event/102998/session/16/contribution/427 (2011)

[114] R. Cardarelli et al., JINST 8 P01003 (2013)